Silesian University of Technology
The Automatics, Robotics and Informatics
Department of Data Science and Engineering

Doctoral Dissertation

Computer-Assisted Detection and Quantification of Low-Attenuation Lung Patterns in CT Studies of COPD Patients

Author: Marek Socha
Supervisor: Professor Joanna Polańska, PhD, DSc

Gliwice, May 2025

I sincerely thank Professor Joanna Polańska
for supervising my research, providing invaluable guidance,
and offering constant support.

I am also grateful to my colleagues
from the Department of Data Science and Engineering
for their help and encouragement during difficult times.

I want to express my gratitude towards Anna Kurianowicz
for her assistance and unwavering support throughout my journey.

And I want to thank my family
for creating an opportunity for me to pursue a scientific career.

Thank you all for your support!

Abstract

Artificial intelligence (AI) is transforming many fields, including entertainment, daily life, and industry. It is also becoming an important tool in medicine. Modern healthcare faces challenges such as high workloads and staff shortages, leading to long waiting times for test results. AI can help by pre-analyzing medical data, making diagnostics more efficient. It can guide doctors in their analysis and highlight important medical information, improving patient care.

Computed Tomography (CT) is an advanced imaging technique that creates detailed three-dimensional images of tissues. It has greatly improved diagnostics in various medical fields. In pulmonology, CT is especially valuable, as it allows the detection of lung lesions in areas that cannot be directly examined by doctors.

Chronic obstructive pulmonary disease (COPD) is a growing health concern linked to rising air pollution and tobacco smoking. It is characterized by emphysema, a condition in which parts of the lung tissue are permanently damaged and destroyed, reducing lung function.

The dissertation examined the potential of artificial intelligence (AI) for detecting and quantifying emphysema. The study used CT images from the COPDGene database and the MOLTEST bis project. It provided a detailed analysis of the biological background of emphysema and the methods used for its segmentation. Based on it, a processing pipeline was developed, including lung segmentation, airway segmentation, lesion segmentation, and their quantification and differential analysis. A novel airway segmentation method was introduced, using iterative propagation from landmarks based on two dominant features. To ensure explainability and alignment with medical practices, an automatic thresholding method based on Gaussian mixtures was proposed for emphysema segmentation. For qualitative and quantitative assessment of emphysema, a set of features has been calculated which can be compared with other similar cases based on the created two-dimensional embedding.

The analysis demonstrates the potential of the proposed methods for practical use. However, further validation and expansion of the database with additional data are needed before application in an industrial setting.

Streszczenie

Sztuczna inteligencja (AI) wywiera istotny wpływ na liczne obszary, w tym rozrywkę, życie codzienne oraz przemysł. Coraz częściej znajduje również zastosowanie w medycynie, stając się kluczowym narzędziem wspierającym procesy diagnostyczne i terapeutyczne. Współczesna opieka zdrowotna mierzy się z wieloma wyzwaniami, takimi jak nadmierne obciążenie pracą personelu medycznego oraz jego niedobory, co skutkuje wydłużonym czasem oczekiwania na wyniki badań. Zastosowanie sztucznej inteligencji umożliwia wstępną analizę danych medycznych, przyczyniając się do zwiększenia efektywności diagnostyki. Ponadto AI wspomaga lekarzy w interpretacji wyników badań, identyfikując kluczowe informacje medyczne, co w konsekwencji prowadzi do poprawy jakości opieki nad pacjentem.

Tomografia komputerowa (TK) stanowi zaawansowaną metodę obrazowania medycznego, umożliwiającą uzyskanie szczegółowych trójwymiarowych rekonstrukcji struktur tkankowych. Technika ta znacząco przyczyniła się do postępu w diagnostyce wielu dziedzin medycyny. W pulmonologii tomografia komputerowa odgrywa szczególnie istotną rolę, gdyż pozwala na wykrywanie zmian patologicznych w obrębie płuc.

Przewlekła obturacyjna choroba płuc (POChP) stanowi narastający problem zdrowotny, którego rozwój jest ściśle związany z rosnącym zanieczyszczeniem powietrza oraz paleniem tytoniu. Schorzenie to charakteryzuje się występowaniem rozedmy płuc, czyli stanu patologicznego prowadzącego do trwałego uszkodzenia oraz destrukcji tkanki płucnej, co skutkuje stopniowym obniżeniem ich funkcji.

Rozprawa doktorska bada potencjał sztucznej inteligencji (AI) w wykrywaniu i ilościowym określaniu rozedmy płuc, wykorzystując obrazy tomografii komputerowej (TK) z baz danych COPDGene i MOLTEST bis. Przedstawiono analizę biologicznych podstaw rozedmy oraz metod segmentacji, opracowując potok przetwarzania obejmujący segmentację płuc, dróg oddechowych i zmian chorobowych, ich kwantyfikację i analizę różnicową. Wprowadzono nową metodę segmentacji dróg oddechowych opartą na iteracyjnej propagacji z punktami orientacyjnymi. Zastosowano automatyczne progowanie segmentacji rozedmy oparte na mieszaninach Gaussa, a także obliczono cechy umożliwiające porównanie przypadków za pomocą dwuwymiarowego osadzenia.

Przeprowadzona analiza wskazuje na potencjalną użyteczność proponowanych metod w praktycznych zastosowaniach. Niemniej jednak, przed ich wdrożeniem w warunkach przemysłowych konieczna jest dalsza walidacja oraz rozszerzenie bazy danych o dodatkowe dane TK.

Contents

1 Introduction **1**
- 1.1 Motivation . . . 1
- 1.2 Scope of the dissertation . . . 2
- 1.3 Aim of the work and thesis . . . 2
- 1.4 Structure . . . 4

2 Technical background **5**
- 2.1 Computed Tomography . . . 5
- 2.2 Hounsfield units . . . 6
- 2.3 Storage standard . . . 6
- 2.4 Patient, study and series . . . 6
- 2.5 Slice thickness . . . 7
- 2.6 Scanner parameters . . . 7
- 2.7 Scanner model . . . 8
- 2.8 Convolution Kernel . . . 8
- 2.9 High and Low dose CT . . . 9
- 2.10 Anatomical factors influencing results . . . 10

3 Biological background **11**
- 3.1 About human lungs . . . 11
- 3.2 Lung Parenchyma and Intersitium . . . 12
- 3.3 Airways . . . 12
- 3.4 Pulmonary arteries and veins . . . 14
- 3.5 Blood-Gas barrier exchange . . . 14
- 3.6 Abnormal patterns in lungs . . . 14
  - 3.6.1 Emphysema . . . 15
  - 3.6.2 Air trapping . . . 17
- 3.7 Chronic Obstructive Pulmonary Disease . . . 18
- 3.8 Quantification of emphysema and COPD . . . 19
  - 3.8.1 Spirometry . . . 19
  - 3.8.2 Symptomatic and quality of life check . . . 20
  - 3.8.3 Macroscopy and microscopy . . . 20
  - 3.8.4 Image analysis . . . 21

4 Materials **25**
4.1 COPDGene . . . 25
4.2 MOLTEST-BIS subset . . . 27

5 Lungs and Lobes segmentation **28**
5.1 Motivation . . . 28
5.2 State of the art . . . 29
5.3 Results . . . 32
5.4 Discussion . . . 35

6 Airways **37**
6.1 Motivation . . . 37
6.2 State of the art . . . 40
6.3 Methods . . . 42
6.3.1 Mediastinum segmentation . . . 42
6.3.2 Trachea segmentation . . . 43
6.3.3 Rough High and Low attenuation elements segmentation . . . 43
6.3.4 Speed map creation . . . 44
6.3.5 Seed points generation . . . 46
6.3.6 Fast Marching segmentation . . . 47
6.3.7 Airways wall guided segmentation . . . 47
6.3.8 Over and Under segmentation detection . . . 47
6.4 Results . . . 49
6.5 Disscussion . . . 53

7 Low attenuation patterns **55**
7.1 Motivation . . . 55
7.2 State of the art . . . 56
7.3 Methods . . . 58
7.3.1 Preprocessing . . . 59
7.3.2 GMM decomposition . . . 59
7.3.3 Grouping . . . 61
7.3.4 Membership function creation . . . 62
7.3.5 Slice thresholds . . . 62
7.3.6 Final Thresholds . . . 62
7.3.7 Comparative analysis of methods . . . 64
7.4 Results . . . 65
7.5 Discussion . . . 70

8 Quantification and mapping **72**
8.1 Motivation . . . 72
8.2 State of the art . . . 73
8.3 Methods . . . 76
8.3.1 Splitting emphysema mask to ROIs . . . 77

8.3.2 Features Extraction 77
8.3.3 Preprocessing 78
8.3.4 Embedding 79
8.3.5 Features significance 82
8.4 Results 83
8.5 Discussion 88
8.5.1 UMAP 1 88
8.5.2 UMAP 2 91
8.5.3 UMAP features significance conclusion 95

9 Summary **96**

Bibliography **99**

List of Figures

2.1 Example Computed Tomography scanner and ideogram showing core working principles a) Siemens SOMATOM Force CT scanner [11], b) X-ray generator rotates over the patient's body emitting X-ray beams which are scattered and absorbed by patient's tissues reaching the detector on the opposite side [12]. 5

3.1 Airways of the Human lung with the airways division ideogram according to the Weible [37]. 13
3.2 Emphysema sub-types ideograms a) centrilobular emphysema; b) panlobular emphysema; c) paraseptal emphysema [49]. 16
3.3 Side by side comparison between a) subpleural bullae emphysema [52], and b) air trapping [53], on the Computed Tomography images. 17

4.1 COPDGene used dataset CT series count divided based on the respiratory phase and convolution kernel. 26
4.2 COPDGene used dataset CT series count divided based on the GOLD standard classification. 27

5.1 U-Net architecture overview [115]. 31
5.2 Example slices from patients with mild and severe abnormal parenchymal changes with overlayed results of the lung segmentation using the Otsu thresholding method. 33
5.3 Example slices from patients with mild and severe abnormal parenchymal changes with overlayed results of the lung segmentation using the region growing method. 34
5.4 Example slices from patients with mild and severe abnormal parenchymal changes with overlayed results of the lung segmentation using the Fast Marching algorithm. 35
5.5 Example slices from patients with mild and severe abnormal parenchymal changes with overlayed results of the lung segmentation using U-Net 2D. 36

6.1 a) Healthy small airways; b) Airways blocked by connective tissue and restricting its lumen, resulting from inflammation [137]. 38

6.2 a) Photograph of a mid-sagittal slice of a lung removed from a patient who received a lung transplant for COPD from the work of Hogg et. al [137]. CLE-related changes resulting in highly inflamed upper lungs; b) Similar specimen from a patient who received a lung transplant also from the work of Hogg et. al [137]. Less severe PLE but the lower lungs are highly involved. 39
6.3 Trachea mask resulting from described methodology. 43
6.4 Final speed map image resulting from the multiplication of speed components. 46
6.5 First subplot, airways mask after the Fast Marching segmentation, second subplot, final airways mask after wall-guided segmentation. 48
6.6 Example airways segmentations from each mark, 1-4 under-segmentation, 5 proper segmentation and 6-9 over-segmentation. 49
6.7 Distribution of airway segmentations' marks, the majority of segmentations are of good quality (5) or sufficient quality (4, 6). 50
6.8 Barplot showing correlation coefficients of the features tested against the grade of the airways segmentation. 51
6.9 Boxplot, where the whiskers were calculated using Hubert et al. [183], and used for filtration of the faulty (outlying) airways segmentations. . 52

7.1 Approximate Threshold Estimation (ATE) pipeline. 58
7.2 Exact Threshold Estimation (ETE) pipeline. 59
7.3 Three-dimensional space of normal distribution parameters (mean, std and alpha) showing final clusters coloured by threshold resulting from the ATE method. 63
7.4 Final clusters and threshold resulting from the ETE method. 64
7.5 Example results of ATE segmentation method shown on CT patient images with each GOLD standard classification a) GOLD 0, b) GOLD 1, c) GOLD 2, d) GOLD 3, e) GOLD 4. 66
7.6 Distibutions of HU values in the segmentations done by ATE and ETE methods in patients with and without emphysema. 67
7.7 The qqplot of the differences between $ATE - ETE$ methods shows that it is not normally distributed data. 68
7.8 Boxplots showing the difference in the thresholds between the ATE and ETE method per-GOLD standard group. 69
7.9 Segmented masks' volumes using ATE and ETE methods. 70
7.10 Example CT images' axial slices of patients from the GOLD 3 group with emphysematous changes whose thresholds were above -900 HU values. . 71

8.1 Density plots of resulting UMAP embedding shown on different subplots. For each GOLD group, areas of the largest densities have been found and named following the convention C(GOLD)(cluster number left-right). 83
8.2 UMAP embedding density plot for GOLD 0 group with example images taken from the centre of each cluster. 84

8.3 UMAP embedding density plot for GOLD 1 group with example images taken from the centre of each cluster. 85
8.4 UMAP embedding density plot for GOLD 2 group with example images taken from the centre of each cluster. 86
8.5 UMAP embedding density plot for GOLD 3 group with example image taken from the centre of the cluster. 86
8.6 UMAP embedding density plot for GOLD 4 group with example image taken from the centre of the cluster. 87
8.7 SHAP median values of features across samples showing features' impact on the UMAP 1 (U1) and UMAP 2 (U2) axis. 87
8.8 Minimum of Run Entropy distribution across the UMAP embedding (reference GOLD distribution in bottom-left corner). Example images with low and high feature values with their voxel-based feature heatmaps. 89
8.9 Standard deviation of Run Entropy distribution across the UMAP embedding (reference GOLD distribution in bottom-left corner). Example images with low and high feature values with their voxel-based feature heatmaps. 89
8.10 Standard deviation of Contours' Small Area Emphasis distribution across the UMAP embedding (reference GOLD distribution in bottom-left corner). Example images with low and high feature values with their voxel-based feature heatmaps. 90
8.11 Mean of ROIs' Surface Area distribution across the UMAP embedding (reference GOLD distribution in bottom-left corner). Example images with low and high feature values, with and without overlaid segmentations' contours. 91
8.12 Standard deviation of Minor Axis Length distribution across the UMAP embedding (reference GOLD distribution in bottom-left corner). Example images with low and high feature values, with and without overlaid segmentations' contours. 92
8.13 Minimum of Run Percentage distribution across the UMAP embedding (reference GOLD distribution in bottom-left corner). Example images with low and high feature values with their voxel-based feature heatmaps. 92
8.14 Minimum of Run Length Non-Uniformity Normalised distribution across the UMAP embedding (reference GOLD distribution in bottom-left corner). Example images with low and high feature values with their voxel-based feature heatmaps. 93
8.15 Maximum of Long Run Emphasis (LRE) distribution across the UMAP embedding (reference GOLD distribution in bottom-left corner). Example images with low and high feature values with their voxel-based feature heatmaps. 94
8.16 Minimum of Short Run Emphasis (SRE) distribution across the UMAP embedding (reference GOLD distribution in bottom-left corner). Example images with low and high feature values with their voxel-based feature heatmaps. 94

List of Tables

3.1 Summarisation of the differences between macroscopy and microscopy quantification methods. 22

4.1 COPDGene summary of the computed tomography series used in the study. 26

6.1 Outlaying segmentations detection accuracy is shown per grade in the table. Grades 1-3 and 7-9 represent faulty and 4-6 proper segmentations. The system assigns 0 to faulty and 1 to proper segmentations. 52

7.1 Non-parametric Wilcoxon test results showing the strength of the thresholds difference in ATE and ETE methods. 69

Chapter 1

Introduction

1.1 Motivation

Chronic Obstructive Pulmonary Disease (COPD) is a progressive disorder obstructing airflow, causing severe shortness of breath, coughing, excessive mucus production, and may result in total respiratory failure. It causes permanent damage to the lung parenchyma called emphysema and inflammation in the airways. The disease is attributed mainly to cigarette smoking [1, 2] and poor air quality [3, 4]. Cigarettes contain nicotine, the addictive substance, which is a major reason why many people continue to smoke despite knowing the health risks, while according to recent studies, air pollution is increasing year by year [5]. As a result, COPD remains a widespread and serious health issue [1]. Early diagnosis and appropriate treatment are the keys to slowing or halting the progression of the disease, making artificial intelligence and machine learning a potential support for the treatment process.

Machine learning and artificial intelligence are currently developing rapidly, with various tools capable of generating detailed graphics from text [6], recommending music based on user preferences [7, 8], and engaging in conversations that closely resemble human interaction [9]. Most systems in the entertainment industry rely on deep learning due to the large availability of annotated data and the relatively stable nature of the tasks. However, in the medical field, the situation is different. Here, patient health is critical, and there is often a lack of labelled data, which calls for a different approach.

The emphysematous changes seen in COPD vary in location, shape, and severity. Although CT scans use a standardised scale of Hounsfield units, comparing scans from

different hospitals often reveals technical differences. Those differences result from the manufacturer of the scanner, scanner parameters, experience of radiologists and the applied scanning protocol. The effectiveness of a deep learning model is highly dependent on the quality of the training data it receives. Manually creating segmentations of 3D emphysematous changes is an extremely time-intensive task, which is infrequently undertaken. Moreover, such data is rarely shared publicly. This lack of available data undermines the reliability of deep learning solutions. This is a setting where the classical methods shine; with the knowledge gathered by the experts about the properties of certain lesions or abnormalities, large annotated dataset requirements can be bypassed. Also, with proper tuning and tests, a much more robust method can be created, or it is possible to define clear boundaries or requirements for the method to work.

1.2 Scope of the dissertation

The dissertation focuses on the analysis of emphysematous changes in chest CT scans of patients with Chronic Obstructive Pulmonary Disease (COPD). The primary aim is to design a method to locate and quantify the abnormal disease patterns despite the lack of hand-made annotations and inter-institutional variability in imaging protocols.

The low attenuation category was selected, with emphasis on COPD-related lesions, as a subject of this dissertation due to the availability of CT data accompanied by quantitative and qualitative assessments of disease progression. This information allowed for an evaluation of the segmentation quality produced by the proposed methodology. The segmentation and classification of high attenuation patterns also gained significant attention during the COVID-19 pandemic (2020–2023), leading to substantial research advancements in this area. In contrast, the segmentation and evaluation of low attenuation patterns have received less attention in recent scientific literature.

1.3 Aim of the work and thesis

This work proposes the establishment of an automated pipeline for the analysis of Computed Tomography images, with the objective of detecting and quantifying low attenuation lesions. The primary focus of this study is on images of patients diagnosed

with Chronic Obstructive Pulmonary Disease (COPD). The disease is characterised by emphysematous changes, i.e. permanent destruction of air bubbles, and small airway disease. The overarching objective of this study is to develop a system that can quantitatively analyse the nature of these changes.

This research concentrates on classical methods, which have shown better generalisation abilities than neural networks. The algorithms created are intended to be efficient but also explainable, and it is planned to implement and improve solutions familiar to radiologists that are used in medical practice. The pipeline comprises four distinct steps: lung segmentation, airway segmentation, emphysematous lesion segmentation and quantification with stratification. The lung segmentation problem has been extensively discussed in numerous publications; therefore, the objective is to evaluate the performance of existing solutions in relation to segmentations performed with classical methods. The goal of airway segmentation is to remove voxels that have similar Hounsfield Unit (HU) values to emphysematous lesions. A further aim of segmentation is to isolate bronchial walls for later automatic thickness analysis. The primary objective of emphysematous lesion segmentation is to identify the region affected by emphysema or other low-attenuation patterns. Quantification and stratification aim to describe the lesions numerically. Using created numerical descriptors, a 2D space will be created where patients are placed in the form of dots. This facilitates a comparative analysis of different cases, enabling the refinement of treatment strategies. The analyses conducted as part of the dissertation enabled the formulation of the following theses:

1. Unsupervised learning techniques demonstrate potential in the detection of low-attenuation lesions in computed tomography (CT) imaging, offering an effective alternative to supervised approaches by leveraging intrinsic data structures without the need for annotated training datasets.

2. The volume and spatial distribution of emphysematous regions identified through automated detection processes can serve as a preliminary estimate of COPD progression. These regions exhibit a quantitative and qualitative relationship with GOLD-defined spirometric measures.

3. To minimise false positives in the segmentation of low-attenuation and emphysematous lesions, it is crucial to construct a three-dimensional model of the airway structure.

1.4 Structure

Chapter two serves as an introduction to the technical foundation of this thesis. It addresses the subject of Computed Tomography imaging by describing the concepts of series and study, emphasising the critical parameters of CT images, and identifying factors that affect the quality of the scans.

Chapter three addresses the biological dimensions of the thesis. It provides an examination of the anatomical structure of the lungs and describes the respiratory process. Furthermore, it introduces the pulmonary abnormalities that constitute the focus of the study while evaluating current techniques for their quantification.

Chapter four describes the materials employed in this thesis. It outlines the datasets employed during the experimental processes, specifying the number of studies and series in the following datasets, along with the locations where the datasets were applied.

Chapter five addresses the segmentation process of the lungs and lobes, examining the availability of various methodologies and their efficacy in distinguishing lung parenchyma from other anatomical structures present in computed tomography (CT) images.

Chapter six describes methods for the segmentation of airways. It includes a review of state-of-the-art methods, talks about their relevance in the context of COPD, and discusses reasons for airway segmentation. In this chapter, the novel, unsupervised airways segmentation method is proposed.

Chapter seven covers the core of the dissertation, the segmentation of low-attenuation patterns. It begins with a description of current state-of-the-art methods in this domain, followed by an analysis of the scope of the lesions identified for segmentation within this study. Then, two distinct methods for segmenting low-attenuation patterns are introduced and evaluated.

Chapter eight presents the final component of the proposed pipeline, which involves grouping low-attenuation changes. Beginning with the state-of-the-art analysis, a method is proposed for assessing segmentation results by embedding their features into a 2D space and evaluating the effectiveness of the grouping.

Chapter 2

Technical background

2.1 Computed Tomography

Computed tomography is an imaging method that allows one to gather information on the amount and type of material present inside an object in a non-invasive way (Figure 2.1a). For this, X-ray radiation is used [10], a form of high-energy wave propagating through space, interacting with the encountered atoms. As an X-ray beam passes through an object, it is gradually absorbed or scattered. What remains reaches the detector placed on the opposite side of the object. X-rays are passed through the object at various angles, allowing the image to be reconstructed in three dimensions (Figure 2.1b). The technique has gained great popularity in the medical field because it allows a precise analysis of a selected body part.

(a)

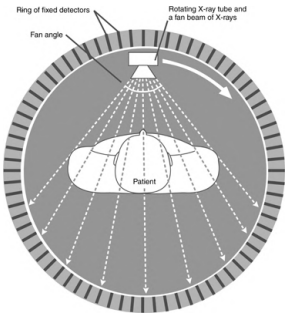

(b)

Figure 2.1: Example Computed Tomography scanner and ideogram showing core working principles a) Siemens SOMATOM Force CT scanner [11], b) X-ray generator rotates over the patient's body emitting X-ray beams which are scattered and absorbed by patient's tissues reaching the detector on the opposite side [12].

2.2 Hounsfield units

Hounsfield units (HU) scale is a quantification metric scale that describes the radiodensity of tissues and substances on the CT image. It is adjusted to the nominal value of water and air under standard temperature and pressure (STP), which is 0 degrees Celsius and a pressure of 100 kPa. This results in a normalised scale where water is represented by the value 0 HU and air is represented by -1000 HU. Hounsfield units result from the linear transformation of the measured attenuation coefficient of structures in the patient's body, which is a measure of the extent to which the radiation beam is weakened by passing through the material [13].

Typically, in chest CT images, Hounsfield voxel values range from -1024 to about 2000. Values around -1024 represent air; in the lungs, despite being largely filled with air, HU values ranging from -900 to -500 are observed. This is due to the presence of alveoli, which are denser than air. The majority of tissues and muscles lie in the range of -100 to 100 HU. Values above 100 HU are reserved for bones and other dense materials that may appear during the scanning procedure [14].

2.3 Storage standard

CT images are stored on the disk using the DICOM file standard. DICOM (Digital Imaging and Communications in Medicine) is a file type created for storing, managing, and diagnosing medical images. DICOM files consist of the image and the header, which stores metadata. The CT series is stored in separate DICOM files, slice by slice, each file connects to the next and previous by information stored in the header.

2.4 Patient, study and series

When a Computed Tomography study is stored on disk, a unique patient identifier is assigned or associated with the patient. The study is characterised by a unique identifier called the 'Study Instance UID'; additionally, it is identified by 'Accession Number' for human consumption. A study usually consists of multiple CT series, such as CT scans reconstructed using different reconstruction methods, in-plane view projections, image copies divided into subareas, segmentations and studies with contrast in different phases. In addition, descriptions of the disease or a report of the radiation

dose to which the patient was subjected during the examination are included. Each series has its unique identifier called 'Series Instance UID'. Each mentioned identifier is unique in the scope of the facility; although it is highly unlikely that two different facilities would have different studies with the same identifier, this option cannot be ruled out.

2.5 Slice thickness

A 3D CT image is created by assembling axial cross-sections stored within the DICOM files. Cross-sections in the form of 2D images are taken at a certain distance from each other; the distance at which they lie in physical space is called slice thickness. Slice thickness directly affects the amount of information contained in a CT image. A high slice thickness value can cause clinically relevant lesions to be missed. However, setting a lower layer thickness leads to exposing the patient to a higher radiation dose. Therefore, the layer thickness is adjusted according to the purpose of the radiographic examination [15].

2.6 Scanner parameters

Scanner parameters are dictated by the investigated body part, the patient's condition, scanner capabilities, and the desire to minimise the radiation dose absorbed by the patient. Differences in the parameters of CT scans create the greatest differences in the quality of the patient's tissue image. Many studies can be found in the literature that discuss the importance and effects of appropriate parameter selection [16, 17, 18, 19]. Parameters with the greatest impact on image quality include detector configuration, tube current, tube potential, reconstruction algorithm, patient positioning, scan range, reconstructed slice thickness, and pitch [19].

The parameters most commonly tweaked are the kilovoltage peak (kVp) and milliampere seconds (mA) because they have to be adjusted for each patient individually [20, 21]. The aforementioned kVp is related to the potential of the X-ray tube accelerating electrons travelling from the cathode to the anode. Controls the quantity and quality of the protons generated. The mAs measure tube current in the span of 1 millisecond. When other parameters are constant, the higher the mAs value, the

more electrons in the tube are gathered, which results in more X-ray photons passing through the patient, leading to better image quality with less noise but increasing the radiation dose. In contrast, lower mA values reduce the radiation dose but can increase image noise and potentially lower image quality [16, 17]. Those two parameters have the greatest influence on the radiation dose to which the patient is exposed during examination.

The radiation dose absorbed by the patient during the examination is an important topic in radiology [22, 23]. The kVp and mAs are one of the most important parameters influencing the strength of the radiation beam. Therefore, depending on the exam goal, different parameters are used. In the scope of the dissertation, it is important to differentiate between so-called low-dose studies and high-dose studies (standard dose), which are discussed in more detail later in the work.

2.7 Scanner model

The market today features a wide array of Computed Tomography scanner manufacturers, including notable names such as SIEMENS, Philips, Toshiba, UIH, and GE Medical Systems. Each of them has its own set of reconstruction kernels, filters, radiation beam optimisation methods, and different scanner designs. Consequently, each is different. Competition is good for progress; however, it also has its negative sides, one of which is the lack of homogeneity.

2.8 Convolution Kernel

Each manufacturer has its own set of convolution kernels. A convolution kernel is a mathematical matrix or algorithm applied to CT data during image reconstruction to emphasise specific image characteristics, such as edges or soft tissue contrast. It directly affects the sharpness and noise of the reconstructed CT images [24, 25]. The convolution kernels can be divided into three groups: sharp kernels, smooth kernels, and standard kernels.

Sharp kernels enhance the edges of structures and high-frequency details. They are commonly used in bone imaging and lung imaging when the lung nodules are the subject of investigation. Examples of the sharp convolution kernels are SIEMENS

B70s, Toshiba FC81 or GE SHARP. The disadvantage of sharp kernels is that they increase the noise in the CT image [25].

Smooth kernels reduce noise and smooth the image while maintaining overall contrast, making them ideal for detecting subtle differences in tissue densities. They are used for soft tissue imaging like abdominal organs, the brain, the liver, the kidneys, and some parenchymal structures. Examples of smooth kernels are SIEMENS B30s, Toshiba FC03 or GE SOFT. Kernels from this group might blur fine details [25].

Standard kernels provide a compromise between spatial resolution and noise. This is a general-purpose group of kernels which can be used for analysis of all body structures. Examples of standard kernels are SIEMENS B40s, Toshiba FC08 or GE STANDARD [25].

While this is not a rule, most manufacturers give the kernel name values where the higher the value, the sharper the kernel. Notably, GE names their convolution kernels using the name of the group they belong to.

2.9 High and Low dose CT

High-dose and low-dose CT differ, as the name suggests, in the amount of radiation dose delivered to the patient during the examination. The negative effects of X-rays on the human body are well known. It is important to minimise the amount of radiation the patient is exposed to during the examination. However, the amount of radiation translates into the quality of the resulting image. Therefore, to make the study effective and safe, the X-ray beam's strength must be properly tuned. There are many standards in which CT examinations are performed, but their general division can be limited to two groups, high-dose and low-dose examinations [25].

High-dose examinations are also known as high-resolution CT (HRCT). They are performed when an accurate picture of the patient's lesions is needed because the abnormal lesions are not known or the surgeon must plan the surgery [26].

Low-dose CT (LDCT) examinations are recommended, especially when a patient belongs to a group with a high risk of cancer development and are commonly used for screening [27, 28].

Regarding the series characteristics, HRCTs typically have a lower slice layer thickness and, therefore, more cross-sections. LDCTs typically have about twice the thick-

ness of the slice layer compared to HRCTs, which translates to a much lower number of cross-sections. HRCTs, compared to LDCTs, have significantly fewer occlusions; the image is much clearer, and the structures present in the patient's lungs are better defined [19].

2.10 Anatomical factors influencing results

The above-mentioned technical factors impact the resulting appearance of the CT image. It is necessary to tailor the scanning protocol parameters to suit the patient's physical condition. Aside from the patient's health status, two important considerations are emphasised during the examination: the patient's age and size.

The patient's age is a proven strong factor that influences the amount of airspace. This translates directly into the values of the CT density parameters [29]. This is a factor considered in most long-term studies. This is confirmed by a 5-year study conducted in a group of healthy people where their respiratory capacity was tested each year. The percentage of relative lung fragment area was shown to be less than -960 HU, which increases with age [30].

As the passing radiation beam through the patient's body is attenuated, naturally, the size of the scanned object has an impact on the result. The parameters of the CT scanners must be adjusted to the patient's size. Usually, it is done by analysing the patient's BMI index [20]. This results in the tweak of the kilovoltage peak (kVp) parameter and a change of the milliampere-second (mA) parameters, changing the strength of the beam.

Chapter 3

Biological background

To support this thesis, a basic understanding of lung anatomy is necessary. Since the research focuses on detecting lung abnormalities, it is important to examine their origin, appearance, and methods of measurement. This section will cover the medical aspects of the study, primarily discussing the human respiratory system as seen in computed tomography (CT) images. It will first explain lung function and the CT imaging process. Then, it will define lung abnormalities and describe their characteristics. The discussion will also include an analysis of lung diseases relevant to the thesis. Finally, it will explore methods for measuring disease severity.

3.1 About human lungs

Lungs are pyramid-shaped paired organs located in the human thorax, bordered from below by a diaphragm. They are elastic structures that expand and contract to suck in and drive out gases. The average weight of the lungs is 850 grams for a man and 750 grams for a woman. The right lung is divided into three lobes: upper, middle, and lower, while the left lung is divided into two lobes: upper and lower. Fissures separate lobes. The lung's main function is to support the exchange of oxygen and carbon dioxide. They are connected to the outside by the trachea, which conducts the gases and distributes them using the right and left bronchi. There are no solid attachments between the lungs and the walls of the chest cage (except the place where the hilum connects to the mediastinum). Instead, lungs are held in the chest by the thin layer of pleural fluid which envelops them, keeping them in place but allowing free

expansion and contraction of the organ [31, 32, 33].

3.2 Lung Parenchyma and Intersitium

Lung parenchyma is the functional part of the lungs responsible for gas exchange. It consists of multiple spherical structures called alveolar sacs in which carbon dioxide is exchanged for oxygen. Alveolar sacs are connected through alveolar ducts, airways, and trachea to the esophagus [34].

The lung parenchyma is supported by a connective tissue called the lung interstitium [35]. It could be assumed as a composition of several components. The peribronchovascular interstitium is a system of connective tissues enclosing the bronchi and pulmonary arteries. The centrilobular interstitium is a peripheral continuum of the interstitial fibre system. Peribronchovascular interstitium and centrilobular interstitium make up the so-called "axial fibre system" extending from the pulmonary hila to the alveolar ducts and sacs. The intralobular interstitium is a network of fibres filling the gap between the centre of lobules and the interlobular septa. The interlobular septa and subpleural interstitium are a part of the "peripheral fibre system". Subpleural interstitium envelops the lung; it mainly contains small vessels, which are involved in the formation of pleural fluid. Subpleural septa extend inward from the pleural surface and carry pulmonary veins and lymphatics. It separates lobules, forming borders between them.

3.3 Airways

In the lung interstitium lie the airways. They are a series of branching tubes which become shorter and narrower as they go deeper into the interstitium. The respiratory passages start with the trachea outside the lungs, splitting into the right and left main bronchi. These further divide into lobar and segmental bronchi before finally branching into bronchioles. In an adult human lung, there are typically twenty-three branching points before reaching the gas exchange regions known as alveoli. The airways are classified as either bronchi or bronchioles. The bronchi are tubes which have more than 0.1 cm in diameter and have cartilaginous walls, while the bronchioles do not have cartilaginous walls and have less than 0.1 cm in diameter [36].

The airways could be divided by their function into conducting, transitional and respiratory zones presented in Figure 3.1a. The conducting zone consists of the trachea, bronchi, bronchioles and terminal bronchioles. Its goal is to deliver inspired air to the gas-exchanging region. The transitional and respiratory zones consist of respiratory bronchioles, alveolar ducts and alveolar sacs. The alveolar region is the region of gas exchange. The conducting zone is an anatomic dead space; it does not take part in the gas exchange and has a volume of about 150 ml. The transitional zone, as the name suggests, serves as a transition between the conducting and respiratory zones. It is interspersed with the budding of alveoli; the closer the alveolar sacs are, the denser the alveoli. The alveolar sacs in the transitional and respiratory zones are responsible for gas exchange. The transitional and respiratory zones account for approximately 2.5 to 3 litres of the lung's volume [37].

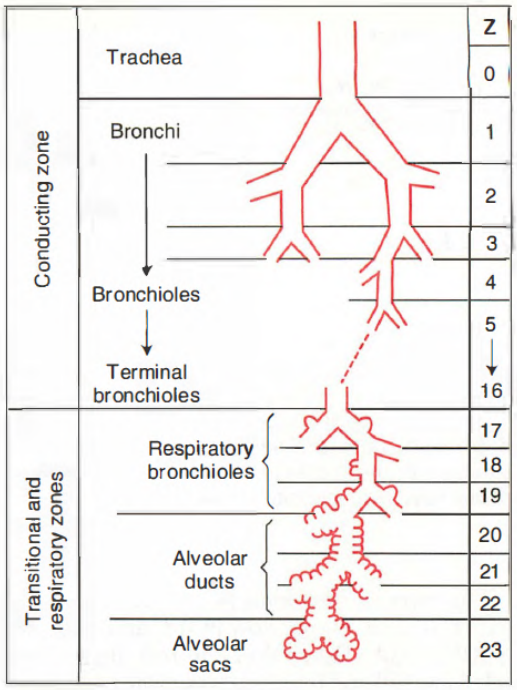

(a) Structural diagram of the structure of bronchial tree.

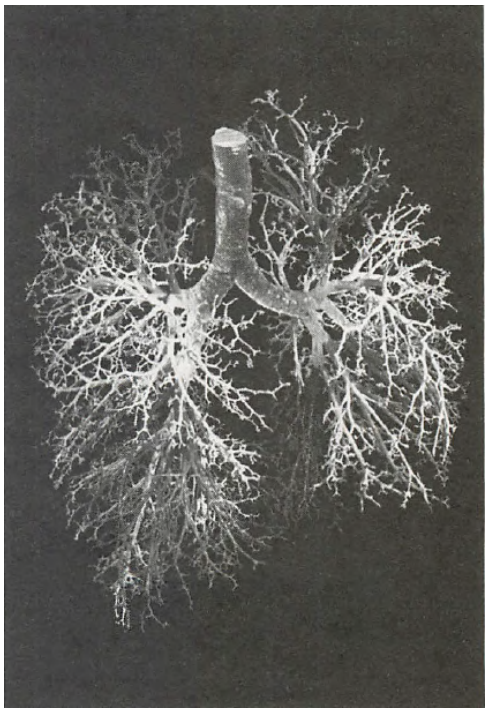

(b) Human bronchi 3D visualisation.

Figure 3.1: Airways of the Human lung with the airways division ideogram according to the Weible [37].

3.4 Pulmonary arteries and veins

Running alongside the bronchus, the pulmonary arteries and veins are located, which facilitate the circulation of blood between the lungs and the heart. Pulmonary arteries carry deoxygenated blood from the heart to the lungs, while pulmonary veins carry oxygenated blood from the lungs to the heart. They branch in multiple directions and follow bronchi. As the pulmonary artery nears the alveoli, it becomes a pulmonary capillary network, consisting of tiny vessels with thin walls without muscle fibres. Enveloping the alveoli, the pulmonary capillary creates the respiratory membrane responsible for the gas exchange [38].

3.5 Blood-Gas barrier exchange

The blood flows from the high-pressure arteriole carrying carbon dioxide to the lower-pressure venule to where oxygen is distributed. Then the pulmonary capillary branches to the pulmonary vein, which transports the oxygenated blood to the heart, which distributes it to the other parts of the body. Pulmonary capillaries are extremely thin structures located in the walls of the alveoli. The total area ranges between 50 and 100 m^2, with half featuring a thickness of 0.2 to 0.3 μm, creating an optimal setting for diffusion.

3.6 Abnormal patterns in lungs

This section is intended to highlight the main abnormal lesions studied. Detection of lung abnormalities is the main topic of the dissertation. Lung abnormalities refer to any alterations linked to diseases impacting the lung parenchyma, visible in Computed Tomography scans. A variety of abnormal lung patterns exist, but for ease of discussion, they can mostly be categorised into two groups: low-attenuation patterns and high-attenuation patterns.

Low-attenuation patterns are visible on CT as darker patterns (lower value) than the surrounding lung parenchyma. Usually present as a result of obliteration of the alveoli or excessive presence of air in the enclosed pocket. To this category of abnormalities belong emphysema and air trapping [39, 40].

High-attenuation patterns are visible on CT as brighter patterns (higher value) than the surrounding lung parenchyma. Usually present due to flooding of the alveoli and bronchi with fluid such as water or blood, calcification, fungal infections, cancer, or the presence of foreign bodies [41, 42, 39].

The proposed division into high and low attenuation patterns is not fair, as shape, location, and surroundings are important in the categorisation of abnormal lesions. Especially in the case of the high-attenuation group, which has more underlying patterns than the low-attenuation group. In medical literature, the high attenuation patterns are usually additionally split into subcategories [43]. Separate categories are given for the opacification resulting from fluids, lung nodules, and foreign bodies, where the nodules are then additionally divided.

Within the scope of this study, access to data is limited, preventing the evaluation of the algorithm introduced in this thesis on all types of abnormal lesions. The analysis was focused on emphysema and air trapping. An algorithm was developed and tested specifically for these two abnormalities. Furthermore, it is assumed that the medical practitioner examining a patient has a preliminary suspicion of the condition based on external tests or physical examination.

3.6.1 Emphysema

Emphysema is defined as a permanent abnormal enlargement of the air spaces distal to the terminal bronchioles, accompanied by destruction of the walls of the occupied air spaces [26]. Emphysema can be accurately diagnosed by HRCT [44, 45] or, with less precision, detected by low-dose CT [46, 47]. It results in focal areas of very low attenuation that can be visually contrasted with the surrounding normal lung parenchyma with higher attenuation if sufficiently low window values are used (-700 to -950 Hounsfield units [HU]). Although some types of emphysema may have walls visible on HRCT, they are usually inconspicuous. In the case of the low-dose CT, the walls are not visible at all, which makes it easy to confuse emphysema with air trapping. Based on the High Resolution Computed Tomography image, it is possible to classify emphysema into subcategories [44].

Cenrilobular Emphysema

Centrilobular emphysema (CLE) is the most common subtype of emphysema. It is characterised by the destruction of the alveolar septa in the centres of alveoli and pulmonary lobules. The CLE usually affects the posterior segments of the upper lungs [48]. On CT images, they show up as round black holes (low attenuating) that are evenly distributed in the lung. Usually, even on HRCT images, CLE walls are not visible [26] (Figure 3.2a).

Panlobular Emphysema

Panlobular emphysema is usually the result of severe or confluent CLE. It is characterised by uniform destruction of the alveolar septa in the lung parenchyma distal to pulmonary bronchioles [48]. On the CT image, it shows up as a large dark area where the pulmonary vessels are not visible [26] (Figure 3.2b).

Paraseptal Emphysema

Paraseptal emphysema, while it can be an isolated abnormality, usually appears with the presence of CLE. It is characterised by the destruction of the most distant alveoli in the subpleural space, sparing the respiratory bronchioles. On CT images, it shows up as subpleural lucencies with very thin but visible walls on the HRCT image [48, 26] (Figure 3.2c).

(a) (b) (c)

Figure 3.2: Emphysema sub-types ideograms a) centrilobular emphysema; b) panlobular emphysema; c) paraseptal emphysema [49].

Bullae and Bullous Emphysema

Bullous emphysema, also referred to as vanishing lung syndrome [50], is a large pathology that is not directly related to any other subtype of emphysema. It is characterised by a sharply delimited region of emphysema seen as a large dark region, at least 1 cm in diameter, with thin walls around 1 mm. Bullae can go up to 20 cm in diameter but usually have about 5 to 8 cm [50]. It is asymmetric and usually has clearly defined walls, making it hard to distinguish it from the lung cyst [51, 26] (Figure 3.3a).

3.6.2 Air trapping

In its advanced stages, emphysema can cause what is known as air trapping. This is an abnormal lesion defined as the retention of excess gas in the lungs, causing respiratory obstruction. On CT images, it manifests itself as an area of reduced attenuation that is strictly separated from the rest of the lung parenchyma. In addition, vessel occlusion is usually observed in this area (Figure 3.3b). While it is very similar to bullae emphysema, this area usually is not delimited by fibrosis; also bullae emphysema tends to be a result of paraseptal emphysema, meaning that it usually occurs on the lung's parenchyma border. The differences could be observed in Figure 3.3.

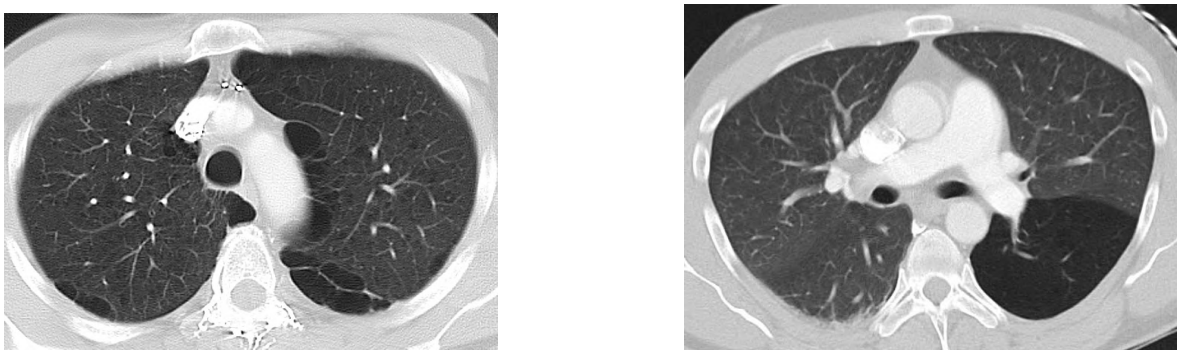

(a) (b)

Figure 3.3: Side by side comparison between a) subpleural bullae emphysema [52], and b) air trapping [53], on the Computed Tomography images.

3.7 Chronic Obstructive Pulmonary Disease

Chronic obstructive lung disease (COPD) is a progressive lung disorder that obstructs the airflow. Symptoms of COPD are coughing, production of mucus, shortness of breath (especially during exercise), wheezing, tightness in the chest, fatigue, and frequent respiratory infections. Key characteristics of the disease include irreversible airflow limitation, progressive nature if untreated, and periodic exacerbations of symptoms (for example, coughing fits and excessive mucus production). COPD is characterised by two disease entities: small airway inflammation and emphysema.

Many studies identify smoking as the predominant factor causing COPD and a significant contributor to COPD mortality in developed countries. Lundbäck et al. study identified that nearly 50% of chronic smokers develop COPD [2]. Air pollution, including particulate matter, is another important risk factor for COPD. Both cigarette smoking and air pollution have been identified as significant factors for COPD development. Yet the difference in their prevalence lies in the geographical location; in highly developed countries, cigarette smoking constitutes 70% of the COPD burden, while in middle-to-low developed countries, environmental exposures account for 60% of the COPD burden [1]. This difference is due to poor planning decisions of cities from low- to middle-developed countries regarding factory and residential area placement, poor living conditions, and the popularity of biomass burners [1, 3, 4]. Aside from lifestyle and environmental factors, the deficit of alpha-1-antitrypsin (AAT) is also a proven risk factor [54]. But in contrast to the previously mentioned factors, it is not a direct cause of COPD.

Tobacco smoke contains many harmful substances that damage the bronchial and alveolar epithelial cells, causing inflammation. Sources state that the onset of COPD is the aforementioned inflammation of the small airways, which is a common feature with asthma [55]. However, the inflammation in COPD differs from that in asthma; in COPD an infiltration of inflammatory cells such as neutrophils, macrophages and T lymphocytes is observed, particularly in the small airways and lung parenchyma [56]. In asthma, eosinophils and mast cells predominate [57]. An important difference between COPD and asthma is the presence of emphysema. It occurs through an imbalance between protease and antiprotease. Protease is an enzyme that breaks down proteins, including elastin, an important component of connective tissue in the lungs. Smoking increases the production of proteases such as neutrophil elastase [58, 59]. Alpha-1-antitrypsin (AAT) is the main inhibitor of elastase in the lung. AAT binds to elastase

and neutralises its action, protecting lung tissue from degradation. Therefore, people with AAT deficiency are more likely to suffer from the effects of COPD. The degradation of elastin contributes to the loss of alveolar elasticity, resulting in alveolar destruction. Alveolar destruction leads to a reduction in the total surface area available for gas exchange (oxygen and carbon dioxide). Loss of elasticity, alveolar destruction, and reduced gas exchange surface area lead to impaired lung function and the formation of emphysema [60, 61, 62].

As COPD is an untreatable disease, external medications and treatment can only improve life quality and halt disease progression. Of the medicines popularly used, drugs from the bronchodilator group are commonly recommended to relax airway muscles, improving airflow. Additionally, corticosteroids are used as accompanying or independent of bronchodilators [63, 64]. Other than that, oxygen therapy is often recommended to maintain adequate oxygen levels. Additionally, patients are instructed to exercise and follow a healthy lifestyle to soften the COPD symptoms. The most important factor in reducing the severity of symptoms is to cease smoking or not smoke cigarettes; yet it does not remove symptoms completely [3, 62].

3.8 Quantification of emphysema and COPD

Quantification of COPD refers to measuring and evaluating the severity and impact of COPD. This quantification involves using clinical, physiological, and imaging tools to assess the degree of impairment of lung function and structural changes in the lungs, allowing personalised disease management and monitoring.

3.8.1 Spirometry

Spirometry is a method that is used to measure the limitations of airflow. The test is performed using a spirometer into which the patient blows air. It is one of the first tests carried out when COPD is suspected, as it is relatively simple, noninvasive, and does not expose the patient to harmful radiation. The test results in 2 coefficients, FEV_1 (forced expiratory volume in 1 second), the amount of air exhaled in the first second of a forceful breath, and FVC (Forced Vital Capacity), the total amount of air exhaled during the test. The $\frac{FEV_1}{FVC}$ ratio is a key indicator of the severity of COPD disease, and a graded scale of disease severity called the GOLD standard has been

created concerning this indicator.

The GOLD (Global Initiative for Chronic Obstructive Lung Disease) standard is a numerical scale ranging from 1 to 4 that represents the severity of emphysema. Based on FEV1 in relation to the reference value (the value expected for a healthy person with similar parameters such as age, sex, and height), the GOLD value standard is assigned to the patient. The GOLD 1 (mild COPD), where FEV1 is 80% of the reference value. At this stage, the disease may be asymptomatic, or there may be mild breathlessness on greater exertion. The GOLD 2 (moderate COPD), where FEV1 ranges from 50% to 79% of the reference value. More breathlessness occurs, especially during physical activity, along with a chronic cough and sputum production. The GOLD 3 (severe COPD), where FEV1 is between 30% and 49% of the reference value. Symptoms become more severe, and breathlessness occurs even during low exertion. GOLD 4 (very severe COPD) where FEV1 $< 30\%$ of the reference value or $< 50\%$ of the reference value with chronic respiratory failure. At this stage, patients are severely limited in their ability to perform daily activities and may require oxygen therapy [65].

3.8.2 Symptomatic and quality of life check

Another example of a non-invasive method of determining the condition of a patient with suspected COPD is the symptomatic assessment and surveys that check the patient's quality of life. There are two leading methods for conducting such a survey, the first is the COPD Assessment Test (CAT) recommended in the GOLD 2011 guidelines and the second is called the modified Medical Research Council (mMRC) dyspnea scale. CAT is a self-administered survey designed to measure and quantify symptoms and the impact of COPD on health-related quality of life. It consists of 8 questions, each rated on a 6-point scale (0 to 5), giving a total score of 40. Scores of 0-10 indicate mild COPD, 11-20 moderate COPD, 21-30 severe COPD, and 31-40 very severe COPD [66]. The mMRC scale, on the other hand, is a 5-point (0 to 4) scale that rates the severity of breathlessness. It is an old scale composed of simple questions [67].

3.8.3 Macroscopy and microscopy

Macroscopy Evaluation of Emphysema refers to quantifying abnormal patterns using 'naked eye' or low magnification tools. Macroscopy quantification is usually based on the lung section or the radiogram of the patient's lung. An example of the

macroscopy approach is the point counting method proposed by Dunil et al. [68] where on the lung section, the transparent sheet of glass with the grid is laid. Based on the overlayed grid, the proportion of the emphysematous lesion is calculated in relation to the healthy lung. Another example of macroscopic evaluation is the panel grading method proposed by Thurlbeck et al. [69] where a paper lung section is used and scored from 0-100, reflecting the severity of the emphysema. Similarly to both methods, the Ryder Grid method [70], where the lung section is overlayed with a transparent radiating grid placed along the greatest fissure, based on which the extent of emphysema is graded from 0 to 5, reflecting the extent of emphysema. All mentioned methods originate from the years 1960 to 1970, so they are relatively old. It is now known that a single lung section is insufficient to measure the extent of emphysematous changes [71]. Additionally, the focus is on the early detection of changes in living specimens rather than postmortem analysis. Modern macroscopic methods rely on medical imaging techniques.

Microscopy methods analyse lung tissue on a cellular level, often revealing more subtle changes that are not visible macroscopically. The evaluation is usually based on the lung biopsy or histology image analysed under the light microscope or electron microscope. As the patterns of the disease are more subtle, the measures that quantify them are more diverse. There is the mean linear intercept (Lm) measure describing the number of walls of alveoli crossed by the test line placed on the sample [68]. The airspace wall per unit volume (AWUV) measures the surface area of the alveoli per unit volume of the lungs [72]. The destruction index (DI) measures the level of alveolar destruction by representing it as a percentage value [73]. In the scope of this dissertation, microscopy quantification metrics will not be used, as the imaging type required for these types of measurements does not involve computed tomography.

The goal of microscopy and microscopy quantification methods is the same, but the way they achieve their goal is different. For clarity, the main differences are listed in Table 3.1.

3.8.4 Image analysis

Chest CT is the most common imaging technique used in clinical practice to analyse lung lesions. This non-invasive method exposes the patient to harmful radiation in exchange for a detailed image of the lungs. It detects subtle structural changes in the

Aspect	Macroscopy	Microscopy
Scale	Large-scale (visible to the naked eye)	Small-scale (cellular and tissue level)
Tools Used	Naked eye, low magnification, CT scans	Light or electron microscope
Focus	Overall lung structure and gross damage	Cellular and tissue-level damage
Findings	Emphysema, bullae, loss of tissue	Alveolar wall destruction, enlarged airspaces
Purpose	To evaluate the extent and distribution of the disease	To understand the structural and cellular changes
Usage	Clinical imaging, surgery, autopsy	Biopsy, research, detailed histopathological evaluation

Table 3.1: Summarisation of the differences between macroscopy and microscopy quantification methods.

lung parenchyma, such as emphysema, thickening of the airway wall, and air trapping. Experienced radiologists do not mark the locations of the lesions when describing the images and can easily identify them. However, they often need information on the distribution and volume of the lesions to plan further treatment. To partly automate the process, physicians and medical scientists tend to use simple solutions, such as the use of fixed cutoff thresholds for voxel intensity values in Hounsfield units or the use of the nth cutoff percentile in the attenuation distribution curve to create a density mask. From such a density mask the different metrics can be calculated.

The most commonly seen is a metric called the "low attenuation area" (LAA), which is the volume of the low attenuation area divided by the total volume of the lungs represented as a percentage (%). Usually, it appears with the specific threshold used, for example, -950 HU is denoted as LAA_{-950}. Another less common metric is the fractal dimension, which measures the wellness of the fit of fractals in the space of the given volume. It is used to describe shapes and structures of an irregular form. It is used for the analysis of cluster voxels that creates emphysematous lesions and to evaluate the progression of the disease [74, 75].

Many studies in the literature suggest optimal cut-off thresholds for finding disease

masks. The first study to analyse differences in grey level intensity between healthy tissue and emphysematous lesions was that of Hayhurst et al. [76], which showed statistical differences in grey level distributions in the lung parenchyma between healthy subjects and those with multiple emphysematous changes. The scientists noticed that the values characterising the emphysematous lesions were found on the left side of the CT histogram, allowing segmentation using a low threshold in the HU space. Since then, many studies have attempted to find a single universal cut-off point for emphysematous lesions.

The study by Muller et al. [77] suggests the use of a cut-off threshold of -910 HU with a section thickness of 10 mm, supporting the conclusions with a correlation of the lesion density mask and the visual assessment of lesions. A study by Gevenois et al. analysed cross-sections of 63 patients for whom thresholds of -900 to -970 HU were checked and concluded that a threshold of -950 HU should be used for objective quantification of emphysema [78]. Madani et al. [79] studied 80 patients with images taken with multi-detector row CT with 1.25-mm-thick sections. She tested different fixed cut-off thresholds and thresholds determined from percentiles of voxel intensity values. The authors recommend using cut-off thresholds of -960 HU or -970 HU. The findings support the correlation with microscopic and macroscopic evaluations of lesions. A study by Bankier et al. analysed CT cross-sections taken from 62 patients and the density mask correlations with macroscopic morphometry findings. The authors used a cutoff point of -950 HU [80] in the study. Studies using remarkably high thresholds such as -900 HU can also be found in the literature. Kishi et al. [81] studied the correlation between the occurrence of lung cancer and emphysema. The study involved 1,520 people; however, 24 people diagnosed with lung cancer and 84 healthy individuals were used for the correlation analysis. The study used a threshold of -900 HU values to separate emphysema from the rest of the lung. A study by Maldonado et al. [82] investigated the correlation between emphysematous changes seen on CT and airflow obstruction in 64 patients with lung cancer and 377 control patients. A threshold of -900 HU was also used to define areas of emphysema. Stern et al. [83] in their study on the challenges of diagnosing and quantifying pulmonary emphysema, employed a range of Hounsfield Unit (HU) values between -900 and -1000 as the thresholds for evaluating segmentation of emphysematous lesions. The study found that a threshold of -900 HU resulted in the most precise density masks.

As mentioned, in addition to fixed cut-off values, thresholds based on the percentile of the lung density histogram are also used. The study mentioned earlier by Madani

et al. [79], in addition to proposing fixed cut-off thresholds, as an alternative suggests using the 1st percentile of the lung density histogram as the cut-off value. Dirksen et al. [84] in their study, in which they investigated the presence of emphysema in patients with α_1-antitrypsin deficiency using CT images thresholded by the 10th percentile of the lung density histogram. Three years later, also under the guidance of Dirksen et al. [85], this time in a study related to the effect of α_1-antitrypsin supplementation on the behaviour of emphysematous changes, they used a threshold of 15 percentiles of the lung density histogram.

The mentioned studies show that it is difficult to find a universal, single cut-off threshold for emphysematous lesions. The experiments were conducted in different years, with the technology moving forward and scanning parameters changing. Different layer thicknesses were used between studies, different numbers of cross-sections were tested, and scanners of different brands were used. The severity of emphysematous changes also varied between studies; small areas and early appearances of emphysema mean less destruction of the alveolar walls, leading to higher HU values, which may not be included in thresholds such as -950 HU or -970 HU. However, when there is a severe case of emphysema, a high threshold, such as -900 HU, can lead to over-segmentations. A fixed threshold ensures that a specific percentage of lesions will be accurately detected, though a significant number of over-segmentations and under-segmentations accompany it. The bronchial tree stands as an instance of systematic over-segmentation within the explored HU unit range, containing pure air that fluctuates around -1000 HU values. When it comes to the accurate separation and analysis of emphysematous changes in the lungs of patients and the early diagnosis of emphysema, the use of fixed thresholds or percentile-based determination is insufficient.

Chapter 4

Materials

The Materials section will discuss the datasets used in the dissertation's scope. All described datasets contain CT images of the chest. The dissertation used both high-resolution computed tomography (HRCT) and low-dose computed tomography (LDCT). LDCT was used mainly during the development of the airways modelling algorithm. As HRCT is the main subject of the thesis, HRCT images were used to develop an algorithm to seek emphysematous changes and used for their quantification.

4.1 COPDGene

The COPDGene dataset results from a study carried out by a group of researchers from 21 institutes in the USA [86]. The study was divided into four phases and was carried out over many years, during which the researchers prepared the dataset. The original dataset consists primarily of genetic data and CT scan images taken in patients' full inspiration and expiration. Additionally, the dataset contains information such as age, sex, ancestry, scanner model, convolutional kernel, and GOLD classification of the patient. In the dissertation, 6078 CT series comprising 2243 unique patients were considered, as summarised in Table 4.1.

Manufacturer	Slice thickness [mm]	Number of series
GE Medical Systems	0.625	2414
	1.25	121
SIEMENS	0.75	3412
	1.0	75
Philips	0.9	56

Table 4.1: COPDGene summary of the computed tomography series used in the study.

The series are evenly distributed between those taken on inspiration and those taken on expiration, with smoothing restoration kernels (STD) slightly outnumbering those taken on inspiration, in both cases as presented in Figure 4.1. The number of series included in a given GOLD standard is not evenly distributed, the most common classification being 2 and the least common 1, as presented in Figure 4.2.

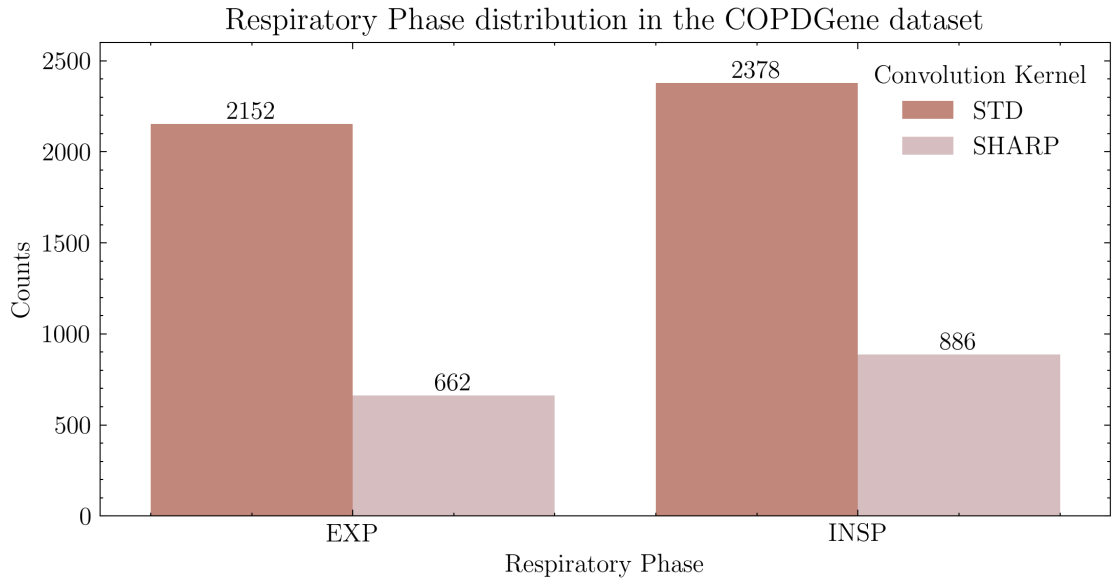

Figure 4.1: COPDGene used dataset CT series count divided based on the respiratory phase and convolution kernel.

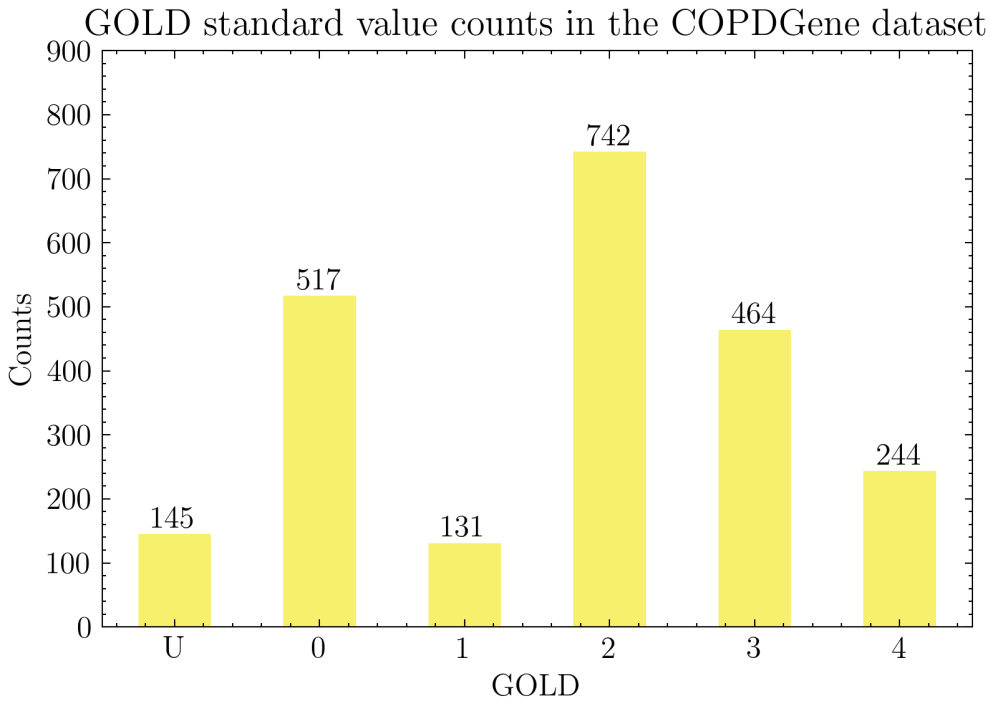

Figure 4.2: COPDGene used dataset CT series count divided based on the GOLD standard classification.

4.2 MOLTEST-BIS subset

The MOLTEST-BIS dataset is derived from a lung cancer screening study conducted between January 2016 and December 2018 [87, 88]. The study included patients in the 50-79 age range with a long-term smoking history. The study examined 6631 patients for whom at least one CT imaging study was performed. The study protocol was based on the United Kingdom Lung Screen protocol, with a follow-up after one year [89].

The dissertation used a subset of 1110 CT examinations from the MOLTEST BIS collection. It focused on patients whose CT images showed evidence of emphysematous lesions. In the scope of the dissertation, the dataset subset was used to test and validate the performance of the airways extraction method. Each scan considered in the study was made with a GE Medical Systems scanner with a STANDARD reconstruction kernel and 2.5 mm slice thickness.

Chapter 5

Lungs and Lobes segmentation

5.1 Motivation

The first and foremost important step in analysing pulmonary abnormalities in CT images is lung segmentation [90]. In this dissertation, lung segmentation refers to the accurate and automated extraction of the left and right lungs from the surrounding thoracic tissue. It is crucial to understand the significance of precision in this context, as any inaccuracies in lung segmentation could significantly affect subsequent analyses. Any tissue incorporated beyond lung tissue would be regarded as noise, potentially reducing the accuracy of the diagnosis. Conversely, omitting lung tissue might result in the loss of vital information concerning the disease progression and lower accuracy or confidence of diagnosis [91]. Lung segmentation is challenging due to the heterogeneous nature of the patient's condition and study environment. The appearance of abnormalities in lung tissues, resulting from ongoing or past diseases, may be omitted by segmentation algorithms due to the difference in the form and texture of the healthy lung.

In the case of lobes segmentation, in the scope of this dissertation, it serves as additional location information for automatic disease quantification. It is not vital for the start of the analysis, but it is important for the precise determination of the disease entity or sub-entity.

5.2 State of the art

In the literature, lung segmentation methods are distinguished into five categories: thresholding-based, region-based, shape- or model-based, anatomy-guided, and machine-learning-based [92, 93]. Thresholding methods are relatively fast but lack accuracy due to the vessels in the mediastinum, trachea, and other structures, which are confounding factors. They are rarely seen in modern literature because of the problems mentioned above. The thresholding is usually done automatically based on the given data with some additional processing [94, 95, 96]. Although there are not many practical use cases in automated systems, medical specialists still use thresholding methods in commercial applications and medical analysis programs to roughly segment the lung area during diagnosis. In addition, they can be used as a preprocessing step for the other methods.

Region-based methods are based on the assumption that neighbouring voxels on the CT image of the lung parenchyma have similar values. Their main advantages are the lack of supervision required and low computational complexity; on the other hand, they are susceptible to noise in the image, and some are heavily dependent on the initial seed. Before the rise of Deep Learning, region-based methods were the most popular lung segmentation approaches. The most popular method was the seed region growing algorithm [97], which segmented the region similar to the given seed voxel. Watershed is another popular region-based segmentation algorithm [98], treating pixel intensity values as topographical features and simulates a flooding process, where basins are formed around intensity minima, separating different objects in the image. Graph cut is another example of a segmentation algorithm in this category [99] it partitions an image into regions by optimising a graph-based representation of the image to find the optimal cut that separates objects or regions of interest. Although graph cuts were a popular image segmentation method in general, they were not widely used in the case of the lung segmentation problem.

Shape- and model-based methods were another step in the progress of lung segmentation systems. They used prior information about the shape or appearance of the lungs for segmentation purposes. They were the closest method to the currently most popular used deep learning approach and could handle mild and low-affected lung parenchyma [92]. Shape-based methods also called boundary-based, consist of methods employing algorithms like active contours [100, 101], snakes [102] or level-sets [103]. The above methods manipulate a preset contour based on user-defined forces

derived from image properties such as the gradient. Forces acting on the contour must be created to reproduce the target image, in this case, the lung parenchyma, which is one of the main challenges of this method [103]. This category consisted of supervised methods that were often taught in more than one CT series. The algorithms were taught the shape and texture of the lungs and, using the level set segmentation methods [100, 101], the lung parenchyma was extracted [104, 105, 106].

Anatomy-guided methods took a different route than other methods; instead of looking for the lungs, they analysed their vicinity looking for structures such as the carcass, heart, spine, liver, and mediastinum [107, 108, 109]. Based on the given locations or segmentation of other organs, methods in this class limit the search area of the lung parenchyma and then create its mask. This was the first group of lung segmentation methods that handled well the heavily afflicted lung [108], such as the cases with pleural fluid or extensive atelectasis. The disadvantage of these methods is that they assume that there are no abnormal lesions or diseases in the organs and structures near the lung area being examined.

The group of machine learning methods concerns all algorithms that learn from data. Based on the given samples, methods adjust internal parameters aimed at locating lung parenchyma in the CT series despite present abnormalities. As noted in the work of Carmo et al. [92], there is a need to additionally distinguish two subcategories in this category: traditional machine learning and deep learning.

Traditional machine learning was based on the extraction of features. In the train set, the region of the lungs was given a priori and based on it, algorithms extracted meaningful features, learning them in the process. Based on the learned features (parameters), the lung parenchyma was extracted. The early work focused on texture classification, which could be achieved by analysis of whole 3D series [110] or 2D series slices [111]. The most straightforward feature of the lung parenchyma is its attenuation value. Most of the developed algorithms used this property in conjunction with other features, which included local binary patterns, wavelets, grey-level statistics, and neighbouring structures [112, 113, 114].

Deep learning is currently the most popular method for lung segmentation. Many papers have been written on this subject, including papers describing per-slice approaches, i.e., based on a 2D slice of a CT image, and papers using a full 3D image of the series. The most commonly used architecture for this task is U-Net [115]. Established in 2015, it revolutionised the field of image segmentation by introducing so-called

skip-connections. U-Net, as shown in Figure 5.1, consists of two paths across the contracting and expansive paths. The first one gradually reduces the feature space by reducing the image's resolution while increasing its depth, creating the so-called image feature space. The second path receives the feature space from the contracting path and gradually increases its resolution while varying its depth. The expansive path's task is to create a mask of the target object based on the extracted features from the contracting path. The aforementioned skip-connection combines the corresponding block of layers in the contracting and expansive paths, passing the input from the contracting path to the expansive path. This provides additional information about the original object, provided the feature space is intended to describe the searched object, and the additional information provided directly by the contracting path allows it to be better located in space.

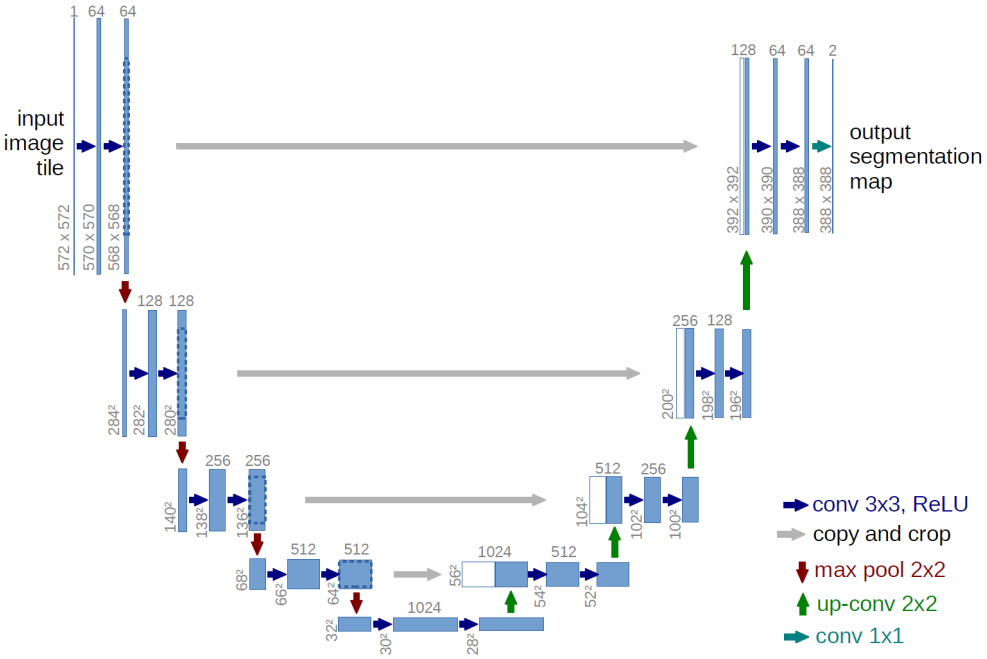

Figure 5.1: U-Net architecture overview [115].

There are many approaches utilising the U-Net original architecture either in the 2D form [116, 117, 118, 119, 120, 121] or in 3D form [122, 123, 124, 125, 126]. The difference between 2D and 3D U-Net networks is the form of convolution that occurs. In the case of 2D networks, convolutions are made with a rectangular window, while in the case of 3D networks, the convolution window is a cube. Each mentioned approach brings novelty in another form, experiment preparation, preprocessing of the CT data, or the

U-Net architecture modifications. In some cases, modifications to the method involve external support for network prediction through, for example, superpixel segmentation and contour refinement [127]. U-Net networks are most often modified by adding attention blocks, either a single block, for example, at the beginning of the network [128] or multiple blocks, for example, within residual connections [129]. Another example of U-Net modification is the addition of some additional layers, like Inception-based blocks hidden between the standard U-Net blocks [130]. U-Net is not the only network used for this task; models like ResNet18 [131], VGG-18 [132], or the ensemble of multiple architectures [133] are also used.

In the case of the lung segmentation task, there are a lot of public datasets with annotations available online, and the hand-annotation of the CT images for this task is not particularly hard. Although works that cover lung segmentation usually do not share a common benchmark, it is very hard to decide which solution is the best solely based on the provided in-paper scoring. Recent studies have questioned the need for additional modification of the U-Net, whether by attention modules or by adding additional blocks. The network no-new-Unet, which, as the name suggests, was a classic U-Net 3D architecture, proved that with a sufficiently diverse set, the U-Net network can outperform its modifications or extensions [134]. This further supports the claim made in the paper mentioned in the motivation by Hofmanninger et al., stating the significantly higher relevance of a diverse training set than the neural network architecture [135].

5.3 Results

Lung segmentation is a crucial step in the segmentation or detection of changes occurring in the lung parenchyma. Isolating this region reduces distortions that may affect the final result. A significant portion of the lung consists of voxels with low Hounsfield unit values, similar to those of air. However, certain structures within the lung parenchyma, such as blood vessels, exhibit high Hounsfield unit values. If only these structures fell within the high voxel value range, a simple thresholding method would be the most appropriate approach. However, abnormal changes in the pulmonary parenchyma, including consolidations and ground-glass opacities, also have high Hounsfield unit values. Although blood vessels are not required for analysis, eliminating any class of abnormalities at this stage would be a critical error.

To evaluate the hypothesis that segmentation based solely on thresholding of the grey-level intensity in CT images is insufficient, the effectiveness of classical thresholding was tested using the Otsu thresholding method. In addition to the Otsu method, the two areas containing the highest number of voxels were selected through an analysis of the merged regions, and the mask was refined using a morphological closure method. An example of the segmentation result is presented in Figure 5.2.

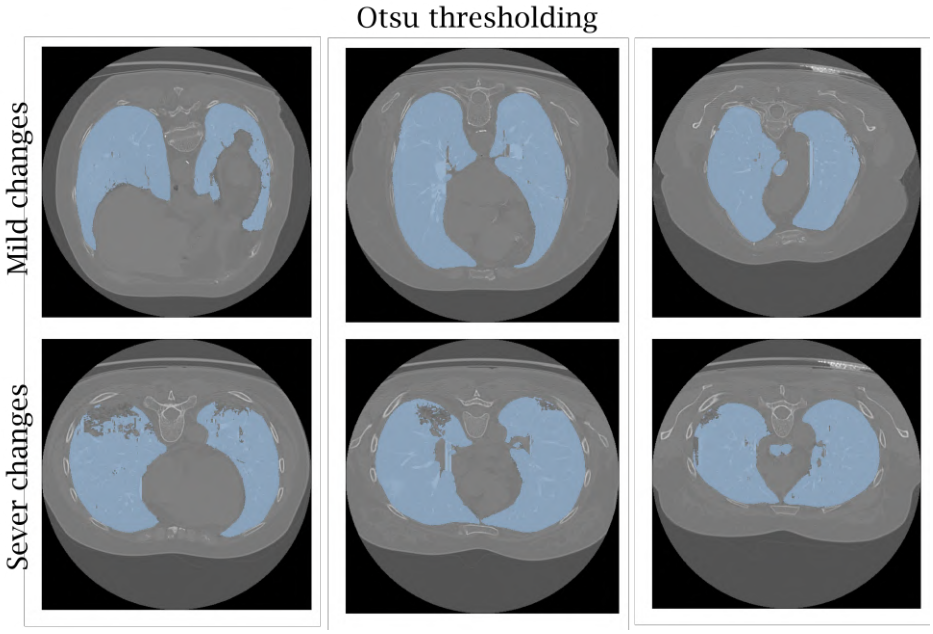

Figure 5.2: Example slices from patients with mild and severe abnormal parenchymal changes with overlayed results of the lung segmentation using the Otsu thresholding method.

A literature analysis showed that, in addition to thresholding methods and morphological operations, proliferation-based and level-set methods are also applicable to the task of lung area segmentation. Using the region-growing algorithm, lung segmentation was performed, where 5000 points were chosen from the thresholding-based method as starting points. The resulting mask was subjected to the same cleaning procedure as for the thresholding-based method. An example of the segmentation result can be seen in Figure 5.3.

The operation of the level-set method was examined using the Fast Marching algorithm as an example. This method functions similarly to region growing but relies on differences between neighbouring pixels rather than intensity differences. Its growth is controlled by a velocity map provided as input. In this case, the velocity map was

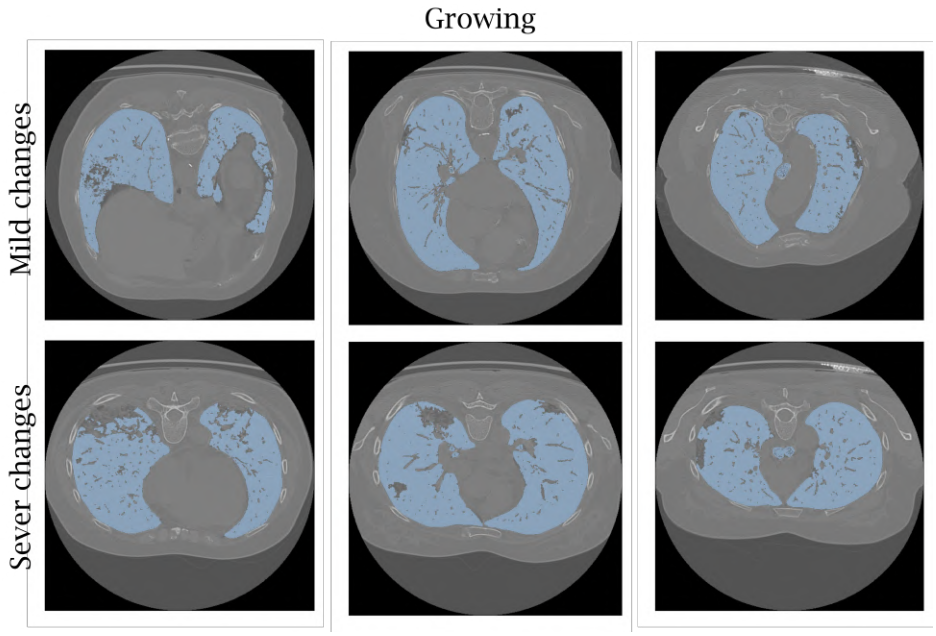

Figure 5.3: Example slices from patients with mild and severe abnormal parenchymal changes with overlayed results of the lung segmentation using the region growing method.

defined as an image gradient, scaled and constrained to a value of 1. An example of the segmentation result is shown in Figure 5.4.

Finally, the performance of neural networks was evaluated using the network designed and trained by Hofmanninger et al. [135]. The selection of this network from the available approaches was based on three main factors: the dataset used for training, the accessibility of the solution, and the relative simplicity of the proposed network. As discussed in the literature review, the U-Net 2D network was trained on a diverse dataset. The authors ensured that scans from different imaging machines and convolution kernels were included in the training set. Additionally, lungs affected by various types of lesions were incorporated to improve generalizability. The network is easily accessible, and the provided Python code is well-structured and robust against package conflicts. An example of the U-Net's segmentation result is shown in Figure 5.5. Compared to more complex architectures such as ViT [136], U-Net 2D is relatively simple, but its effectiveness is largely driven by the quality and diversity of the training dataset.

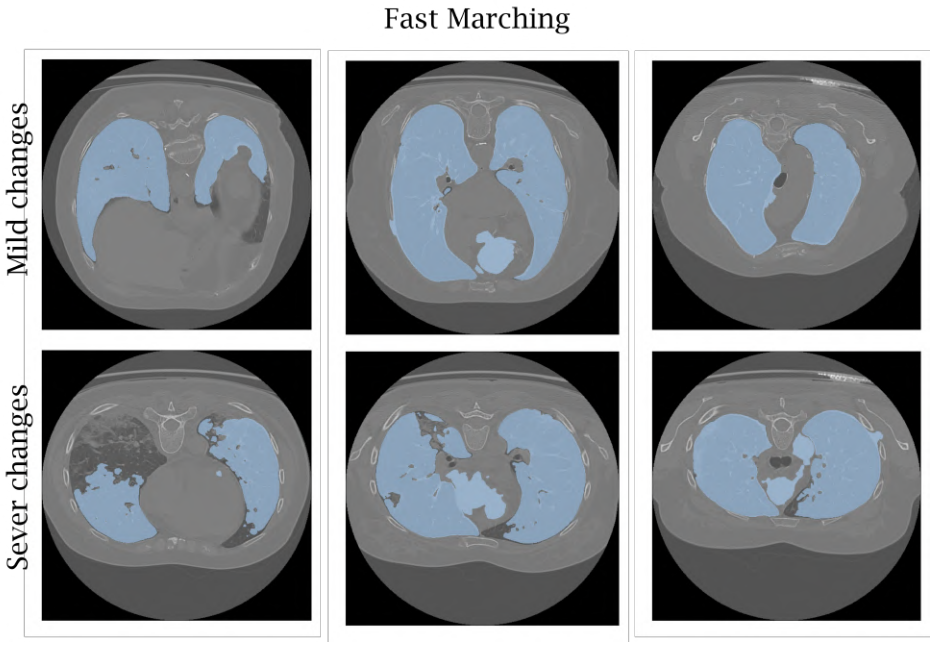

Figure 5.4: Example slices from patients with mild and severe abnormal parenchymal changes with overlayed results of the lung segmentation using the Fast Marching algorithm.

5.4 Discussion

Tests conducted using classical image processing methods have shown that this is a complex problem. Although voxel intensity levels exhibit regular structure and homogeneity, changes in the parenchyma disrupt the tissue's natural characteristics. Classical algorithms are sensitive to such disturbances and require adaptation. No classical image processing algorithm was found to perform well in the presence of abnormal structures in the lung parenchyma.

This dissertation focuses on exploring the use of classical methods. While deep learning is currently the most popular approach, classical methods are still useful, especially when there is not enough diverse, labelled data. This often happens in tasks like segmenting lesions or muscle groups, where manual labelling is difficult. In contrast, the lungs are easier to identify in CT scans because they are separated from surrounding tissue. Additionally, the COVID-19 pandemic led to increased research on lung diseases, resulting in many new tools and labelled datasets. Since lung segmentation is already well-studied and serves mainly as a preliminary step for analysing lesions, this work uses an existing lung segmentation solution.

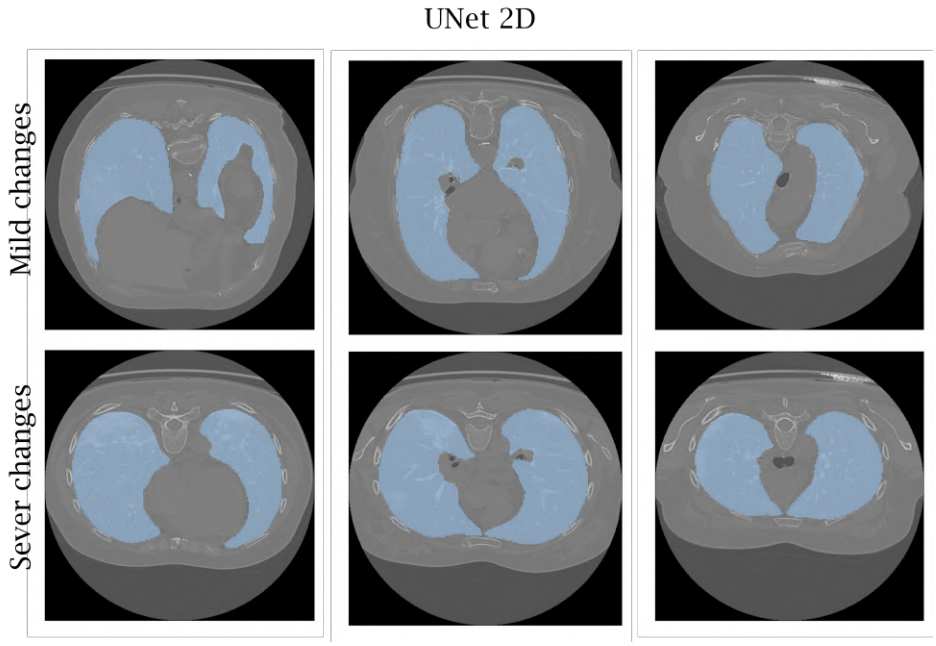

Figure 5.5: Example slices from patients with mild and severe abnormal parenchymal changes with overlayed results of the lung segmentation using U-Net 2D.

As part of the neural network tests, the effectiveness of the method proposed by Hofmanninger et al. [135] was evaluated. This method was selected because it met a critical condition: it had been trained on a diverse dataset and tested on a variety of diseases. Other approaches were not considered, as none of them met the required criteria. Some methods either did not analyse the lungs affected by lesions [116, 118, 120, 121, 122, 123, 125, 128, 130] or had issues with algorithm availability [127, 129]. Additionally, the method by Hofmanninger et al. [135] proved to be effective. Since the analysis of differences between lung segmentation methods was not the primary focus of the dissertation, this method was incorporated into the final processing pipeline.

Chapter 6

Airways

This chapter describes the method used for segmenting airways from the lungs. The primary objective is to remove the airways before proceeding to the next stage of analysis. A secondary objective is to analyse the airway regions.

The airway segmentation method utilises three key features of the airways. First, their tubular structure is considered. Second, the characteristic voxel intensities of their filling are taken into account. Third, the fact that the airways are enclosed by solid tissue walls is used as a distinguishing feature. Based on these properties, the method relies on the dual-gradient map fast marching algorithm, which is bounded by the estimated airway walls.

6.1 Motivation

Chronic Obstructive Pulmonary Disease (COPD) is characterised by two particular changes in the chest image of the lungs. The first is pulmonary emphysema, which is a reduced attenuation of the lung parenchyma due to the destruction of the lung parenchyma. The second is small airway inflammation (bronchiolitis), which causes narrowing or loss of the airway lumen (Figure 6.1).

It was originally believed that small airway disease only manifests itself in advanced stages of COPD. However, the study by Niewoehner et al. [138] was the first to show that it also occurs in young smokers. They carried out an analysis of the lungs of deceased smokers of a similar age (under 40) eliminating those with visible emphysematous changes from the study. The study indicated a link between smoking and

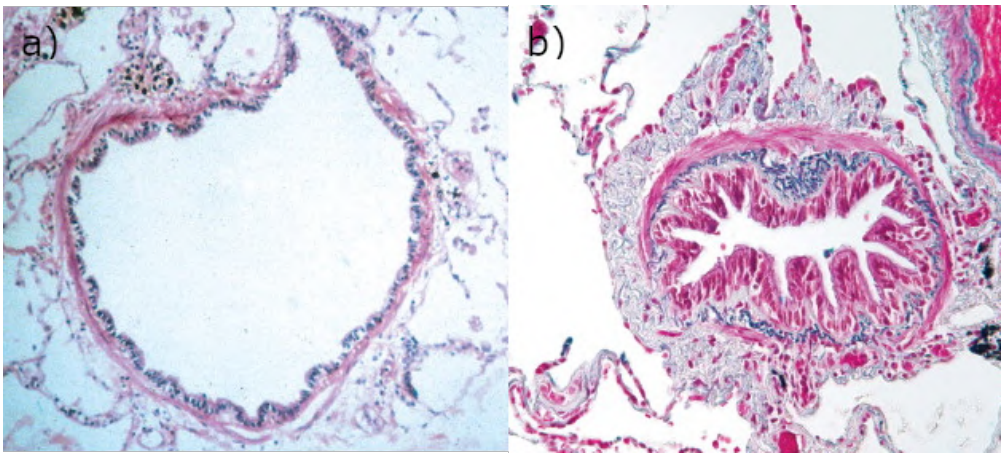

Figure 6.1: a) Healthy small airways; b) Airways blocked by connective tissue and restricting its lumen, resulting from inflammation [137].

pathological changes in the peripheral airways, which the authors identified as potential indications of more severe pathological changes. Since then, more studies have appeared analysing this problem. In 1978, Cosio et al. [139] created a scoring system to determine the extent of pathological changes in small airways based on lung biopsy findings. They considered the lesion initially indicative of small airway disease to be a progressive inflammatory reaction leading to fibrosis with deposition of connective tissue in the airway walls. Further independent studies have emphasised the relevance and impact of small airway lesions on the development and progression of COPD [140, 141].

Even in the presence of emphysema, airway inflammation appears to have a significant impact on the functional health deterioration of patients with COPD. It is further emphasised by the work of Wright et al. [142] who examined non-smokers, smokers and ex-smokers. The respiratory bronchioles of smokers appeared to be significantly more inflated and had significantly decreased goblet cell pigment compared to ex-smokers. But what is even more important in the scope of the thesis is that the wall thickness of membranous and respiratory bronchioles was significantly larger in the smokers' group than in the ex-smokers' group. His study found that smoking increases bronchial wall thickness, regardless of airway size or the amount of emphysema. Other studies confirmed these findings by showing a correlation between airflow limitation and the average airway diameter [143, 144].

Inflammation of the airways and emphysema have a complex relationship. Studies have proven that the presence of emphysematous changes does not always directly

mean that the airways are inflamed. Small airway disease seems to affect people with centrilobular emphysematous (CLE) changes when, in people with predominant panlobular emphysematous (PLE) changes, airway inflammation is less frequently noted [145, 146]. Research indicates that PLE and CLE are different from the start and indicate different disease progression paths. Patients with CLE show more muscularization and airway wall thickening than patients with PLE. It has been observed, in patients with CLE, that the upper small airways are significantly more occupied than the lower airways [147] (Figure 6.2) and, importantly, that changes in the small airways precede the appearance of emphysema [139].

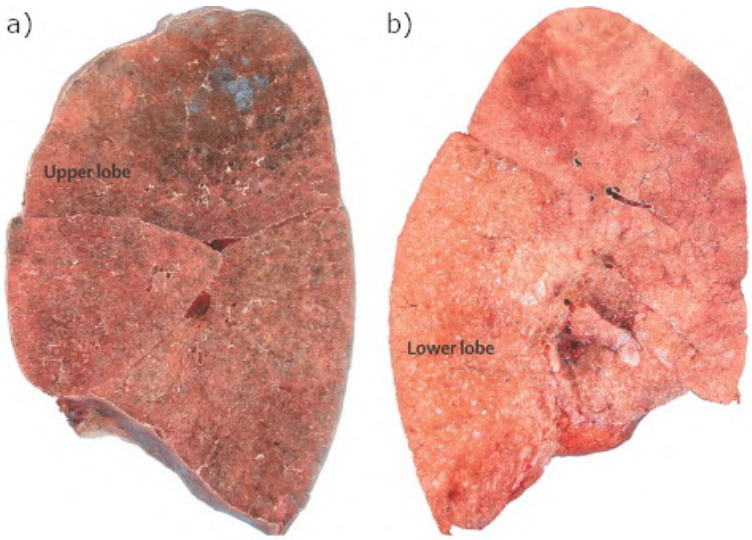

Figure 6.2: a) Photograph of a mid-sagittal slice of a lung removed from a patient who received a lung transplant for COPD from the work of Hogg et. al [137]. CLE-related changes resulting in highly inflamed upper lungs; b) Similar specimen from a patient who received a lung transplant also from the work of Hogg et. al [137]. Less severe PLE but the lower lungs are highly involved.

These studies demonstrate the importance of analysing the bronchial condition in COPD. Using it, physicians can assess the degree of damage and plan treatment, define the type of disease, and even potentially prevent further damage to the bronchioles. From the point of view of automated image analysis, the bronchi are also a potential confounder. If the aim is to segment emphysematous lesions, the bronchial tree makes this task much more difficult by having similar voxel intensity values to lesions. Therefore, bronchial segmentation, in addition to the direct benefit of increased diagnostic accuracy, potentially facilitates further steps in the automatic analysis of the condition.

6.2 State of the art

The airways or bronchi have distinctive features commonly exploited by various algorithms. It is a tree-shaped structure that extends from the mediastinum and branching through the lung parenchyma up to 23 times. On a standard-dose CT image, trained physicians can see up to 7 branchings. Each branching results in a smaller branch where each branch is a narrowing tube-like structure filled with low-level grey-intensity voxels surrounded by walls with relatively high-level grey-intensity voxels. Many methods emerged discussing the problem of airway segmentation and proposing solutions to this issue. Usually, they use a combination of several airways' characteristics, where one characteristic serves as the base for the main novelty of the method. In response to the tree-like structure of airways, researchers use growing methods starting from the base to the terminal branches. They noticed that the tubularity of the tree can be mathematically described by the Hessian matrix. The characteristic grey level intensities can be exploited by thresholding methods. The narrowing of the airway structure can be detected by bottom-up iterative analysis of the structure. Based on those observations, airway segmentation methods can be divided into general categories: Hessian-based, growing, morphological, and neural network-based methods.

Hessian-based methods are one of the most commonly seen in older approaches. They exploit the tubular structure of the bronchiole by analysing Hessian eigenvalues convolved with the Gaussian filter of predefined standard deviation σ (for in-depth explanation refer to **??**). One of the first such approaches was proposed by Sato et al. and called the Sato filter [148] followed by the Frangi filter [149], Meijering filter [150], Jerman filter [151] and Zhang filter [152]. While neither of them specifically talked about airway segmentation from CT thorax scans, part of them proved their ability to differentiate those structures from the lung parenchyma as an additional ability. They also laid the foundation for other great works related to this topic [153, 154, 155].

The growing-based methods are also popular due to the commonly seen problem in the airway automatic segmentation field, the so-called leakages. The bronchus extends inside the lung parenchyma; its goal is to distribute air to the alveoli located inside the lung. Leakages in the segmentations occur when the bronchi blend into the lung parenchyma and become indistinguishable; some methods like thresholding or morphological methods may, as a result, contain the voxels of the lungs, which are adjacent to the bronchi and not divided by the airway wall. Growing methods usually consist of guided, step-by-step growth of the airway mask area while trying to avoid leakages.

Such methods may use a region-growing algorithm for evolution [97, 156, 157, 158, 159, 160] while some of them are semiautomatic, as in the Bartz et al. study [159] which requires defining a manual seed point in the trachea while using 3D growing with template matching. The region-growing method is typically combined with other novel approaches or algorithms to address the problem of airway extraction. Lo et al. [160] introduced a method in which the primary innovation lies in utilising vessel orientation for airway identification, with region-growing serving as a substep of the process.

In addition to region-growing, the fast-marching algorithm is commonly applied to this problem. This algorithm is based on the propagation of a wavefront from a given point or multiple points on the velocity map. It has been demonstrated to be effective in analysing subsequent fronts and filtering leakages [161, 162, 163]. The regular shape of the propagation front provides several advantages, such as enabling the extraction of a minimum path from the root to terminal points, known as the centerline [163, 164]. Additionally, this structured propagation allows for a stepwise analysis of the growing process [165]. The method can also serve as a final step in the analysis to complete the airway tree segmentation process [161, 162, 166].

Neural network-based solutions are widely used due to their high accuracy and ability to function without manual adjustments. However, several challenges exist. A large dataset with precise masks is required, and the dataset must encompass diverse CT image features. There are a few publicly available datasets dedicated to the task of airway segmentation. The most popular of these is the EXACT'09 dataset [167], consisting of 40 CT series containing CT images of the lungs, of different patients taken by different scanners and possessing respective bronchial masks. For training and testing, the dataset was divided into two equal parts. However, in the literature, a common approach is to allocate 70% for training and 30% for testing and validation [168]. Additionally, to enhance the dataset, internally labelled data were used with the assistance of other segmentation tools and under specialist supervision. However, these datasets were not made publicly available [169, 170]. Among the available neural networks, convolutional neural networks (CNNs) with 3D kernels are the most commonly used [171, 172, 173, 168]. An alternative approach was proposed by Yun et al. [169], in which three cross-sections are analysed collectively for voxel classification. Another notable solution is the method introduced by Charbonnier et al. [168], which is not directly used for segmentation but rather for detecting leaks in segmentations generated by proliferative segmentation methods. Other methods found in the literature are

largely based on the UNet and VNet architectures, which have been repeatedly proven to perform well in image segmentation tasks [115]. Garcia-Uceda et al. have proposed several solutions based on the U-Net architecture. One approach utilises large data patches and various augmentation techniques [174]. Another method combines U-Net with graph neural networks (GNN) [175]. Additionally, a patch-based solution incorporating a 3D U-Net was introduced, leveraging a large and diverse dataset [173]. The graph-based structure of the airways drives methods of Jin et al. [176] and Meng et al. [177], who used the U-Net architecture but applied convolutions along the extracted centerlines. Qin et al. [178] and Zhao et al. [179] also exploit the fact that airways form a fully connected structure, using voxel connectivity analysis or tracking the airway length through the application of a 3D U-Net architecture. Later, Qin et al. [180] proposed an approach for airway segmentation that incorporates feature recalibration and an attention module, using the U-Net architecture as a base. Nadeem et al. introduced an iterative "freeze-and-grow" method using U-Net, where the airway segmentation is repeatedly passed through the U-Net network, gradually growing the airways up to the terminal bronchioles.

Despite so many approaches, only a few have been shared as a ready-to-run product. Making it hard to reproduce and test. Although neural network approaches appear to be the most prominent, they usually use internal datasets for training. The lack of data makes it impossible to achieve the same results as the authors. Following that, a novel, easy-to-implement method for airway extraction with an emphasis on the correctness of the resulting segmentation was proposed. It is based on the properties of the Hessian matrix eigenvalues, connectivity analysis and iterative growth of the segmentation.

6.3 Methods

6.3.1 Mediastinum segmentation

Mediastinal segmentation is needed to initiate and perform the bronchial modelling procedure. For this purpose, a convex hull of a lung mask was calculated. To separate the lung mask from the mediastinum, the lung mask was subtracted from the resultant convex hull mask. A morphological opening operation was performed to eliminate any residual noise in the image. From the resulting mask, the largest object was selected using the connected components method, thus obtaining the mediastinal mask.

6.3.2 Trachea segmentation

The trachea connects the esophagus and the bronchial tree, diffusing into the lung parenchyma. The tracheal mask is required to start the bronchial modelling procedure and outline the trend line controlling the modelling process. Based on the results of the Vegas-Sánchez-Ferrero et al. [181] study showing the theoretical median values of Haunsfield units (HU) in the trachea, the cut-off values were set at -1024 HU and -920 HU. The threshold resulted in a set of non-connected objects (masks) in 3D space. The trachea is one of the largest objects in the set. Still, since there are cases in which the diaphragm turns out to be larger, the object to be searched must be as close as possible to the centre of the 3D matrix, which defines the space in which the objects are located. To detect an object corresponding to the trachea within the set, an object was identified that maximised two conditions: its size and its position relative to the centre. Example trachea segmentation is shown in Figure 6.3.

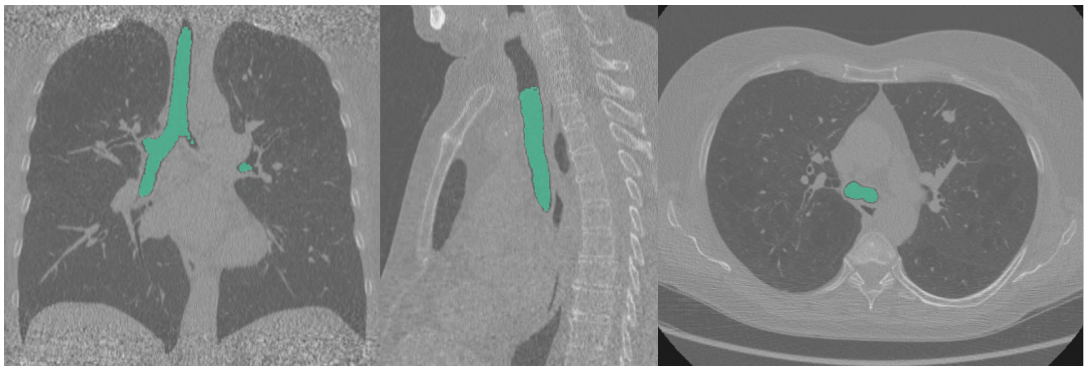

Figure 6.3: Trachea mask resulting from described methodology.

6.3.3 Rough High and Low attenuation elements segmentation

The rough mask of high and low attenuation elements was created using the Gaussian Mixture model method. The segmented lung area served as an input signal from which the distributions were derived. The number of components for this part was fixed to 3. The first component was supposed to be reserved for air, but when the patient suffers from severe emphysema, this component covers the emphysematous changes. The second component was a supporting component, reserved also for the air in most cases, but could also contain mild ground glass opacities. The third component was reserved for high-attenuation objects like solids, walls, fluids, consolidations, and vessels. The intersections of the Gaussian distributions were marked as thresholds which

were applied to the image. This resulted in 3 thresholds and 4 segmentations. First and second segmentations were joined, creating a low attenuation rough segmentation (LARS). The third and fourth components were also joined, creating a high attenuation rough segmentation (HARS).

6.3.4 Speed map creation

The final speed map image is a combination of two other maps, both made based on the low attenuation rough segmentation (LARS). The first map was created by calculating the gradient magnitude from the LARS Eq. 6.1 and passing it through the bounded inverse function Eq. 6.2. This way preserving the LARS structure and penalizing the narrowing.

$$\|\nabla I(x,y,z)\| = \sqrt{\left(\frac{\partial I}{\partial x}\right)^2 + \left(\frac{\partial I}{\partial y}\right)^2 + \left(\frac{\partial I}{\partial z}\right)^2} \tag{6.1}$$

$$I^{'} = \frac{1}{1 + \|\nabla I(x,y,z)\|} \tag{6.2}$$

The second map was created by passing the air mask through a Sato filter. Sato vesselness filter is a Hessian-based method designed to highlight bright tubular structures [148]. Hessian matrix of the 3D image at point $p = (x, y, z)$ is defined in Eq. 6.3.

$$H(p) = \nabla^2 I(p) = \begin{bmatrix} I_{xx}(p) & I_{xy}(p) & I_{xz}(p) \\ I_{yx}(p) & I_{yy}(p) & I_{yz}(p) \\ I_{zx}(p) & I_{zy}(p) & I_{zz}(p) \end{bmatrix} = \begin{bmatrix} \frac{\partial^2 I(p)}{\partial x^2} & \frac{\partial^2 I(p)}{\partial xy} & \frac{\partial^2 I(p)}{\partial xz} \\ \frac{\partial^2 I(p)}{\partial yx} & \frac{\partial^2 I(p)}{\partial y^2} & \frac{\partial^2 I(p)}{\partial yz} \\ \frac{\partial^2 I(p)}{\partial xz} & \frac{\partial^2 I(p)}{\partial zy} & \frac{\partial^2 I(p)}{\partial zz} \end{bmatrix} \tag{6.3}$$

It is important to note that to calculate the Hessian matrix for a 3D image, it must be continuous and twice-differentiable. However, the images are digital, non-continuous, and non-differentiable. Therefore, before calculating the Hessian matrix, the image is convolved by the Gaussian filter Eq. 6.4.

$$I^g(p) = G(p;\sigma) * I(p) \tag{6.4}$$

Where $G(x;\sigma)$ is a Gaussian kernel of scale σ and $*$ is a convolution operation. This creates a relation between vessel size and the scale of the Gaussian filter; only vessels as thick as the scale will be considered by the filter. The multi-scale space representation of the image was created; using its properties, the equation can be rewritten [182]. As an example, an equation in the new form is shown for $I_{xx}(p;\sigma)$ Eq. 6.5.

$$I_{xx}(p;\sigma) = \frac{\partial^2}{\partial x^2}\{G(p;\sigma) * I(p)\} = \left\{\frac{\partial^2}{\partial x^2}G(p;\sigma)\right\} * I(p) \tag{6.5}$$

Now, the Hessian matrix equation can also be rewritten.

$$H(p;\sigma) = \nabla^2 I(p;\sigma) = \begin{bmatrix} I_{xx}(p;\sigma) & I_{xy}(p;\sigma) & I_{xz}(p;\sigma) \\ I_{yx}(p;\sigma) & I_{yy}(p;\sigma) & I_{yz}(p;\sigma) \\ I_{zx}(p;\sigma) & I_{zy}(p;\sigma) & I_{zz}(p;\sigma) \end{bmatrix} \tag{6.6}$$

Let eigenvectors of the Hessian matrix 6.6 be $e_1(p;\sigma)$, $e_2(p;\sigma)$ and $e_3(p;\sigma)$ with eigenvalues $\lambda_1(p;\sigma)$, $\lambda_2(p;\sigma)$ and $\lambda_3(p;\sigma)$. Calculating eigenvalues for every voxel in an image results in collections λ_1, λ_2 and λ_3 ($\lambda_1 < \lambda_2 < \lambda_3$). If the vessels in the image are represented by the light tubular structures present on the dark background, they express properties 6.7.

$$\lambda_1 \approx 0 \quad \text{and} \quad \lambda_2 \approx \lambda_3 \ll 0 \tag{6.7}$$

Sato vesselness filter builds on these properties, starting by sorting eigenvalues λ_1 so $\lambda_1 \geqslant \lambda_2 \geqslant \lambda_3$. Then the eigenvector e_1 is associated with the main direction of the vessel and the eigenvectors e_2 and e_3 are associated with a tube's cross-section. Following that, the eigenvalues λ_2 and λ_3 represent the size of a cross-section and λ_1 length of a tube. Sato proposed a formula based on the sign of λ_1 with control parameters α_1 and α_2 Eq. **??**.

$$S = \begin{cases} \lambda_c \exp(-\frac{\lambda_1^2}{2(\alpha_1 \lambda_c)^2}) & \lambda_1 \leq 0, \lambda_c \neq 0 \\ \lambda_c \exp(-\frac{\lambda_1^2}{2(\alpha_2 \lambda_c)^2}) & \lambda_1 \geq 0, \lambda_c \neq 0 \\ 0 & \lambda_c = 0 \end{cases}$$

Where $\lambda_c = \min(-\lambda_2, -\lambda_3)$.

The created Sato useless image was normalised, values less than 0.05 were clipped, and the image was multiplied by the air mask. The image created contains high values in the tube-like voxel complex and low values elsewhere. For the Sato filter, the following values of σ=[2, 3, 5] were taken as Gaussian filter scales. The speed image resulting from a combination of LARS's gradient magnitude and Sato filtering is presented in Figure 6.4.

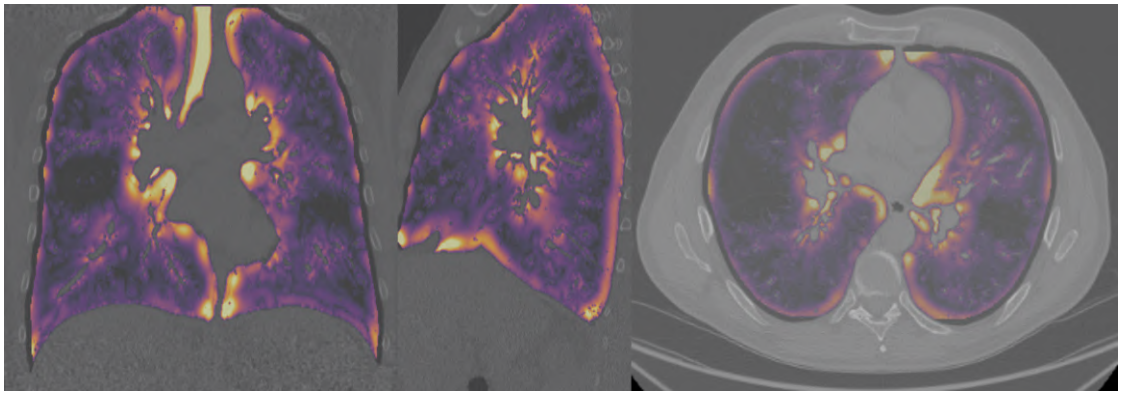

Figure 6.4: Final speed map image resulting from the multiplication of speed components.

6.3.5 Seed points generation

Thresholding LARS determines the seed points for the fast marching algorithm with the mean value of the voxels in the trachea. Voxels located in the airways have significantly lower HU values than voxels located in the lungs, even though their intensities indicate the presence of air according to the Hounsfield scale. This is because there are alveoli in the lungs. The walls of the alveoli have a higher density than the air, which increases the attenuation coefficient and increases the voxel HU values. The average of the air present in the trachea was calculated to obtain the initial values for

the fast-marching algorithm. From this value, the original image was multiplied by the air mask and was thresholded below the calculated mean, yielding a set of initial values for the fast marching algorithm.

6.3.6 Fast Marching segmentation

The created speed image and seed points image served as an input to the Fast Marching algorithm. The output time crossing map was limited to a maximum crossing time value of 10 and is binarised for further analysis. To find the mask's element representing the airway approximation, the mask was labelled using the connected components method. Each component's mask was then compared to the trachea segmentation using the Jaccard index. The most similar component mask was then selected as the airways approximation.

6.3.7 Airways wall guided segmentation

The segmentation from the previous step (Fast Marching segmentation) may include over-segmentations due to the marching front extending beyond the lung surface. To remove these segments, the algorithm assumed that airways were surrounded by highly attenuated walls. The airway walls were found by applying a dilation operation with a sphere-shaped structuring element of radius 3. Airway walls were obtained when the dilation result was multiplied by the processed mask created from the third GMM component. After that, to the resulting wall mask, the morphological closing operation was applied. Multiplying the resulting mask with the original airways mask returns the final airways mask. Both airways and their walls were marked on the output segmentation mask. The example airways model before and after wall guided segmentation is shown in Figure 6.5.

6.3.8 Over and Under segmentation detection

The proposed method is unsupervised, making it difficult to evaluate the quality of the results. Therefore, an unsupervised method for faulty segmentation detection was proposed based on the Hubert outliers [183] detection method. The resulting segmentations of the bronchial trees were marked with values from 1 to 9. Mark 5 indicates proper segmentation, marks 1 to 4 indicate under-segmentation, and marks

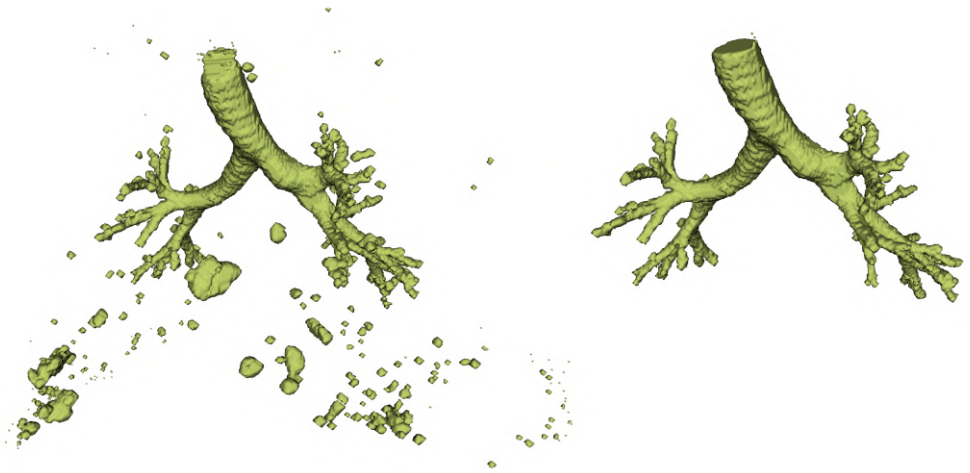

Figure 6.5: First subplot, airways mask after the Fast Marching segmentation, second subplot, final airways mask after wall-guided segmentation.

6 to 9 indicate over-segmentation. Segmentations marked 1-3 and 7-9 are considered incorrect. Segments marked 4 and 6, despite the absence of some branches or minor leakages into the lung parenchyma, are considered sufficient.

From each resulting segmentation, a set of features was calculated. This set includes basic properties of the segmented airways, such as the number of voxels and volume in millilitres, as well as characteristics of the airway's final branches. The final branches were segmented using the following operations. A convex hull was created from the airway segmentation. The convex hull was then eroded using a cube structuring element of size 10. The result of the erosion was subtracted from the convex hull and multiplied by the airways, resulting in an image containing the end-airway branches. Each independent branch was labelled, and the following features were calculated for each branch: area, major axis length, equivalent diameter area, Euler's number, extent, and the area filled by the convex hull. The branch features were aggregated using the maximum, minimum, mean, and standard deviation functions so that a single value per feature represented each segmentation. Additionally, the number of labelled components was added to the feature set.

To find the feature that best represents the quality of the segregation, the Spearman correlation between the calculated feature and the created marks was counted. The feature with the highest correlation coefficient was used to calculate box and whiskers using the Hubert method [183]. The data points outside of the whiskers were considered outliers, either over or under segmentations.

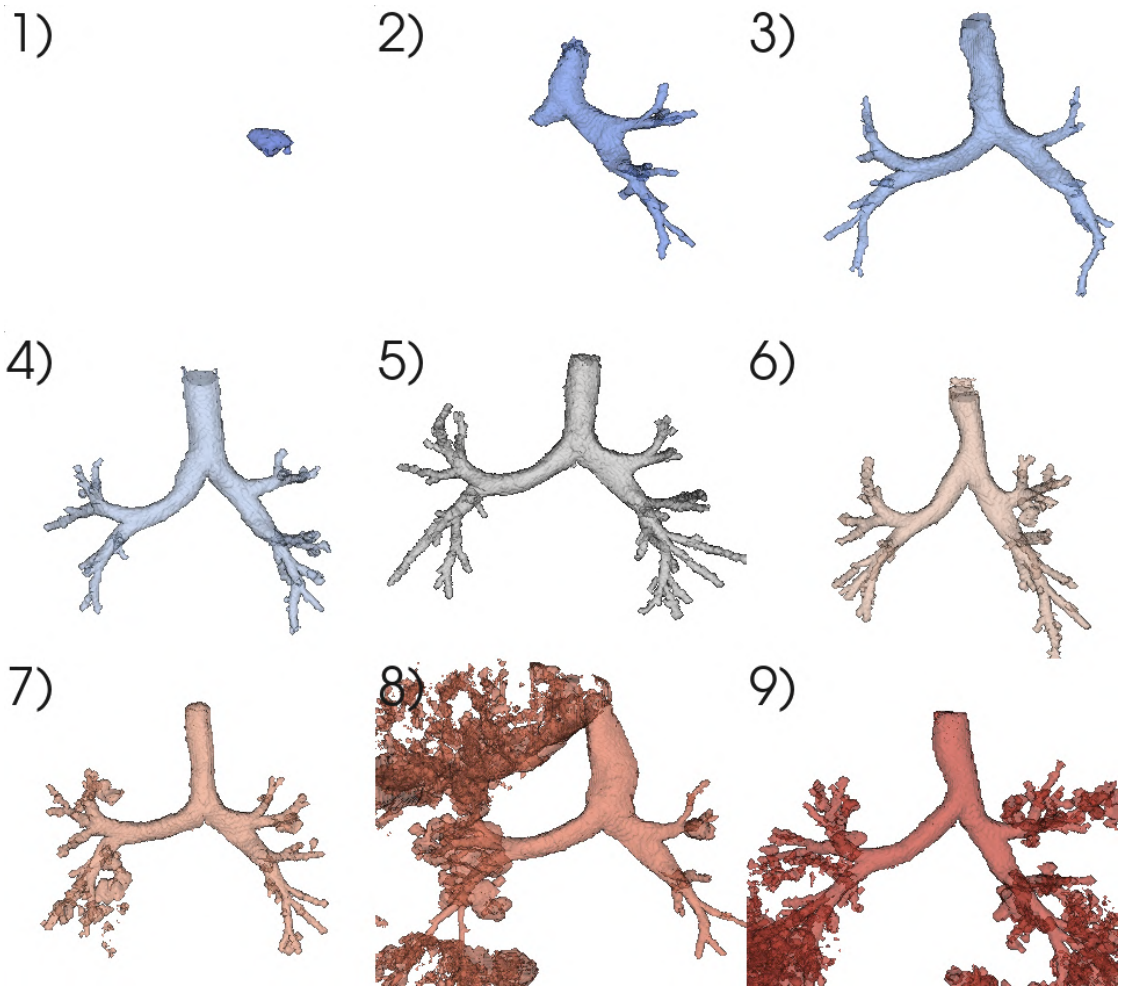

Figure 6.6: Example airways segmentations from each mark, 1-4 under-segmentation, 5 proper segmentation and 6-9 over-segmentation.

6.4 Results

The resulting segmentations were marked with values from 1 to 9, where 5 indicated proper segmentation, 4 and 6 sufficient segmentation, and 1-3 and 7-9 faulty segmentation. Example segmentations of each mark are shown in Figure 6.6.

Most of the airway segmentations are of proper quality, that is, they belong to group 5, comprising 614 images, which represents 55.22% of the total set. The suitable quality segmentations, labelled 4 and 6, consist of 163 (14.66%) and 201 (18.26%) segmentations, respectively. Fourteen 14 (0.01%) segmentations were included in the group, consisting of segmentations with under-segmentations, denoted by values 1-3. The group of images with visible over-segmentations, denoted by 7-9, included 118

(11.85%) segmentations. The resulting distribution of airway segmentation quality values is presented in Figure 6.7.

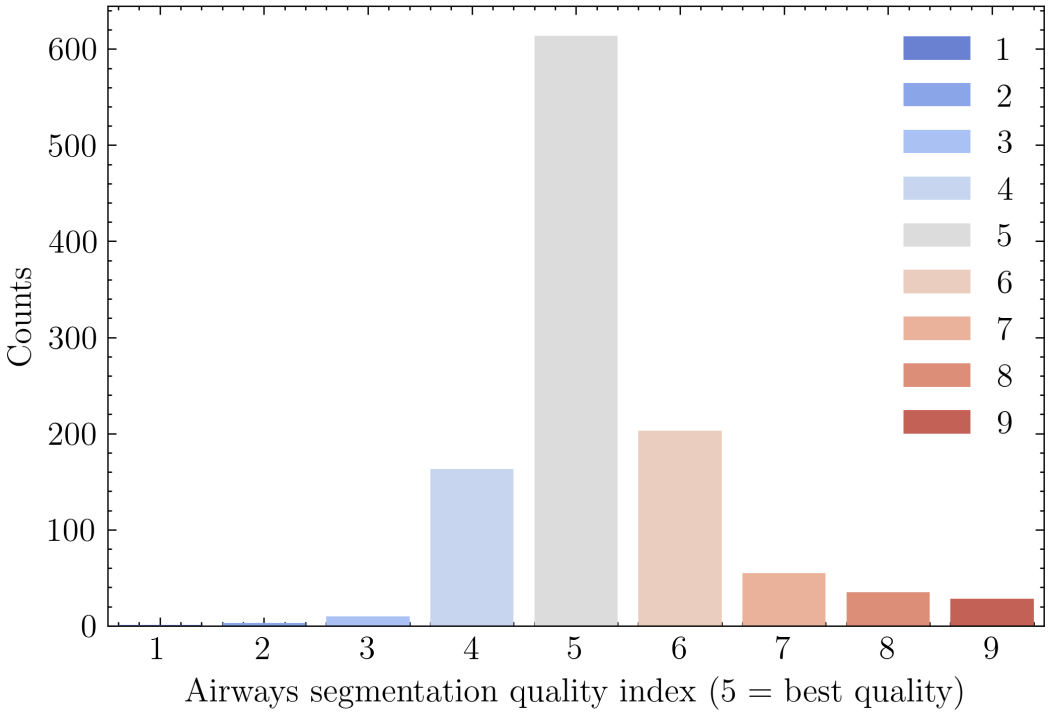

Figure 6.7: Distribution of airway segmentations' marks, the majority of segmentations are of good quality (5) or sufficient quality (4, 6).

The segmentation features were calculated, including volume features (number of voxels, volume in mm) and terminal branch features (area, major axis length, equivalent diameter area, Euler's number, and extent). Spearman's rank correlation was calculated between features and marks. The resulting correlation coefficients are shown in Figure 6.8.

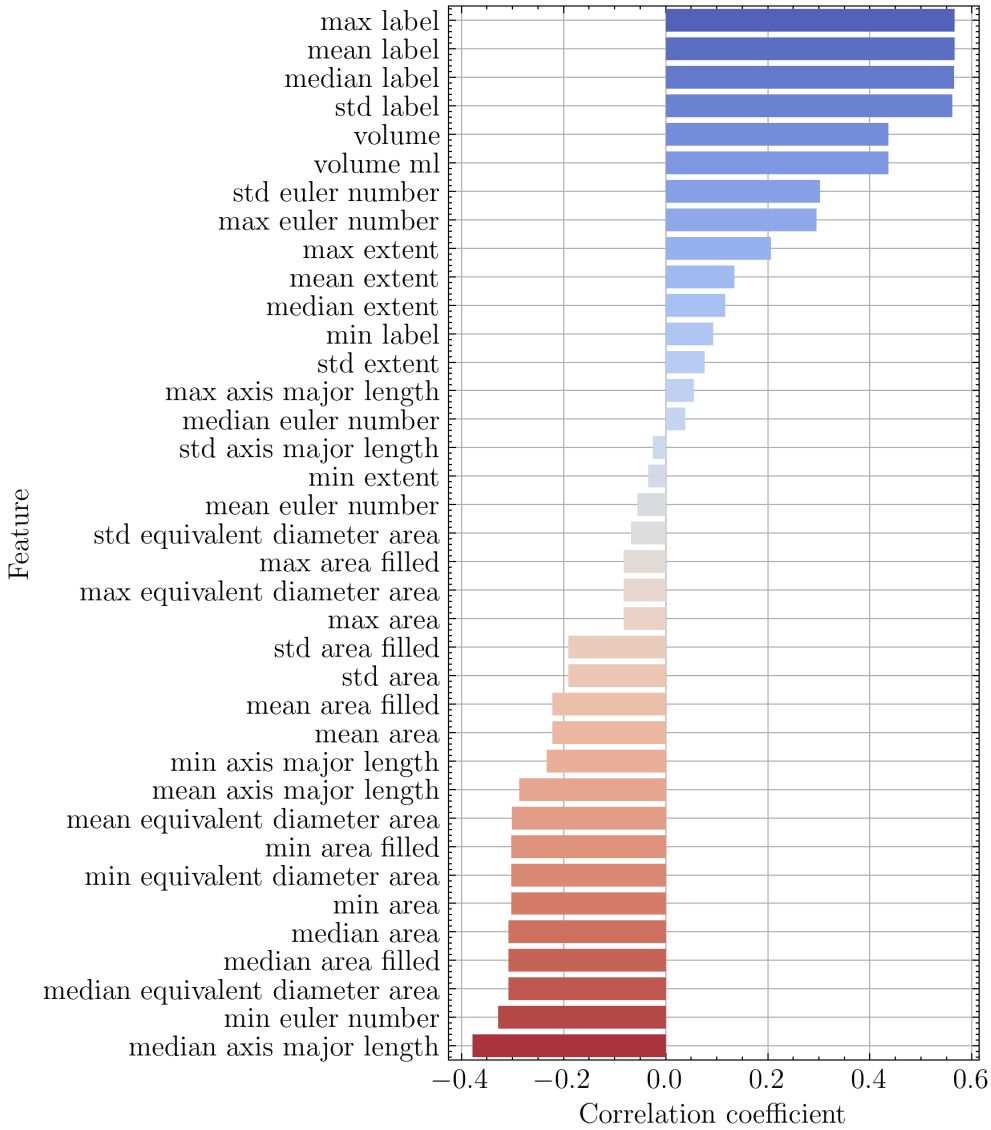

Figure 6.8: Barplot showing correlation coefficients of the features tested against the grade of the airways segmentation.

The highest positive correlation coefficients have features derived from the number of objects, reflecting the number of final branches of the segmentation. The second-highest correlation score has a feature related to the volume of the segmented airways mask. Close to the value of 0.3 are features related to the Euler number, that means, the number of objects minus tunnels and holes in the mask. The median length of the main object vectors and the minimum value of the Euler number of objects have the highest negative correlation coefficients, see Figure 6.8.

To detect faulty segmentation, the Hubert outlier detection method [183] was used.

The over and under segmentations (faulty segmentations) were marked as 1-3 or 7-9, respectively, whereas those marked as 4, 5 and 6 were considered proper segmentations. Based on the feature with the highest correlation coefficient, a boxplot was created whose whiskers were determined using the Hubert method presented in Figure 6.9. Segmentations outside the whiskers are considered abnormal, whereas those between the whiskers are considered normal. The summary of the results was included in Table 6.1.

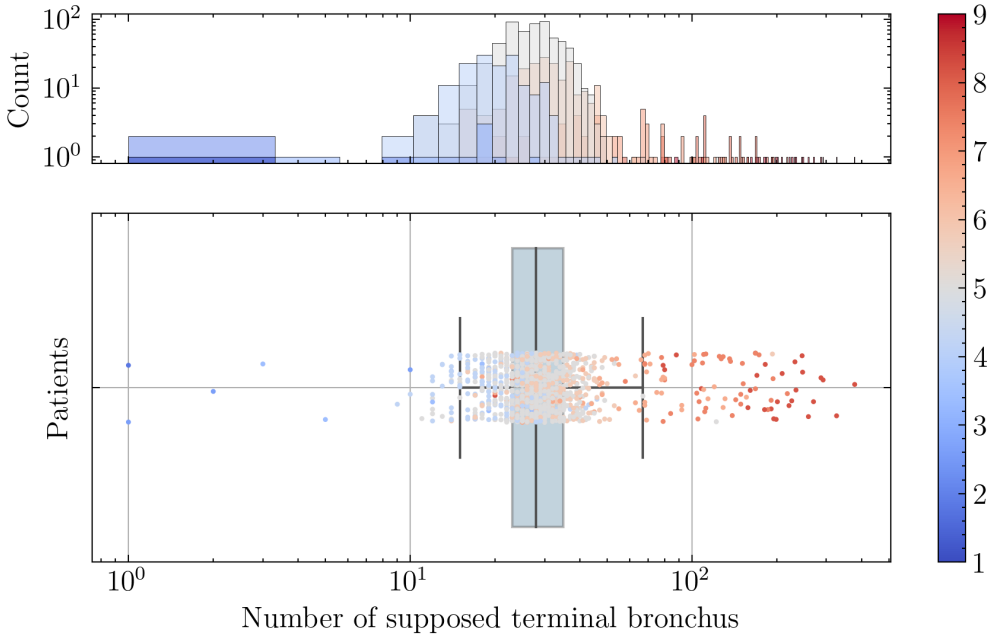

Figure 6.9: Boxplot, where the whiskers were calculated using Hubert et al. [183], and used for filtration of the faulty (outlying) airways segmentations.

Grade	**1**	**2**	**3**	**4**	**5**	**6**	**7**	**8**	**9**
Counts	1	3	10	163	614	203	55	35	28
Accuracy [%]	100	66.7	20	99.4	99.5	50.9	97.1	96.4	96.4

Table 6.1: Outlaying segmentations detection accuracy is shown per grade in the table. Grades 1-3 and 7-9 represent faulty and 4-6 proper segmentations. The system assigns 0 to faulty and 1 to proper segmentations.

6.5 Disscussion

A three-component Gaussian Mixture Model (GMM) method was developed for initial low and high attenuation patterns distinction. The decision was made mainly based on the presence of two dominant structures in the lung parenchyma: air and fluids like blood. The third component was reserved for abnormal changes. However, alternative methods for voxel grouping could be considered. For instance, when working on airway detection with COVID-19-related inflammation, more components could be considered due to the presence of ground glass opacities. These types of inflammation, characterised by varying tissue densities, could confound the initial low and high attenuation tissue distinction process.

There are cases of airway segmentation where the terminal branches of the bronchial tree are not accurately delineated. This is because the farther into the pulmonary parenchyma the branches of the bronchial tree are drawn, the higher their HU values become, more and more similar to the HU values of the pulmonary parenchyma. The boundary between them and the parenchyma becomes blurred, and leaks, or direct connections to the branches to the alveoli, also become more frequent. In its current form, the method works well enough for the task set before it: to process CT images before the next processing steps. The next steps are automatic thresholding and quantification of emphysematous changes. So the method's main goal is not to remove fragments of the bronchial tree with HU values close to the HU values of the lung parenchyma.

The method employed the Sato filter [148] to generate a velocity map, selected for its resistance to noise and its ability to control the size of detected structures by adjusting the sigma parameter. The Frangi [149] and Meijering [150] filters were also tested during method development. The Frangi filter struggled to filter out structures at the high noise levels typical of LDCT scans and performed poorly in detecting small structures. The Meijering filter was overly sensitive to narrow, smaller tree fragments but less effective with thicker structures. To determine the most effective filter, further investigation into their performance and the influence of their parameters on the results would be required. It is possible that one of these filters could address the issue of accurately segmenting terminal bronchial segments.

Regarding the correlation of features with groups and their ability to distinguish over-segmentation and under-segmentation groups using the Hubert method [183], it

was initially expected that the most strongly correlated features would be the volume of the entire bronchial tree, the Euler number of the borders, and the length of the main axis of the borders. The volume feature was indeed one of the most correlated features, providing good filtering of edge case groups from group 5. However, the volume feature did not perform as well with features closer to group 5. The Euler number of the edge also considers the holes that often occur with poor segmentations, but these were less frequent in groups closer to 5, possibly explaining the lower correlation. The length of the major axis of the edges could have yielded greater values for Tukey filtering if the end bronchioles (branches) had been segmented more accurately. The rationale behind edge analysis is that the end bronchioles should be tube-shaped. However, the methodology employed in this study does not ensure accurate segmentation of these structures. Achieving such accuracy would have required a branch-by-branch analysis of the tree until no further connections were found in the analysed branch. This approach was not chosen, as over-segmentation cases often result in closed loops of branches, which could lead to erroneous identification of terminal bronchioles. Additionally, such an analysis would have been highly time-consuming. Therefore, a simplified version of the method was adopted.

In COPD, the terminal bronchial wall has significant diagnostic information. The method presented here returns a mask of the wall in addition to the airways themselves. This allows diagnosticians to accurately analyse the thickness and assess the progression of the disease. This can be particularly useful for treatment planning in patients with impaired respiratory capacity but no visible emphysematous changes.

Chapter 7

Low attenuation patterns

This chapter discusses and describes low-attenuation pattern segmentation methods based on computed tomography images of the thorax. The main goal of this segmentation pipeline is to find and mark voxels of specific areas of lung parenchyma that are afflicted with emphysematous changes. The sub-goal is splitting the afflicted regions into sub-regions based on their connectivity and position.

Methods presented in this chapter are based on adaptive thresholding and the key assumption that healthy structures visible on lung CT scans, similar in value to the areas being searched for, are removed before the method starts. Analysis of the CT scans is performed per-slice, for which Gaussian mixture models are created at the intersections of which cut-off thresholds defining separate clusters are determined. As low-attenuation values characterise emphysematous lesions, the first cluster contains voxels that are considered to be emphysematous lesions. Within a single CT series, the lesions are further clustered based on their location and degree of connectivity.

7.1 Motivation

In the case of low attenuation patterns, as mentioned previously, in the scope of the study, the main emphasis was placed on emphysematous changes related to chronic obstructive lung disease. In clinical practice, the degree of lung destruction by pulmonary emphysema is measured by the pulmonary function test (PFT), which is primarily a spirometric test. The test result is compared with the expected lung function values. However, PFT is only effective in severe cases. Studies have shown that for a spiro-

metric test to yield an alarming result, a significant amount of lung tissue must be destroyed [184]. Practical medicine lacks a tool for the early detection of COPD with sufficient sensitivity. In addition, PFT does not provide precise information on the extent and location of the changes, which is crucial for further treatment as centrilobular and panlobular emphysema are fundamentally different [145, 146].

7.2 State of the art

Methods for identifying changes belonging to the group of low-attenuation patterns are mostly unsupervised. The first automatic systems for analysing emphysema were developed in the 1990s, using simple techniques like thresholding [185], region-growing algorithms [186], or dividing the lung into areas from top to bottom [187]. The statistics and characteristics of these areas were then calculated. These numerical values were used in classifiers to either identify disease areas or assess the severity of damage. Despite the simplicity of these methods, they achieved high accuracy in classification and were able to distinguish different stages of emphysema.

In the following years, researchers attempted to solve the problem of detecting or segmenting emphysematous lesions of the lung parenchyma. They proposed new systems or built on previous work, adding modules to increase the accuracy of the method. Older approaches tended to lack variety in the origin of the data due to the limited possibilities in the data transfer. As data transportation became an issue of the past, more and more studies have found that previous systems tend to be biased toward data of similar origin. This raised the need to universalise the approaches by making them resistant to the effects of differences in reconstruction kernels, CT scan layer thickness, and scanner manufacturer. An example is the work of Vegas-Sánchez-Ferrero et al.[188], which enables the use of the same cutoff thresholds to segment lesions on CT images from different centres by harmonising CT grey level values. A similar threshold-based solution was proposed by Hame et al. [189] they also noticed that fixed cutoff thresholds are not applicable if the studies come from different cohorts or centres. They proposed using a parametric intensity distribution model and a hidden Markov measure field model to detect areas of the lung affected by emphysematous changes. The paper Almeida et al. [190] is based on the idea of top-down division of the lung parenchyma. They have analysed many CT images by dividing them into top-down cubic regions based on these, creating a pattern to characterise emphysematous

lesions. The detection task reduces the problem of detecting anomalies by comparing the image being studied with a healthy reference model. An interesting variation of this solution is the method proposed by Mirela T. Cazzolato et al. [191], where the authors propose turning cubes into superpixels, which become supervoxels in the case of 3D images. By analysing each area and calculating metrics and features, they create a heat map that allows them to pinpoint areas affected by emphysematous lesions and other types of lesions. The patch-based approach was also used in the work of Ling Cheng et al. [192], where the lungs were divided into cube volumes of interest (VOI) and analysed by the graph convolution neural network. Patch-based approaches do not segment the lung parenchyma but classify the supposedly infected areas. Li et al. [193] took a similar approach, also divided the lungs into zones, and analysed them using a graph convolutional neural network.

Graph neural networks are not the only neural network type finding application in this problem; the work of Suzuki et al. [194] uses 2D UNet networks to segment emphysematous lesions from the lung parenchyma. The authors report the use of a rich dataset consisting of single-detector cross-sections of approximately 400 patients for training. Unfortunately, the dataset has not been shared for public use. The work of Peng et al. [195], due to the lack of fully labelled data, proposed a semi-supervised approach in which only part of the data was annotated and missing annotations were made online during the training process. The lack of labelling in the data is one of the main reasons why, despite the importance of the task, the topic of segmentation of emphysematous lesions is not often addressed. In the literature, the classification of lesions is more frequently found [196, 197, 198, 199].

A literature review reveals the biggest problem holding back the further development of emphysematous lesion segmentation methods, namely the lack of labelled data. This is a common problem; rarely are even the largest consortia able to tag enough diverse CT data to train a network that can be uniquely applied to this problem. Therefore, as part of this dissertation, the performance of an algorithm based on unsupervised learning was tested. As described in the "Anatomy" chapter and the "State-of-the-art" sub-section, emphysematous lesions are heterogeneous in position and shape but homogeneous in grey-level intensity. It is hypothesised that thresholding methods can be used to determine the intensity level of the lesions in the patient's lung parenchyma. This class of methods was effective in the 1990s, but with advancements in image quality, the homogeneity of grey-level intensity has been partially lost. Adaptive thresholding has been chosen for the proposed method. The only structure

with similar intensities of Hounsfield units are the airways, which were removed using the approach outlined in the Chapter 6 "Airways". The approach presented in this chapter results in the creation of a mask for emphysematous changes.

7.3 Methods

Two methods for adaptive thresholding of a CT series were tested and compared. The first method, the Approximate Threshold Estimation (ATE), was based on the Mimseg method from the work of Binczyk et al. [200]. The pipeline of the method is presented in Figure 7.1. The second method tested was the Exact Threshold Estimation (ETE) method; the pipeline of the method is presented in Figure 7.2.

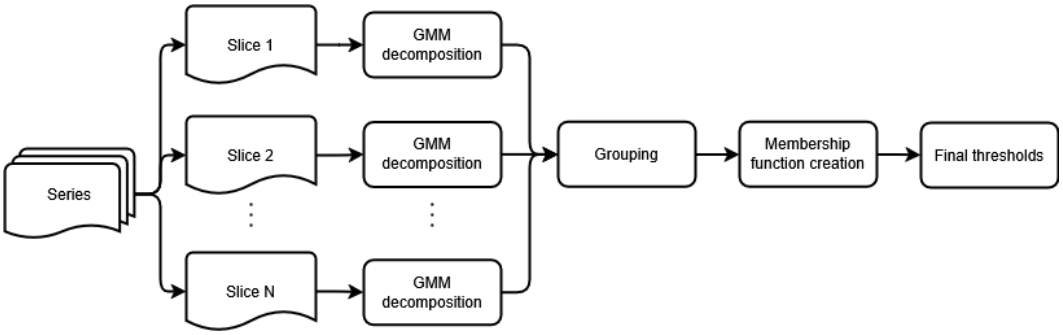

Figure 7.1: Approximate Threshold Estimation (ATE) pipeline.

Both methods aim to use Gaussian mixture models (GMM) decomposition to estimate segmentation thresholds for the image. Both methods analyse the 3D image section by section by decomposing it into Gaussian components represented by the normal distribution parameters. The main difference between the methods concerns the point at which the components are clustered. In the ATE method, the clustering occurs after the Gaussian components have been separated in 3D space, while in the ETE method, the thresholds for the cross-sections are determined first, which are clustered between the cross-sections instead of the distribution parameters. Detailed descriptions of the methods are given below.

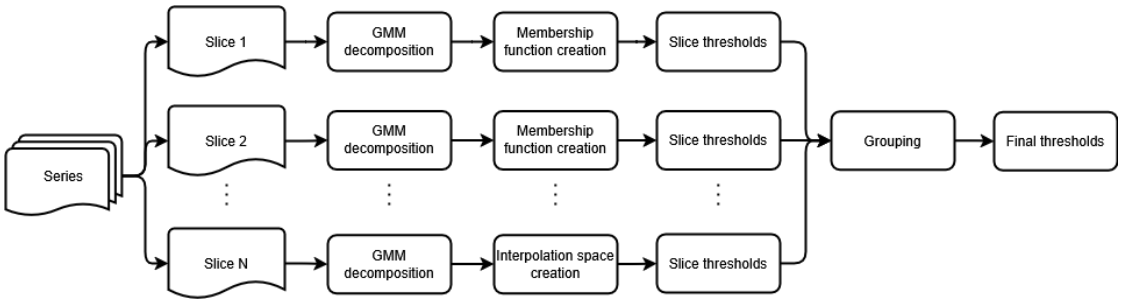

Figure 7.2: Exact Threshold Estimation (ETE) pipeline.

7.3.1 Preprocessing

The lung region was extracted from the original CT series and the bronchial tree was removed based on previously developed algorithms. The image prepared in this way, denoted by S, was iteratively analysed in the axial direction, where cross sections in which the lung parenchyma represented only 10% or less of the total area were eliminated.

7.3.2 GMM decomposition

The prepared cross-sections were decomposed into a set of normal distributions using Gaussian mixture modelling (GMM). Given the signal (density of the voxel grey levels) GMM aims to decompose it into a collection of Gaussian distributions called components. The probability density function for each distribution in the GMM is defined by the Eq 7.1.

$$\mathcal{N}(X|\mu,\sigma) = \frac{1}{\sigma\sqrt{2\pi}} e^{-(x-\mu)^2/2\sigma^2} \tag{7.1}$$

Where X is an input data, x is an input data point, μ is the mean of the Gaussian distribution, and *sigma* is the standard deviation of the Gaussian distribution. Assuming there are K different distributions, the probability density function for the Gaussian Mixture Model is defined by Eq. 7.2.

$$p(X) = \sum_{k=1}^{K} \alpha_k \mathcal{N}(\mathbf{X}|\mu_k,\sigma_k) \tag{7.2}$$

Where the α symbol denotes a mixing coefficient of k distribution. The following steps make up the mixture modelling process:

1. Initialise values of μ, σ and α for every distribution,

   Values can be initialised randomly, can be given manually or can be created by an algorithm, like for example k-means.

2. Expectation step - calculating $p(\theta_k|\mathbf{X})$,

   Parameters of the distributions in the mixture are estimated using the Expectation Maximisation algorithm. It calculates the likelihood function of the data given the parameters (Eq. 7.3).

$$\mathcal{L} = p(\mathbf{X}|\mu_k, \sigma_k) = \prod_{n=1}^{N} p(x_n) = \prod_{n=1}^{N} \sum_{k=1}^{K} \alpha_k \mathcal{N}(\mathbf{x_n}|\mu_k, \sigma_k) \tag{7.3}$$

   To simplify the computations the likelihood function is transformed into the log-likelihood function (Eq. 7.4).

$$\mathcal{LL} = ln(\mathcal{L}) = \sum_{n=1}^{N} ln \sum_{k=1}^{K} \alpha_k l\mathcal{N}(\mathbf{x_n}|\mu_k, \sigma_k) \tag{7.4}$$

   Assuming that θ is a set of attributes for k-th component. To estimate parameters based on log-likelihood, hidden variables based on the Bayesian Theorem are computed using Eq. 7.5.

$$p(\theta_k|\mathbf{X}) = \frac{\alpha_k \mathcal{N}(\mathbf{X}|\mu_k, \sigma_k)}{\sum_{k=1}^{K} \alpha_k \mathcal{N}(\mathbf{X}|\mu_k, \sigma_k)} \tag{7.5}$$

3. Maximization step - calculate μ^{i+1}, σ^{i+1} and α^{i+1},

   To find the maximum log-likelihood function, the derivatives over $\mathcal{LL}$ parameters μ, σ and α are calculated, the derivatives then have to be 0. Equations are shown below for following μ Eq. 7.6, σ Eq. 7.7 and α Eq. 7.8.

$$\mu_k^{i+1} = \frac{\sum_{n=1}^{N} p(\theta_k|\mathbf{X}) x_n}{\sum_{n=1}^{N} p(\theta_k|\mathbf{X})} \tag{7.6}$$

$$(\sigma_k^{i+1})^2 = \frac{\sum_{n=1}^{N} p(\theta_k|\mathbf{X})(x_n - \mu_k^{i+1})^2}{\sum_{n=1}^{N} p(\theta_k|\mathbf{X})} \tag{7.7}$$

$$\alpha_k^{i+1} = \frac{\sum_{n=1}^{N} p(\theta_k|\mathbf{X})}{N} \tag{7.8}$$

4. Calculate log-likelihood for new parameters,

5. If convergence stops, else go to step 2.

Multiple numbers of desired mixtures/distributions k were tested from 3 to 10. For each k Bayesian inference criterion (BIC) was calculated. Bayesian inference criterion (BIC) [201] is a measure used in statistics; it grades model quality considering the complexity of the model and its fit to the data. It is used mainly to compare multiple models to select the best one by balancing the number of parameters and the likelihood of fit (Eq. 7.9).

$$\mathrm{BIC} = k\ln(n) - 2\ln(\hat{L}) \tag{7.9}$$

k - number of model parameters (in the GMM case, number of mixtures),

n - number of observations,

$\hat{L}$ - the likelihood of parameter fit (in GMM case, defined by 7.4).

A lower BIC value indicates a better model; the model fits the data well with a minimal number of parameters. BIC is a similar measure to the AIC (Akaike Information Criterion), but in comparison, BIC penalises the model more for its complexity.

The optimal number of mixtures was determined by the selection of the model with the lowest BIC. Once the optimal Gaussian mixture model for the cross section was obtained, each resulting distribution was analysed, eliminating distributions where the value of α is less than 0.01. As a result, for the series, the collection of μ, σ and α was obtained with the indication for which slice the parameters were estimated.

7.3.3 Grouping

The grouping phase is performed in the different parts of the pipeline for ATE and ETE methods. For ATE, the grouping was performed in the middle of the pipeline, right after the per-slice GMM decomposition; for ETE, it is a pre-last step of the pipeline, performed after the derivation of the slice thresholds.

Gaussian Mixture Models (GMM) were used for the ATE, grouping was performed in the 3D space of α, μ and σ. The GMM was initialised with a full covariance matrix and weighted by 2 in the μ feature space. An optimal number n of clusters was derived using the BIC criterion, where n with the smallest BIC score was selected.

K-means was used for the ETE, grouping was performed in the space of the threshold derived later in the pipeline. Cluster centres were initialised using the kmeans++ method. The optimal number of clusters n was calculated based on the inertia, that is, on the sum of the squares of the cluster points' distances from their centre. The inertia is tracked through the changing n, and the point of the largest change between consecutive inertia values is selected as the optimal n.

7.3.4 Membership function creation

A membership space was created from the Gaussian mixtures. The membership space consists of a x vector and y array, the x vector stores sorted values ranging from a minimum value of the voxel in the series to the maximum value of the voxel in the series with a 0.1 step difference between consecutive numbers. The array y contains Gaussian probability density functions calculated based on the vector x and the parameters of the mixtures. The values stored in y were normalised at each point x_i where $min(S) \leq i \leq max(S)$ so that at each $\sum_{j=1}^{k} y_{ij} = 1$.

7.3.5 Slice thresholds

For the ETE, the cut-off thresholds were derived for each cross-section based on the membership function. The order in which the cross-sections are processed was irrelevant; therefore, the operation was performed in parallel. After obtaining a set of thresholds for all cross-sections in the series, the thresholds stored in the matrix are subjected to a clustering operation.

7.3.6 Final Thresholds

Cut-off thresholds are determined at the intersections of the curves of the membership function. For ATE, the final cut-off thresholds were derived based on the membership function created from the clusters created in the α, μ, and σ space, as shown in Figure 7.3.

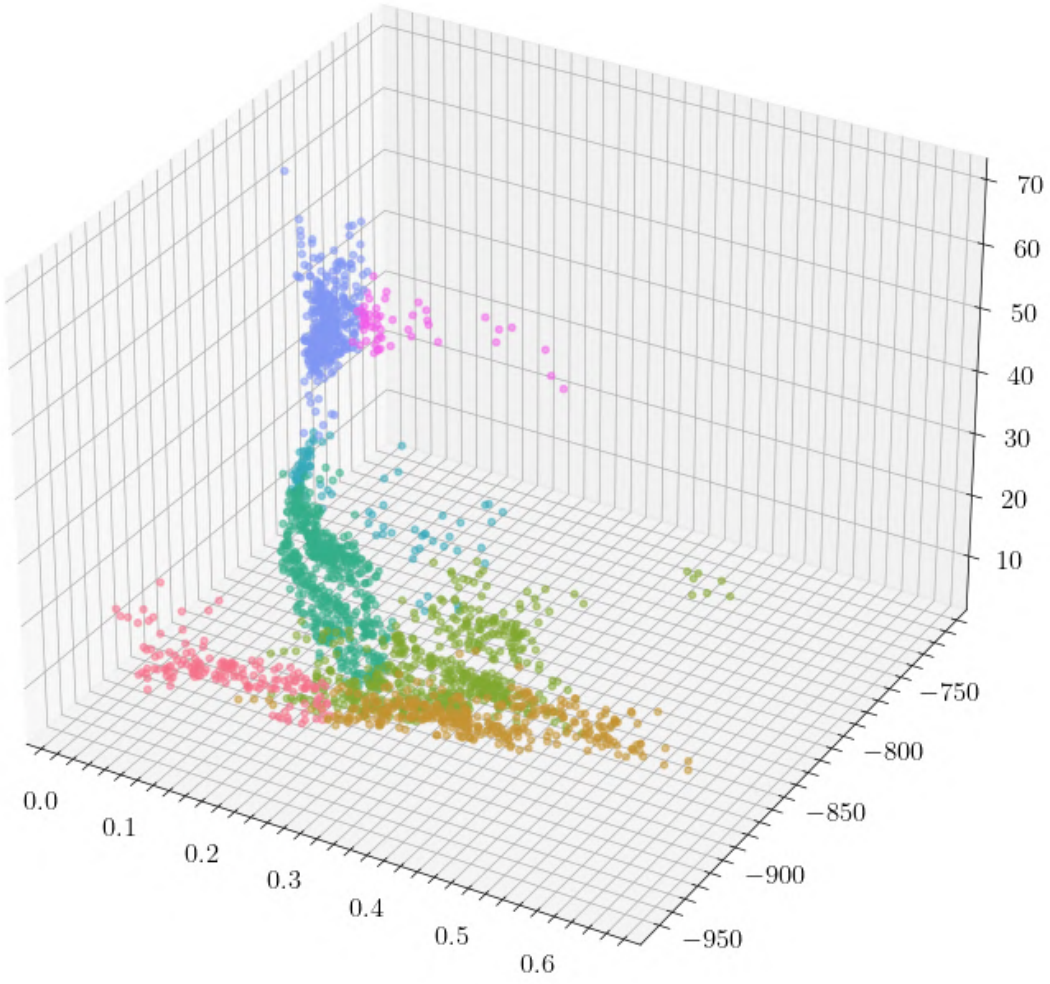

Figure 7.3: Three-dimensional space of normal distribution parameters (mean, std and alpha) showing final clusters coloured by threshold resulting from the ATE method.

For ETE, the final cut-off thresholds were obtained by taking the x-value of the centroids of the clusters from the grouping phase, as shown in Figure 7.4.

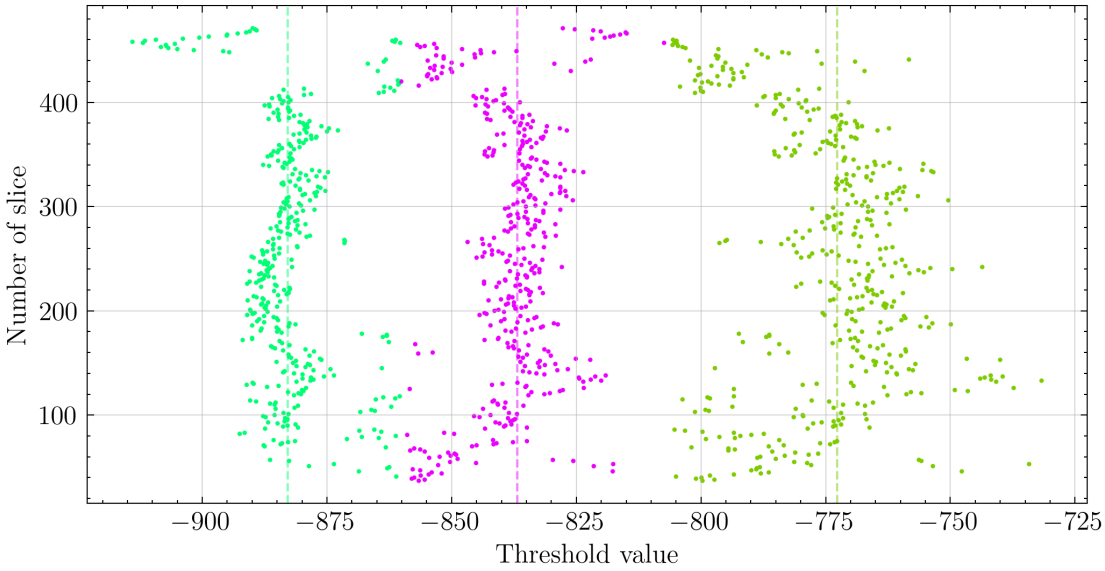

Figure 7.4: Final clusters and threshold resulting from the ETE method.

7.3.7 Comparative analysis of methods

From the set of COPDGene images, those with clear emphysematous changes and those without were collected. The sum of the segmentation HU distribution values for both methods was calculated and normalised by the number of patients. Expected values were derived based on the summed distributions; the expected value of the no-changes group marked the threshold that indicated a lack of emphysematous lesions in the patientś lung parenchyma. The CT series without emphysematous lesions were removed from the comparative analysis of methods.

The difference between ATE and ETE emphysema threshold values was calculated. A Jarque-Bera test at a significance level of $\alpha = 0.05$ was applied, with the null hypothesis stating that a normal distribution can model the distribution of the given samples. The selection of the Jarque-Bera test was motivated by the large sample size. Following that, either the Mann-Whitney U Test or the Wilcoxon tests were conducted. The selection of the test depended on the outcome of the Jarque-Bera test. The Paired T-test would have been conducted if the null hypothesis of the Jarque-Bera test was not rejected, and the Wilcoxon test would have been conducted if the null hypothesis of the Jarque-Bera test was rejected. Both tests were executed at a significance level of $\alpha = 0.05$, with the null hypothesis suggesting equivalency in the means/medians of the compared groups. Both test results were supported by the effect size in the form of a

rank-biserial correlation. If a significant difference was found, the tests were conducted independently on the GOLD groups within the scope of the COPDGene dataset.

It is important to note that the number of samples per GOLD group is different, thus the p-values resulting from the test cannot be compared. In such a situation, it is recommended to analyse the significance of the results based on the effect size ES. Based on the work of Cohen et al. [202] the Wilcoxon test assumes that differences between values are negligible when $|ES| \in [0, 0.125]$, are small when $|ES| \in [0.125, 0.304]$, are medium when $|ES| \in [0.304, 0.465]$ and are large when $|ES| \in [0.465, 1]$. The sign of ES indicates the direction of the effect. If the effect is positive, then the ranks of the first group's values are larger; if it is negative, then the second group's ranks are larger. Given the data analysed, a positive ES value means that the ATE method has lower thresholds, and a negative ES value means that the ETE method has lower thresholds.

At this stage of the analysis, it is assumed that only images containing emphysematous lesions are analysed. This assumption results from the first step of the analysis. This means that any differences in thresholds will indicate an overestimation or underestimation of the lesion area by one of the methods. To determine whether there is an overestimation or underestimation, this part of the analysis was paired with a trend analysis of the volume of change in the group. Regarding the analysis of the COPDGene data, it must be kept in mind that GOLD values do not directly indicate the presence or absence of changes. Therefore, GOLD values and lesion volumes are not expected to be directly correlated. However, a trend indicating an increase in lesion volume with the GOLD standard is expected.

7.4 Results

The lung area was extracted from chest CT scans, and the bronchial tree, delineated by the methods detailed earlier, was excluded. These modified images were then processed using an adaptive thresholding technique. This procedure resulted in a segmentation divided into n segments, where n differed among patients. For ATE, the thresholds are drawn at the intersections of the membership functions; the average value of the number of thresholds is 3.66 with a standard deviation of 1.14. For ETE, the thresholds are drawn from the centroids of the clusters; the average value of the number of thresholds is 4.81 with a standard deviation of 1.24. This results in an anticipated outcome of 4 to 6 segments appearing on the output segmentation for both

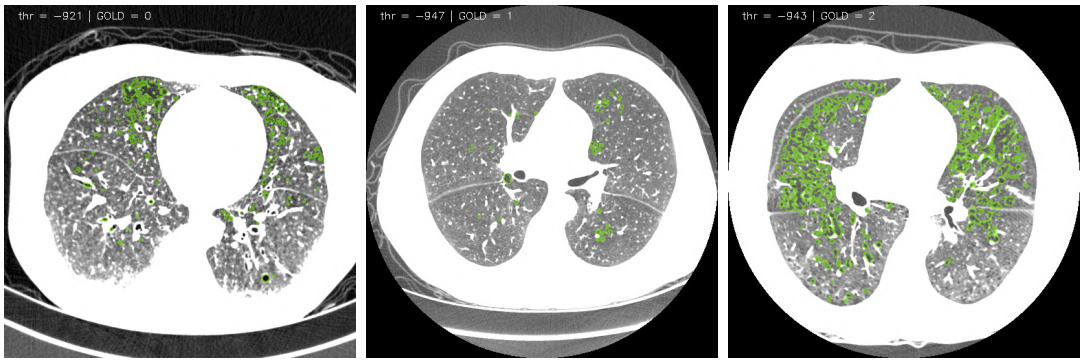

(a) GOLD 0 (b) GOLD 1 (c) GOLD 2

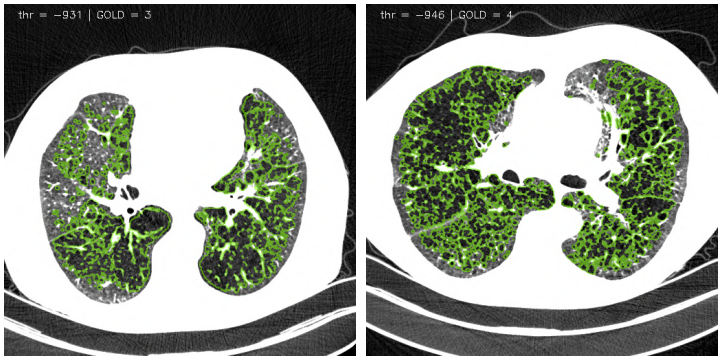

(d) GOLD 3 (e) GOLD 4

Figure 7.5: Example results of ATE segmentation method shown on CT patient images with each GOLD standard classification a) GOLD 0, b) GOLD 1, c) GOLD 2, d) GOLD 3, e) GOLD 4.

methods. Despite the large amount of information, only the first and second segments were analysed. The first segment contains the tissue with the lowest attenuation values, the air. As described in the Anatomy chapter, emphysematous lesions lead to the destruction of alveoli, causing them to merge and create a hollow area. The space is then filled with air, hence the low attenuation values. The second segment contains healthy lung parenchyma with alveoli whose walls increase the attenuation coefficient. The rest of the segments represent other structures present in the lung such as vessels, interlobular septa, and other lesions. Example segmentation results are presented in Figure 7.5.

The methods described in this chapter are used for automatic and unsupervised segmentation of emphysematous lesions. In their absence, the determined threshold should describe the HU values of the lung parenchyma. To determine the value of this threshold, 171 images from the GOLD 0 group, which did not contain emphysema,

and 330 images from the other groups, which contained emphysematous lesions, were selected from the COPDGene collection. Based on the calculated segmentations in both methods, a histogram of these segmentations, ranging from -1000 HU to -800 HU was plotted. Histograms were graphed based on lesion occurrence, and then the histogram bar values were summed and divided by the number of patients in the group. This produced two curves with expected values defined by their peak and intersecting at one point.

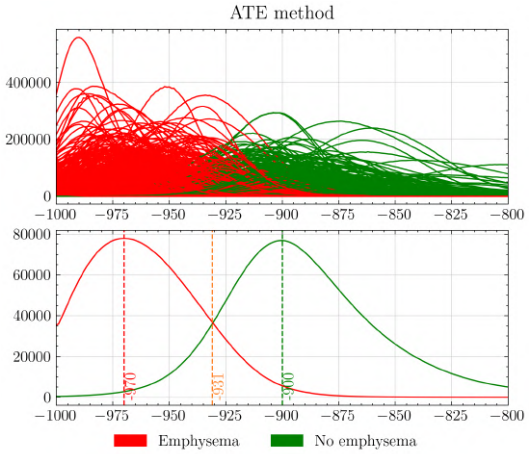

(a) Emphysema segmentations ATE HU values distributions of patients with changes (red) and without changes (green).

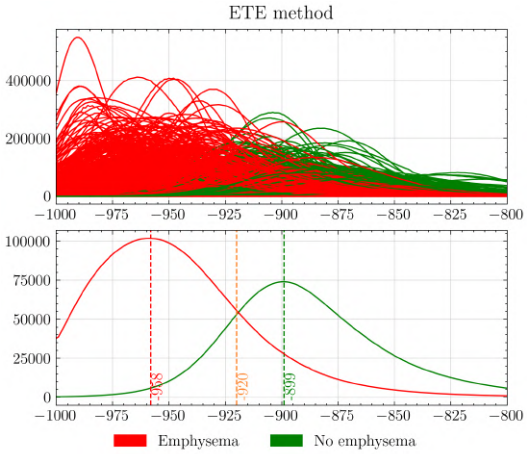

(b) Emphysema segmentations ATE HU values distributions of patients with changes (red) and without changes (green).

Figure 7.6: Distibutions of HU values in the segmentations done by ATE and ETE methods in patients with and without emphysema.

The expected value for the ATE method in the case of the Emphysema class is -970 HU and in the No emphysema class is -900 HU 7.6a. The ETE method's expected value in the Emphysema class is -958 HU and in the No emphysema class is -899 HU 7.6b. The literature reveals that emphysema changes fall within the threshold range of -900 HU to -1000 HU (Chapter 3.8.4). Based on the results and literature, the threshold deciding whether the emphysema is present was set to -900 HU. This suggests all series with thresholds over -900 HU do not contain emphysematous changes.

Before competitive analysis, the series with threshold values over the -900 HU were separated from the set resulting in the data with a sample size of 1029. The difference d between the thresholds t from ATE and ETE methods was calculated $d = t_{ATE} - t_{ETE}$. The Jarque-Bera test for normality indicated that the data significantly deviates from a normal distribution, $p < 10^{-6}$, $W = 126.771$. Because the sample size is large, the

normality test results could be wrong. In addition, the qqplot was made and is shown in Figure 7.7. Most samples deviate greatly from the diagonal and are not included in the confidence intervals. Therefore, the assumption of normality is violated.

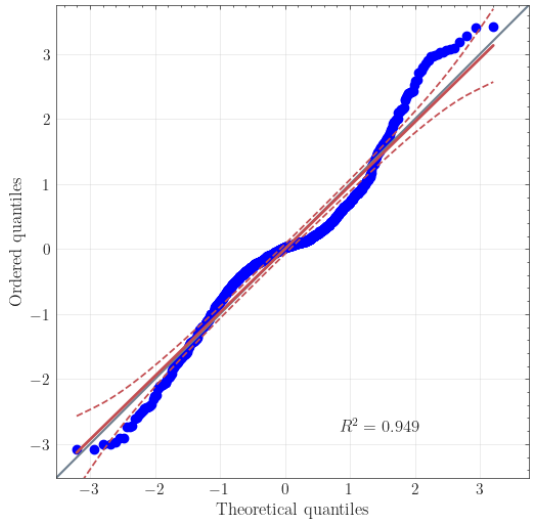

Figure 7.7: The qqplot of the differences between $ATE - ETE$ methods shows that it is not normally distributed data.

The non-parametric Wilcoxon test revealed a significant difference between the two thresholds (p = 0.0146, RBC = −0.0953). The Wilcoxon test was repeated for each group to see differences in cut-off thresholds between groups. Significant differences in cut-off thresholds were observed for the first three GOLD grades, GOLD 0 with p-value = 0.029500 and RBC = 0.240367, for GOLD 1 p-value = 0.013416 and RBC = −0.394775, for GOLD 2 p-value = 0.041328 and RBC = −0.140190. For GOLD 3 and GOLD 4, the p-values indicated no difference between the threshold values, with GOLD 3 p-value = 0.177675 with RBC = −0.097215 and GOLD 4 p-value = 0.058607 and RBC = −0.163969. Figure 7.8 shows differences between thresholds per the GOLD standard.

The non-parametric Wilcoxon was performed per GOLD group, where the effect size RBC was emphasised and analysis was paired with emphysema volume trend analysis (Figure 7.9). Additionally, the box plot of differences was plotted in Figure 7.8. The results of the Wilcoxon test with the sample sizes of groups were stored in Table 7.1. All RBC values are negative, indicating lower thresholds in the ETE method. In the GOLD 0 group $|RBC| < 0.125$ which indicates a negligible difference in method thresholds. As can be seen in Figure 7.8, the median value of the difference is close to zero, but their interquartile range is the largest relative to the other groups. Its upper quantile is

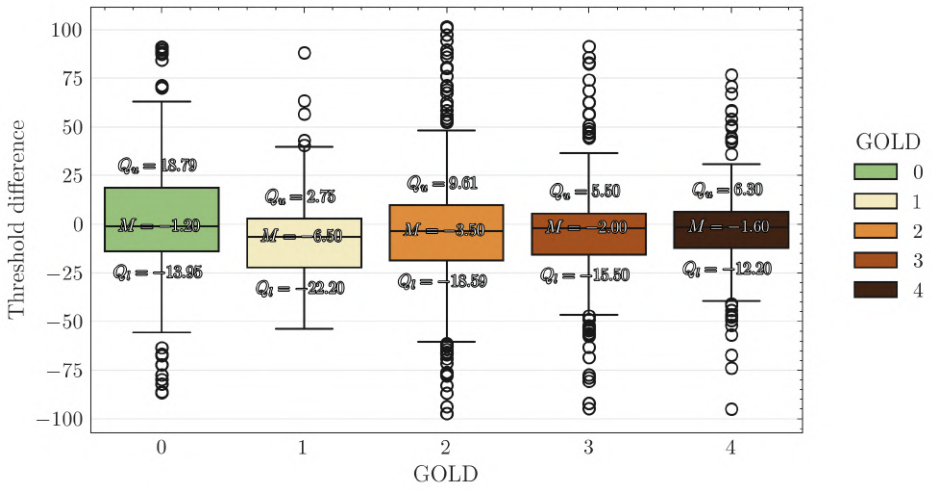

Figure 7.8: Boxplots showing the difference in the thresholds between the ATE and ETE method per-GOLD standard group.

GOLD	N	p-value	W	RBC
GOLD 0 Wilcoxon	144	0.776266	5077.0	-0.027395
GOLD 1 Wilcoxon	57	0.025055	544.0	-0.341803
GOLD 2 Wilcoxon	342	0.002034	23388.5	-0.193083
GOLD 3 Wilcoxon	289	0.001806	16515.0	-0.211789
GOLD 4 Wilcoxon	197	0.065725	8276.5	-0.151259

Table 7.1: Non-parametric Wilcoxon test results showing the strength of the thresholds difference in ATE and ETE methods.

close to the value of 18.79, and its lower quantile is -13.95, indicating greater variation in the threshold values of the ATE method. GOLD 1 $0.304 < |RBC| < 0.465$ indicates a medium effect; the ETE method is more sensitive and returns lower threshold values. Lower threshold values result in small segmented regions. In the GOLD 2 group $0.125 < |RBC| < 0.304$ indicates a small effect, meaning there are small differences in thresholds. In the difference boxplot shown in Figure 7.8, GOLD 2 has the largest and most outliers, with values as high as 100 and as low as -100. The GOLD 3 group and GOLD 4 both have $0.125 < |RBC| < 0.304$, indicating a small effect in both groups. They both have narrow standard deviations, as shown in Figure 7.8.

The calculated thresholds were used to segment the lesions after the removal of the bronchial tree. Volumes were calculated from the segmentations created and subjected

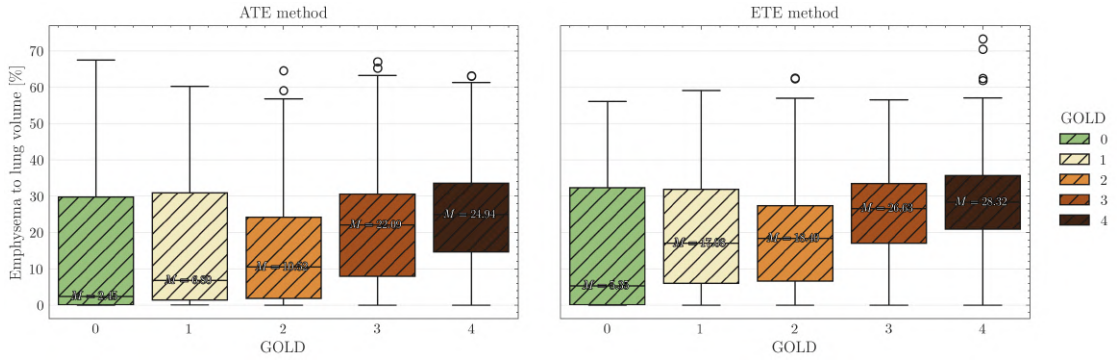

Figure 7.9: Segmented masks' volumes using ATE and ETE methods.

to trend analysis. Figure 7.9 shows boxplots of lesion volumes segmented by GOLD and by the method. The result of the Jonckheere-Terpstra test indicated an increasing trend for the ATE ($p-value < 1*10^{-6}$) and ETE ($p-value < 1*10^{-6}$) methods. Both methods have a positive trend and similar distances between group medians. Therefore, it was checked how many lesions are clinically significant, i.e. make up at least 5% of the total lung volume. The results of the ATE method consist of 91.042% clinically relevant segmentations, whereas the ETE method consists of 89.638% clinically relevant segmentations. The analysis shows that the ETE method has a higher tendency to under-segment.

Both methods give promising results, but based on the analysis of cut-off threshold differences and segmentation volume trends, the ATE method is the better choice. In the case of method ETE, there is a risk of under-segmentation.

7.5 Discussion

The cut-off threshold for images without emphysematous changes was determined based on the analysis of the distributions of individuals with and without changes presented in Figure 7.6. It was assumed that if the cut-off threshold is greater than -900 HU, then no change is assumed. The threshold value was determined for statistical analysis to minimise False Positives (FP). However, this is not a universal threshold value. Figure 7.10 shows two cases of GOLD 3 images with a cut-off of (a) -888 and (b) -893. Both cases have extensive emphysematous lesions and their lung images were taken on inspiration and with a standard reconstruction kernel. However, presumably due to a poor choice of parameters concerning the patient's carcasses, or deliberately

underestimating the radiation intensity due to the patient's health status, the emphysematous lesions seen in the cross-sectional images have higher HU values than in the other cases.

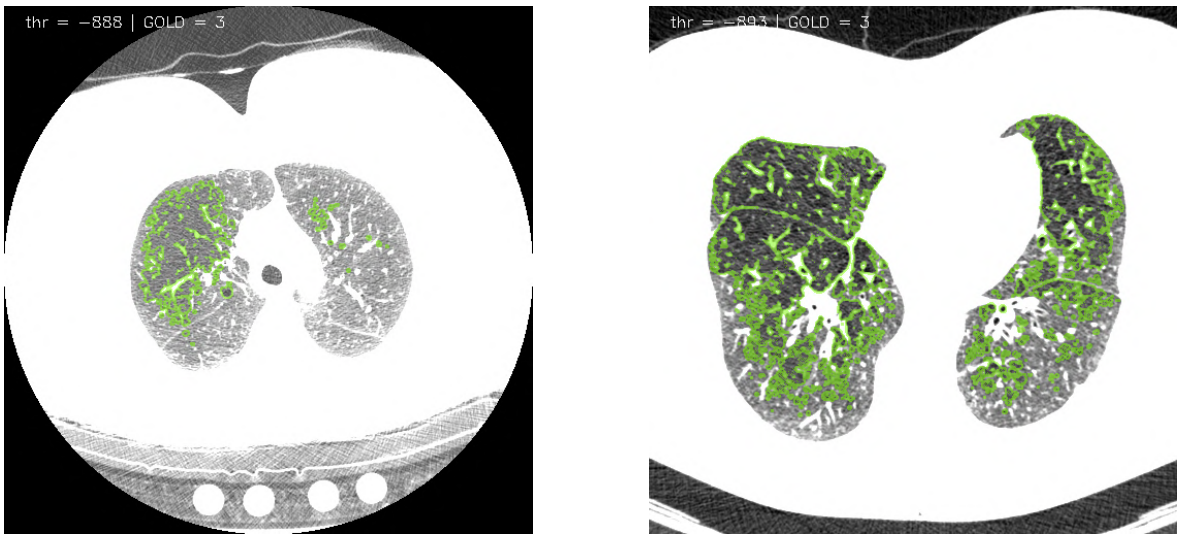

(a) Patient COPDGene_A76645 GOLD 3, CT scan taken at inspiration with the standard kernel.

(b) Patient COPDGene_G46462 GOLD 3, CT scan taken at inspiration with standard kernel.

Figure 7.10: Example CT images' axial slices of patients from the GOLD 3 group with emphysematous changes whose thresholds were above -900 HU values.

In addition to emphysema, the method can segment other lesions such as consolidations or ground-glass opacities. The method returns a range of cut-off thresholds indicating different tissues. Once the input has been appropriately adjusted and the thresholds analysed to detect an automatically appropriate range of Hounsfield unit values, the method can potentially be used with other diseases.

Chapter 8

Quantification and mapping

This chapter describes the method for quantification of the emphysematous changes. The main goal of quantification is to summarise findings, in this case, abnormal lung changes, into a format from which quick conclusions can be drawn.

A novel emphysema quantification method is introduced. It operates by utilising the segmentation results discussed in the prior chapter, "Low attenuation patterns." The approach involves extracting features from the ROI and mapping them onto a 2D space to illustrate patient differences and similarities. Subsequently, this quantification technique is compared with the GOLD standard value derived from spirometry results.

8.1 Motivation

Providing only a baseline mask of emphysematous lesions in the output is insufficient for diagnostic purposes. From the point of view of the medical practitioner, it is crucial to determine the type, distribution, and extent of parenchymal destruction. Most of the available methods for assessing the severity of COPD are limited to environmental interviews or spirometric examinations. When it comes to assessing the lesions visible on CT scans, the analysis is usually limited to calculating the volume of the lesions in relation to the total lung area, that is, determining the low attenuation area (LAA) mentioned in the "Biological background" Subsection 3.8 "Quantification of emphysema and COPD". Using information derived from the COPDGene dataset in the form of radiomic features, the dissertation aims to visualise similarities between different cases of emphysema. This approach will enable better and faster adaptation

of treatment to the patient's needs.

8.2 State of the art

Most of the classical methods for the quantification of emphysema used by medical practitioners have been outlined in the chapter "Biological Background". The majority of the methods mentioned require supervision or depend on manual labour. In this state-of-the-art analysis, the emphasis will be put on the methods for automatic quantification of changes.

COPD progresses differently from patient to patient. Treatment must be adjusted according to the type of changes present in the parenchyma. In the Chapter 3 "Biological Background" Subsection 3.6.1 "Emphysema", three categories of emphysema were introduced: centrilobular, panlobular, and paraseptal emphysema. Each is characterised by a different extent, texture, and distribution. When evaluating the severity of the changes based on LAA, not all features of the emphysema subtypes are taken into account.

Many research papers have been produced that address the problem of automatic quantification of emphysematous lesions. These usually come down to two stages, the first being the description of the lesions by characteristics and the second being the classification of the lesions or their recognition. It all started with the texture features of the lesions proposed by Uppaluri et al. to classify emphysema [203]. From this, the quantification of emphysema lesions slowly gained traction, and researchers tested approaches using local binary patterns (LBP) [204] or its developed version, local ternary patterns (LTP) [205], mixing them with Gabor filters [206], or using different kernels for feature extraction [207]. However, the most popular solutions are currently based on radiomic features and neural networks. Radiomic features [208, 209], in other words, are a set of multiple values describing a mask-selected piece of tissue in a medical image. The set of radiomic features includes:

- First order features - basic statistics like mean and standard deviation,
- Shape features - for example, volume, size, sphericity of the object,
- Grey level co-occurrence matrix (GLCM) features - textural features based on the voxels' placement in space,

- Grey level size zone matrix (GLSZM) - size of the specific grey level zones,
- Grey level run length matrix (GLRLM) - length of consecutive voxels with the specific grey level,
- Neighboring grey-tone difference matrix (NGTDM) - quantifies differences between the neighbouring voxels,
- Grey level dependence matrix (GLDM) - describing the local texture information.

The radiomic features listed were tested in many ways; Cheplygina et al. proposed using a logistic classifier to assign patients to healthy and diseased groups [210]. Li et al. used the SVM algorithm for this task by giving the calculated lung radiomic features as input and additionally distinguishing between subtypes of COPD [211]. Yang et al. proposed two approaches to address this problem. The first approach involves selecting meaningful radiomic features of the lungs using the Lasso method, followed by dividing the images into subcategories using a multi-layer perceptron [212]. The second approach also selects differentiating features using the Lasso method, but the final classification is performed using a graph neural network [213]. Amudala et al. focused on the features of the lungs and bronchial tree by analysing their texture and shape and then using an algorithm from the Gradient Boosting family to perform the classification into healthy and COPD lungs [214].

The alternative for radiomic features are neural networks which, when trained properly, can encapsulate meaningful information from the image about the target against which they are trained. González et al. analysed a cohort of patients with a smoking history and COPD using a CNN network. The input was compromised from the 4 canonical CT views and trained according to the data set, either to predict the presence of COPD or to detect the GOLD stage [215]. Singla et al. trained a generative network with the latent space connected to the discriminator with the attention module. The goal was to predict FEV1 and FEV1/FVC scores indicating the spirometric capacity of the lungs [216]. Xu et al. trained the CNN network and used it purely as a feature extractor. Then, after feature dimension reduction by PCA, they fed them into k-Nearest-Neighbour, multiple-instance support vector machine, and expectation-maximisation diverse density. The goal was to identify and stage COPD disease [217]. Du et al. decided to evaluate the bronchial tree instead of the whole lung volume, as COPD damages it. They used CNN with Bayesian optimisation for feature extraction and a voting classifier to group the results into COPD and healthy classes [218]. Tang

et al. used a deep residual neural network to predict COPD presence defined based on the spirometry data. Input to the network were whole CT images split into the regions [219]. Ho et al. used parametric response mapping to highlight regions of emphysema, functional small-airway disease and normal lungs. Then, using CNN they classified the CT scans into COPD and healthy [220]. Chen et al. proposed a solution based on the graph convolutional neural network where CT scans were sliced into smaller cubes and whole volumes were classified into COPD and non-COPD classes [221]. Zhang et al. trained two DenseNet-201 CNN networks to decide whether a given patient has COPD or not. The difference is the first lung volume accepted by the network as input and the second bronchial walls as input. Information from networks was then combined by the logistic classifier [222]. Wu et al. used the snapshots of the lungs and bronchi tree in 3D to train their CNN network for COPD detection [223]. Sun et al. used the ResNet 18 architecture with an attention module to distinguish lungs with COPD from those without COPD. They sliced CT images in the axial plane and used them as input to the model [224]. Li et al. graph convolutional neural network classifying the COPD and non-COPD states. They automatically determined ROIs in the lung parenchyma and created spatial connections between them using a graph employing both spatial (location) and temporal (grey-level intensity values of ROIs) information in the learning process [225]. Wu et al. created attention-based neural networks which used three different input information: the slices of the CT image, the lung mask and the bronchi mask. Based on their output, the logistic classifier assigned labels of COPD or non-COPD state [223]. Xue et al. used a multiple-instance learning approach with an attention mechanism. The slices of the CT scan were iteratively passed to the network input, features were extracted, the attention mechanism assigned a weight to the slice, and then all slices were fused creating both information about the patient state (COPD or not) and CT slice where the disease is the most prevalent [226]. Yu et al. proposed a self-supervised neural network using a contrastive learning strategy for the emphysema detection task [227].

The mentioned works mostly use ECLIPSE [228] and COPDEGene [86] datasets or use their own CT scan collections. The papers focus on a binary classification into COPD and non-COPD, in some cases a multi-label classification into, for example, non-COPD, GOLD 1, GOLD 2, GOLD 3 and GOLD 4. There is a single paper considering the regression task on the output values of FEV1 and FEV1 / FVC spirometry. The articles use raw CT images of lung masks and/or bronchial masks as input data for both the radiomics and neural networks.

Doctors and medical professionals approach any AI solution with caution. A tool that provides just a label with the conclusion is not sufficient. The patient's well-being and life are on the line, so it is important to explain the AI results [229, 230]. Some methods presented in the articles use xAI tools to provide visualisations of network activations indicating locations on CT scans based on which the neural network based its result [216, 218, 220, 222, 223, 224, 226]. This approach is promising but raises concerns about trust in the case of controversial xAI results. For instance, if the activation map extends into the background but still includes some abnormal changes, it becomes unclear whether the decision is based more on the background or the changes. It is possible that, in many training cases, changes were typically present in that specific region, or the training images from a particular imaging centre might have had characteristic background values. The neural network approach is not yet suited for diagnostic purposes, but with a sufficiently diverse dataset and high NPV, PPV, sensitivity, and specificity values, they can be used as a screening tool [27, 28]. Radiomic-based approaches do not suffer from such problems as neural networks have, yet extraction of radiomic features from the whole lung volume may lead to the omission of less prevalent changes.

Due to the mentioned problems, the quantification method presented in this dissertation will rely on the created emphysema masks. By including a resultant mask, the medical practitioner will be able to view the area against which the calculations are made and be assured that only those voxels are the essence of the analysis. In addition, the resulting quantification decision will not be a class; it will be a map of relationships between cases. The presented quantification method aims not to make decisions for the physician, but only to support his/her diagnostic abilities by depicting the relationships between different cases of COPD in 2D space.

8.3 Methods

The proposed method aims to show the relationship between the different cases of COPD. It is based on radiomic features, which, after undergoing a series of operations such as preprocessing, feature selection, and embedding, are finally presented in 2D space.

8.3.1 Splitting emphysema mask to ROIs

A full emphysematous lesion mask can include multiple lobes and can occur in both the left and right lungs. To extract features from the masks that reflect the character of the lesions, the mask was divided into regions of interest (ROI). The first step was to divide the lesion mask into lobes. Subsequently, in each patch, sub-areas were separated using the K-Means algorithm, where clustering took place in the 3D space of the standardised coordinates of the mask's voxels. The number of components for K-Means was selected automatically using the elbow method, where the measured value was inertia, for example, the sum of the square of the distance of a point and the centroid of its cluster. The result was a mask that contained N clusters divided into two lungs and 5 lung lobes.

8.3.2 Features Extraction

Three sets of features were calculated; the first set was radiomic features [208, 209] extracted from the ROI. The contours were drawn in the 3-voxel space around the ROI, from which the second set of radiomic features was calculated. The third set of features was related to the spatial position of the ROI. A vector was drawn from the lung's weighted centre to the ROI's centre; the angle in x, y, and z, and the magnitude of the vector directions were recorded. In total, 156 features were calculated per ROI.

For radiomic features calculation, the pyRadiomics package was used; it contains 7 feature groups amounting in total to 110 features. The first group is First-Order Statistics, which quantifies the distribution of voxel intensities within the region of interest (ROI). They are used to assess the overall intensity patterns of the ROI. The second group is Shape-Based Features, which describes the geometric properties of the ROI. This set was not calculated for the contour features. The third group is Grey Level Co-occurrence Matrix (GLCM) Features, which measure texture by analysing the spatial relationship between pairs of voxel intensities. It evaluates fine textures and spatial intensity variations. The fourth group is the Grey Level Run Length Matrix (GLRLM) Features group, which quantifies the length of consecutive voxels with the same intensity along a specified direction, which is evaluated at multiple angles. It is used to detect uniform textural patterns. The fifth group belongs to Grey Level Size Zone Matrix (GLSZM) Features, which measure the size of connected regions (zones) of voxels with the same intensity. It has a similar usage as GLRLM; it also quantifies the

appearance of the same intensity values, but it is done in zones rather than in a specific direction. The sixth group is Grey Level Dependence Matrix (GLDM) Features, which measure the degree of voxel intensity dependence within the ROI. It analyses how a voxel in the centre affects its neighbourhood. The final seventh group, Neighbouring Grey Tone Difference Matrix (NGTDM) Features, analyses the contrast and texture by assessing the difference between a voxel's intensity and its neighbours.

Sets of features were recorded for each patient for each region of interest (ROI) within the patient's segmentation. To aggregate information per patient, the mean, median, minimum, maximum, and standard deviation were calculated for each feature per patient. This expanded the number of features from 156 to 780.

8.3.3 Preprocessing

Initially, features with zero variance were removed from the complete set in the method's pipeline. The features that remained were standardised using the features' mean and standard deviation. The PCA technique was then employed for the initial dimension reduction, selecting components that accounted for 90% of the variance.

Principal Components Analysis (PCA) is a linear dimensionality reduction technique. PCA identifies the directions (principal components) along which the variance in the data is maximised, transforming the data into a new coordinate system where the dimensions are uncorrelated. The following steps can describe the whole transformation process:

Assuming that $X \in R^{np}$ where n is a number of observations, p is a number of features, and k is the desired number of components.

1. Data standardisation - it is an important step because if features have different scales (for example, were measured in different units), those with larger magnitudes will dominate the principal components. For scaling, usually z-score normalisation is used Eq. 8.1.

$$z = \frac{x - \mu}{\sigma} \tag{8.1}$$

Where x is a feature sample, μ is the feature mean and σ is the feature standard deviation.

2. Calculation of covariance matrix - it is a symmetric matrix capturing the pairwise relationships between features Eq. 8.2.

$$\Sigma = \frac{1}{N-1} \sum_{i=1}^{N} (\mathbf{x}_i - \mu) (\mathbf{x}_i - \mu)^T \tag{8.2}$$

3. The eigenvalues λ_j and eigenvectors v_j of principal component directions j are then computed using property Eq. 8.3 and solving the Eq. 8.4.

$$\det(\Sigma - \lambda_j I) = 0 \tag{8.3}$$

$$\Sigma \mathbf{v_j} = \lambda_j \mathbf{v_j} \tag{8.4}$$

The eigenvalues λ_1, λ_2,..., λ_j (sorted in descending order) represent the variance explained by the corresponding principal components.

4. Projection on the eigenvectors - the top k components are selected based on the eigenvalues, and the matrix W of v eigenvectors is formed Eq. 8.5.

$$W = [v_1, v_2, \ldots, v_k] \in \mathbb{R}^{p \times k}. \tag{8.5}$$

Original data X into the new k-dimensional subspace Eq. 8.6.

$$Z = XW, \tag{8.6}$$

where $Z \in \mathbb{R}^{n \times k}$ is the transformed dataset, where each row of Z represent new sample basis.

8.3.4 Embedding

The Uniform Manifold Approximation and Projection (UMAP) method [231] was used to create embeddings for dimension reduction. UMAP is a dimensionality reduction technique that models high-dimensional data by constructing a weighted graph representing its local structure. Using a cost function optimises a low-dimensional representation by minimising the difference between the high- and low-dimensional graphs. The method has many hyperparameters; among the most influential on the final result

are the distance metric $d(...)$, the number of neighbours k, and the minimum distance between points d_{min}. The UMAP development process is based on a solid mathematical foundation and draws from graph theory, differential geometry, and topology theory. The paper will present the general idea of how the method works, which can be divided into three main steps:

1. Construction of a weighted neighbourhood graph in a high-dimensional space

   Let the input dataset be $X = \{x_1, x_2, \ldots, x_N\}$ for each point, its distance from other points in space is calculated using a chosen metric, such as Euclidean distance. The sets of k-nearest neighbours for each point are thus determined.

   For each x_i, ρ_i and σ_i are defined. Where ρ_i provides a connection between x_i and at least one other data point Eq. 8.7.

$$\rho_i = \min\{d(x_i, x_{i_j}) \mid 1 \leq j \leq k, d(x_i, x_{i_j}) > 0\} \tag{8.7}$$

   The parameter σ_i is a local scaling factor determining how 'wide' the local neighbourhood area around point x_i is. In practice, σ_i is adjusted so that the number of neighbours of a given point in the graph corresponds to the desired value of the k neighbours Eq. 8.8.

$$\sum_{j=1}^{k} \exp\left(\frac{-\max(d(x_i, x_{i_j}), 0) - \rho_i}{\sigma_i}\right) = \log_2(k) \tag{8.8}$$

   The parameter σ introduces local differences in space, meaning that at each point x_i the data space is viewed from the perspective of the local distance 'scale'.

   Finally, the equation for the weight of edges in a weighted graph can be written for the point x_i Eq. 8.9.

$$w(x_i, x_{i_j}) = \exp\left(\frac{-\max(d(x_i, x_{i_j}), 0) - \rho_i}{\sigma_i}\right) \tag{8.9}$$

   Notably, any points x_i and x_j have a bidirectional relation on a weighted graph. Their weights must be symmetrised (b the resulting symmetric value) using Eq. 8.10.

$$b_{ij} = w_{ij} + w_{ji} - w_{ij} \cdot w_{ji} \tag{8.10}$$

2. Low-dimensional space construction

   The low-dimensional space is created using the Spectral Embedding method. This is a non-linear method to reduce the dimensionality of data presented as a weighted graph [232]. Like PCA, Spectral Embedding uses eigenvalues and eigenvectors for this purpose; however, it does not operate on the covariance matrix; it uses the Laplacian graph L. Under the assumption that A represents a weighted adjacency matrix (containing symmetrized weights) and D is a diagonal degree matrix for a graph A (sum of edges' weights connected to the nodes in each diagonal element), then Laplacian can be calculated using Eq. 8.11.

$$L = D^{1/2}(D - A)D^{1/2} \tag{8.11}$$

   Then the eigenvalues and eigenvectors are calculated by solving Eq. 8.12, and sorted in descending order.

$$Lv = \lambda Dv \tag{8.12}$$

   The top n eigenvalues represent the new embedding space.

3. Low-dimensional space optimisation

   UMAP use the attraction and repulsion forces to optimise the low-embedding space. For each neighbourhood, the sample is selected from which the attraction and repulsion are calculated. This is done due to the computational power constraints. The convergence is guaranteed due to slowly decreasing attraction and repulsion forces.

The UMAP was configured with a cosine distance, 70 minimum neighbours, and a minimum distance of 0.3. As a result, a 2D embedding of features was acquired; the X and Y axes were denoted as U1 and U2. To enable the transformation of external data into the UMAP space, a fully connected neural network was designed for regression. PCA components were input to the model, and two resulting UMAP dimensions were the desired output. Various network configurations were tested, including 2 to 6 layers, layer sizes ranging from 200 to 20 neurons, and learning rates between 10^{-3} and 10^{-6}. The training was performed using 5-fold cross-validation, and the best network was chosen based on its R^2 value, as defined in Eq. 8.13.

$$R^2 = \frac{\sum_{i=0}^{M}(y_{true_i} - y_{pred_i})^2}{\sum_{i=0}^{M}(y_{true_i} - \overline{y}_{true})^2} \tag{8.13}$$

8.3.5 Features significance

To measure the features' significance in the UMAP creation process, the SHAP values were used. Another neural network model was trained; the input to the network was the set of standardised features, while the output was the U1 and U2 values of the UMAP embedding. The neural network contained 5 dense layers with an ELU activation function [233] and 2 dropout layers with a 0.3 rate in between dense layers. The number of neurons ranged from 200 to 50 in the network's backbone and 2 at the input. The Adam optimiser was used with a learning rate of 0.001 and for the loss function, mean absolute error was selected. The network was trained for 100 epochs.

SHAP values are based on game theory and are used to explain feature significance in model prediction. The features F are analysed one by one on the feature subsets S where $S \subseteq F$. Two models are compared during the analysis of a single feature. The first model is trained on the feature space S, which does not contain the analysed feature i and is denoted f_S. The second model is trained on the subset $S \cup i$, which holds the analysed feature, and the model is denoted as $f_{S \cup i}$. The SHAP values are then calculated using Eq. 8.14.

$$\phi_i = \sum_{S \subseteq F \setminus \{i\}} \frac{|S|!(|F| - |S| - 1)!}{|F|!} \left(f(x_{S \cup \{i\}}) - f(x_S) \right) \tag{8.14}$$

The positive SHAP value means that the feature increases the prediction; the negative value means it decreases the prediction.

The SHAP values are then analysed in the U1 and U2 spaces. For the most influential features, the CT series were found that correspond to the extreme points. These were visualised and, if possible, voxel-based radiomic features were calculated. Unlike traditional region-based radiomics, which summarises features over an entire segmented region, voxel-based radiomics captures local heterogeneity and spatial variations by computing features for each voxel in its local neighbourhood.

8.4 Results

The feature set was preprocessed and inputted to the PCA method, from which components explaining 90 % of the variance were selected. This resulted in the 29 components, which were linear combinations of original features. UMAP created based on the PCA components is shown in Figure 8.1 as a density map with subplots showing the distribution of patients from each GOLD group. On each subfigure, clusters formed by a high concentration of points in one place were noted as C(GOLD)(cluster number left-right). For GOLD 0 patients, three clusters were formed (C00, C01, C02); for GOLD 1 patients, two clusters of similar size were formed (C10, C11); for GOLD 2 patients, two clusters were also formed (C20, C21), but of different sizes; for GOLD 3 (C30) and GOLD 4 (C40) patients, one cluster was formed.

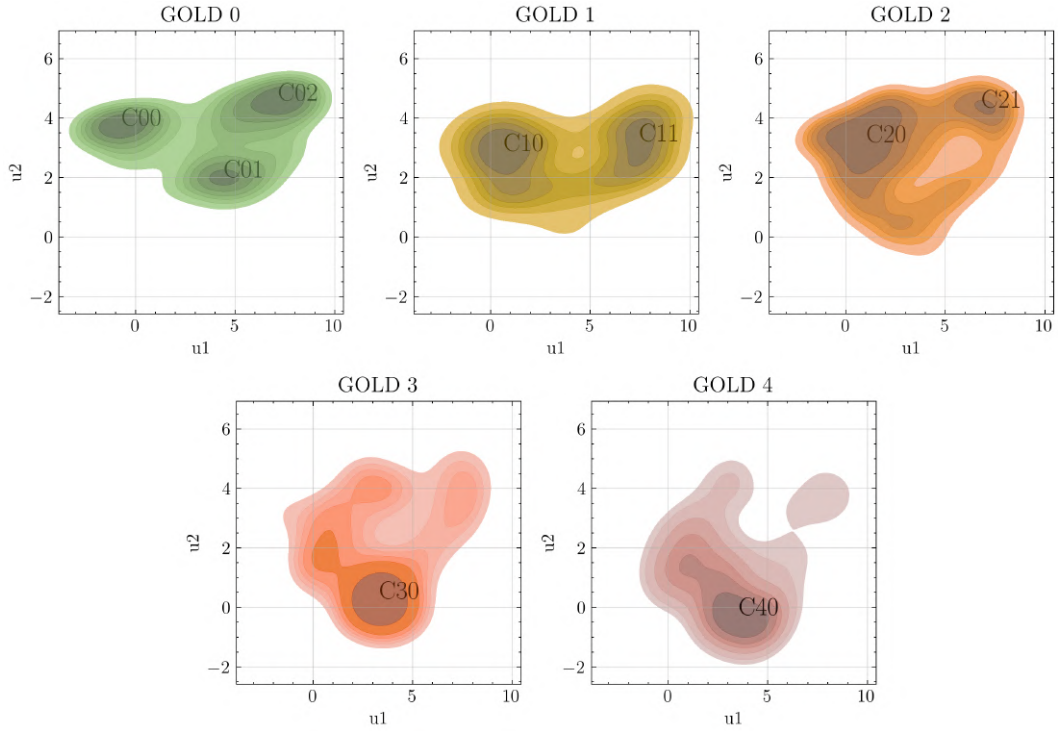

Figure 8.1: Density plots of resulting UMAP embedding shown on different subplots. For each GOLD group, areas of the largest densities have been found and named following the convention C(GOLD)(cluster number left-right).

There is a slight overlap with the placement of the clusters for GOLD groups 0, 1, and 2. Notably, the clusters C00 and C02 are positioned slightly higher than the clusters C10, C11, C20 and C21. Cluster C10 is positioned between C00 and C01, and cluster C11 is situated between C01 and C02. Cluster C20 overlaps with C10 but

seems to miss cluster C00 and C01. Cluster C21 is situated over cluster C11 and in the lower part of C02. Clusters for C30 and C40 are quite close, but the C40 cluster's largest density is visible below the C30 cluster. The number of clusters in the GOLD groups or their blurring suggests the non-homogeneity in the groups. However, the non-homogeneity is not due to the disease analysed but to differences between individual patients. It is noticeable that the clusters become more homogeneous with the increase of the GOLD value. Each cluster was be visualised and analysed to prove it.

The C00 cluster example image is shown in the second subplot of Figure 8.2. These changes are identified by low-attenuation values, around -982 HU. The abnormalities in the images are found near the lung border or close to blood vessels, which typically have higher density values. The thin alveoli walls can be seen on the presented scans, suggesting the scans' high resolution. The C01 example image is shown in the third subplot of Figure 8.2. This cluster includes patients with no noticeable changes and those with visible emphysematous alterations. It is characterised by a large volume of segmented areas, with density values around -910 HU. The segmented regions are not located near the lung borders; if adjacent to blood vessels, only a small portion of the segmentation area is in contact. The C02 example image is shown in the fourth subplot of Figure 8.2. Image series within these clusters have unusually high threshold values reaching approximately -788 HU. Despite this, the lungs are not fully outlined, suggesting either an issue with the scanning protocol or the presence of high-attenuation patterns. Some images in this cluster are of low quality, with noise reducing the visibility of alveolar edges. The lung segmentations extend to the edges of the chest, suggesting that contour features may play a significant role in this region of the UMAP embedding.

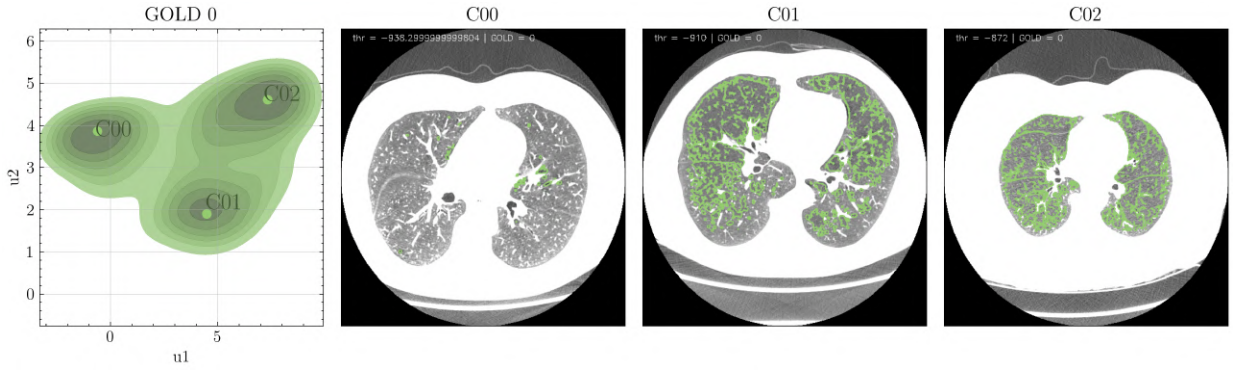

Figure 8.2: UMAP embedding density plot for GOLD 0 group with example images taken from the centre of each cluster.

The C10 example images are shown in the second subplot of Figure 8.3. The images included in this cluster have emphysematous lesions with little volume but a high degree of diffusion. The lesions are in contact with the lung walls and vessels more than once. The threshold values are not homogeneous, ranging from -900 to about -940, while the voxel values in the segmentations seem homogeneous. The C11 example image is shown in the third subplot of Figure 8.3. The threshold values in the cluster vary from -850 to -910 HU. The images contain a large volume of abnormal changes and a low degree of diffusion; changes are usually packed closely together. The segmented areas appear to be heterogeneous in terms of voxel HU values.

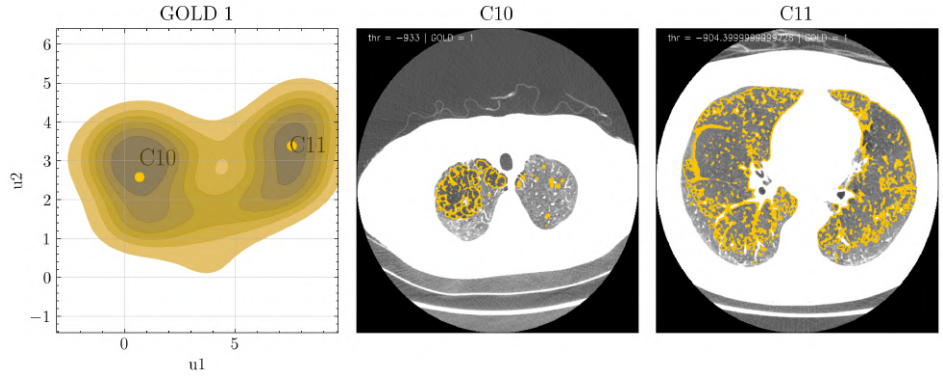

Figure 8.3: UMAP embedding density plot for GOLD 1 group with example images taken from the centre of each cluster.

The C20, a larger and more diffuse cluster example image, is shown in the second subplot of Figure 8.4. The cluster contains segmentations acquired with thresholds ranging from -915 to even -990. This high variation in threshold values results from the large area of the cluster. It contains images with moderate amounts of changes, raising in value while moving down on the y-axis in the embedding. It is characterised by high diffusion of changes and homogeneity of the voxel values. The C21, small cluster example image is shown in the third subplot of Figure 8.4. The images within the clusters have relatively high threshold values, which translates to their high volume. The HU values in the segmentations are heterogeneous. Segmentations are compact and tend to share a border with the lung's edges.

The C30 example image from a cluster with the highest density is shown in the second subplot of Figure 8.5. The images within the cluster have a large volume of emphysematous lesions. The distribution of the changes varies and does not present any pattern. The segmentation HU values overall are heterogeneous, but the segmentation

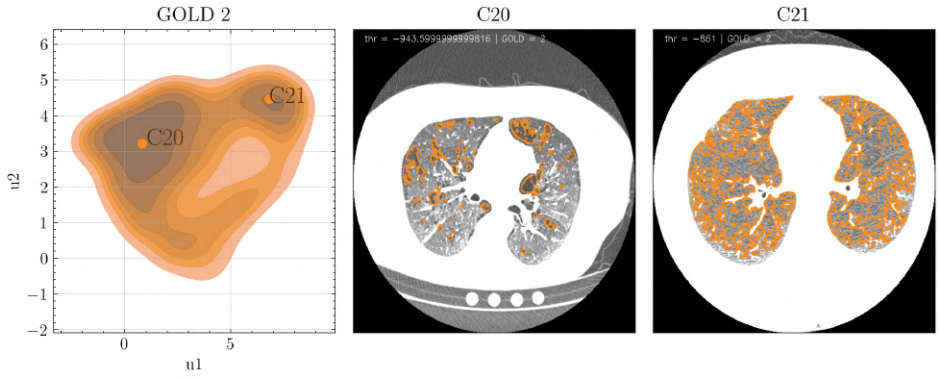

Figure 8.4: UMAP embedding density plot for GOLD 2 group with example images taken from the centre of each cluster.

surfaces show clear, larger patches of emphysematous lesions separated by thicker white lines.

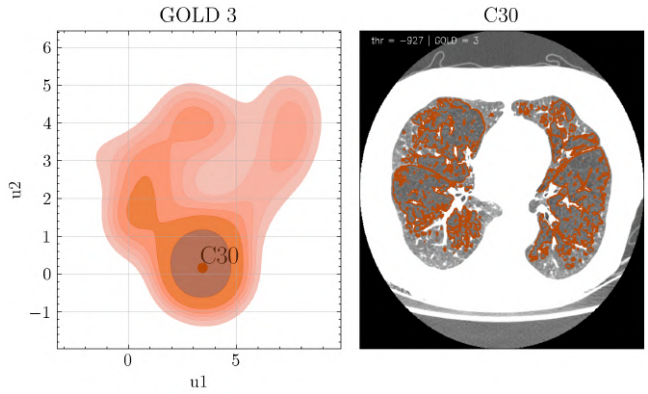

Figure 8.5: UMAP embedding density plot for GOLD 3 group with example image taken from the centre of the cluster.

The C40 main cluster example image is shown in the second subplot of Figure 8.6. The images are characterised by widespread, large homogeneous patches of emphysematous changes resulting from the destruction of alveoli walls. The segmented regions sometimes share borders with the vessels and lung walls or are separated by fissures or reticulations.

A visual analysis of the UMAP embedding content presents a diagram of the nature of the segmentation. At the top left, images with not much segmentation area, whose grey level intensity values are homogeneous, are arranged. The further to the right, the more changes, at first characterised by strong dispersion, but tending towards more homogeneous areas. To the right, the character of the changes is much more

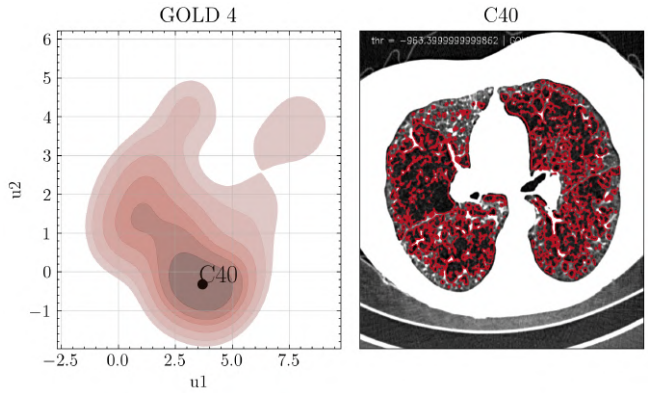

Figure 8.6: UMAP embedding density plot for GOLD 4 group with example image taken from the centre of the cluster.

heterogeneous in terms of segmentation grey levels. There are also areas bordered by lung walls. Moving slowly downwards from this point, the segmentations move away from the lung walls. The lower one goes, the UMAP narrows more and more, at first presenting progressively more homogeneous areas, at the same time locating images with less and more scattered segmentation on the left and right. Finally, at the very bottom of the UMAP embedding, the segmentations show large patches of homogeneous regions, suggesting large destruction of alveoli walls.

To further understand the features with the most influence on UMAP embedding, a detailed backward feature analysis was conducted. The most influential features were distinguished by calculating SHAP values based on the trained neural network model. The absolute mean of SHAP values for both UMAP dimensions was plotted and shown in Figure 8.7.

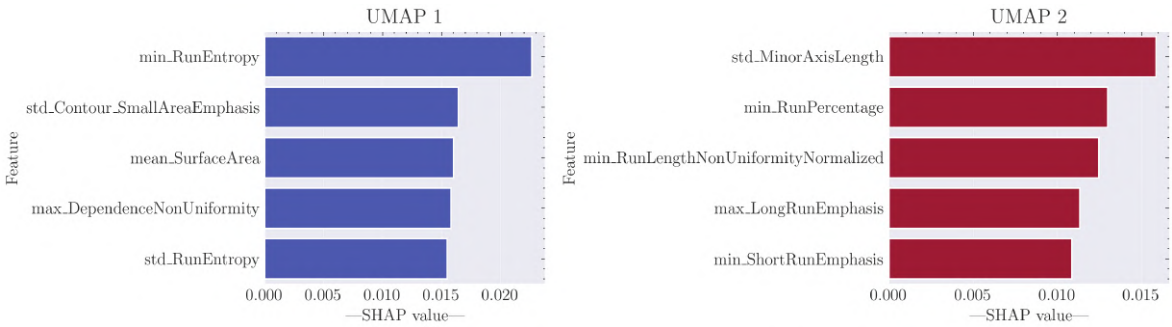

Figure 8.7: SHAP median values of features across samples showing features' impact on the UMAP 1 (U1) and UMAP 2 (U2) axis.

The minimum of run entropy feature is the most significant feature in the U1

(X) axis, and the standard deviation of minor axis length is most significant in the U2 (Y) axis. Other features have their SHAP values distributed evenly.

8.5 Discussion

In this section, the effect of features on the UMAP embedding will be discussed. The UMAPs with the example slices from the CT series with low and high feature values will be shown. Additionally, the voxel-based radiomic features were calculated from the given volumes and shown under each slice. It is important to note that each low-attenuation pattern segmentation resulting from the method presented in this dissertation was split into ROIs with respect to the lung lobes. The radiomic features were calculated per ROI and then summarised using a difference aggregation function.

8.5.1 UMAP 1

The minimum of Run Entropy is the most influential feature in U1; it is a texture feature derived from the Grey Level Run Length Matrix (GLRLM). It measures the randomness in the distribution of run lengths for different intensity levels in an image. A higher Run Entropy indicates a more complex texture with varied run lengths, while a lower Run Entropy suggests a more uniform or structured pattern. The example series with high and low run entropy features are shown in Figure 8.8. In the series with GOLD 0 and 1, emphysema was present in small, uniform regions. If the algorithm did not indicate emphysema, then the mask was occupied by an area of the lung which was not uniform. Hence, it is presumed that the minimum run entropy feature differentiates between emphysematous and non-emphysematous cases of patients with low GOLD values.

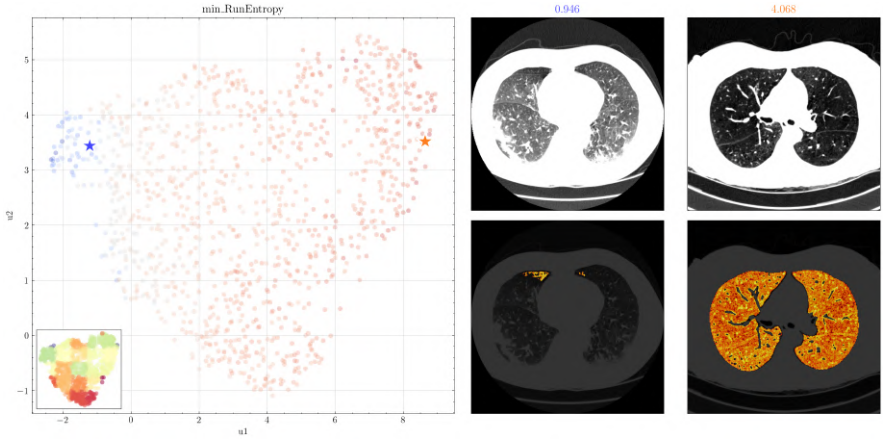

Figure 8.8: Minimum of Run Entropy distribution across the UMAP embedding (reference GOLD distribution in bottom-left corner). Example images with low and high feature values with their voxel-based feature heatmaps.

The Run Entropy feature can be seen for the second time on the significance chart. The standard deviation of the Run entropy is the fifth most significant feature. Even though the feature origin is the same, the difference between its minimum (Figure 8.8) and standard deviation (Figure 8.9) is apparent. The gradient of feature changes has been reversed, but the overall trend persists.

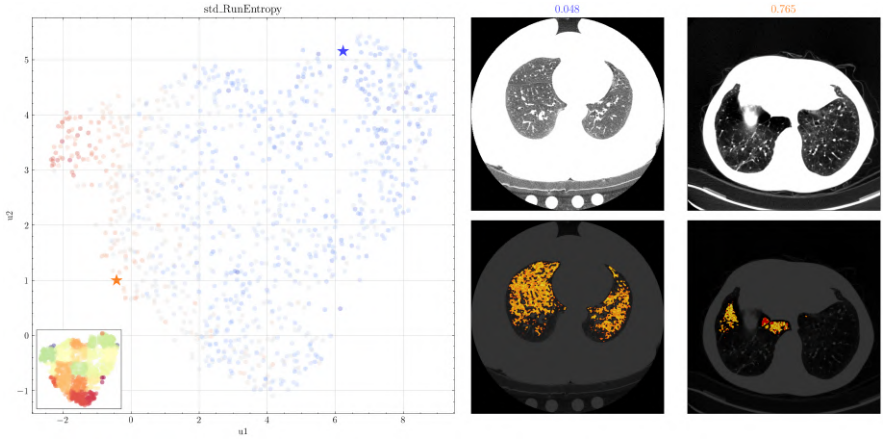

Figure 8.9: Standard deviation of Run Entropy distribution across the UMAP embedding (reference GOLD distribution in bottom-left corner). Example images with low and high feature values with their voxel-based feature heatmaps.

The standard deviation of contour Small Area Emphasis is the second most influential feature in U1; contour features were derived based on the outer surface of the ROIs. The Small Area Emphasis is a texture feature calculated from the Grey Level Size Zone

Matrix (GLSZM). It quantifies the distribution of small homogeneous zones (clusters of connected voxels with the same intensity). A high value means that the image has many small uniform regions. A low-value image has larger non-uniform regions. Since the standard deviation was used to aggregate the Small Area Emphasis, a higher value indicates greater variation in contour size and texture, while a lower value suggests less variation. The high variation of the contour values and sizes usually appears when the emphysematous lesion is found in the central areas of the lung parenchyma. The low variation of the contour values and sizes appears when the mask is located on the lung borders. This can be seen on the example images in Figure 8.10.

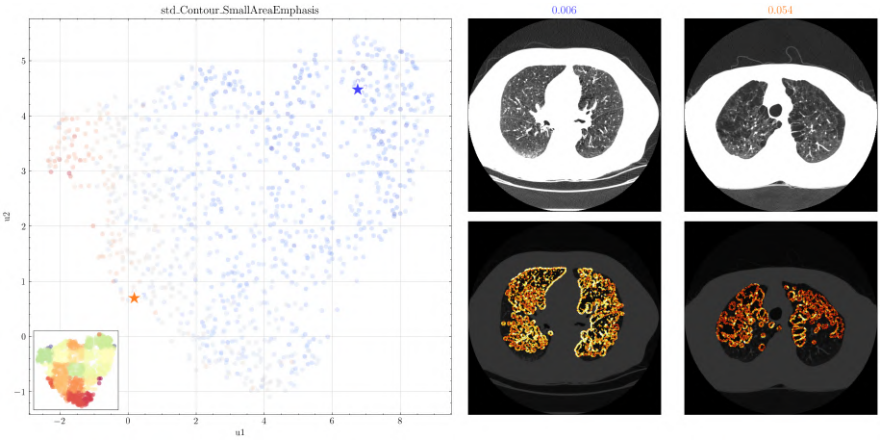

Figure 8.10: Standard deviation of Contours' Small Area Emphasis distribution across the UMAP embedding (reference GOLD distribution in bottom-left corner). Example images with low and high feature values with their voxel-based feature heatmaps.

The mean Surface Area is the third most influential feature in U1; it is a shape-based feature and refers to the total outer surface of a 3D ROI. It represents the sum of all the areas of the individual faces that make up the 3D object's boundary. Its average value directly indicates the size of the segmented masks. The example series with high and low mean surface area features are shown in Figure 8.11.

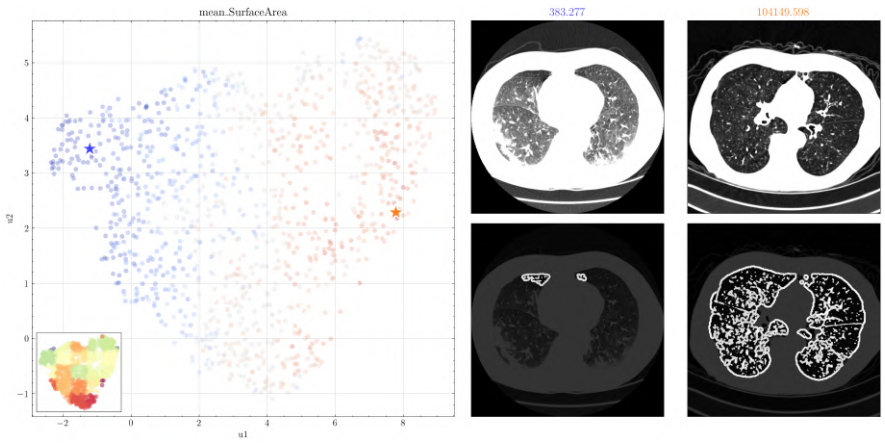

Figure 8.11: Mean of ROIs' Surface Area distribution across the UMAP embedding (reference GOLD distribution in bottom-left corner). Example images with low and high feature values, with and without overlaid segmentations' contours.

8.5.2 UMAP 2

The standard deviation of Minor Axis Length is the most influential feature in U2; it is a shape-based feature that represents the shortest axis of the best-fitting ellipse (or ellipsoid in 3D) that encloses the segmented region of interest (ROI). The feature calculation is done separately for several ROIs determined by grouping neighbouring areas within lobes. A large std Minor Axis Length value means many emphysematous lesions, most likely scattered throughout the lung area, of different sizes. The low value of std Minor Axis Length indicates that either there are not that many ROIs in the lung volume or the ROIs are similarly sized. The example series slices with a high and low standard deviation of Minor Axis Length are shown in Figure 8.12.

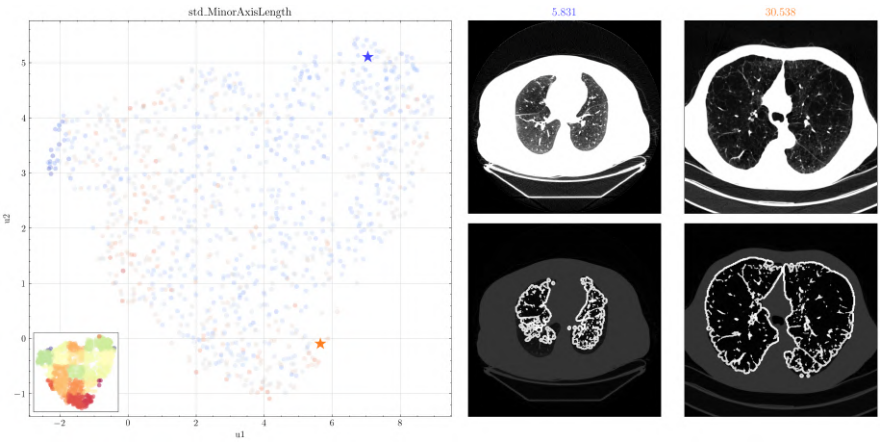

Figure 8.12: Standard deviation of Minor Axis Length distribution across the UMAP embedding (reference GOLD distribution in bottom-left corner). Example images with low and high feature values, with and without overlaid segmentations' contours.

The minimum of Run Percentage has the second most influence on U2; it is a texture feature derived from the Grey Level Run Length Matrix (GLRLM). It quantifies the density of homogeneous runs (consecutive voxels with the same grey level) in an image. This means that when the value is high, there is more transition between grey levels in the ROI. A low value indicates that there are fewer transitions between grey level regions; the regions are more homogeneous. Higher homogeneity of regions is typical in emphysematous lesions. The example series and their slices are shown in Figure 8.13.

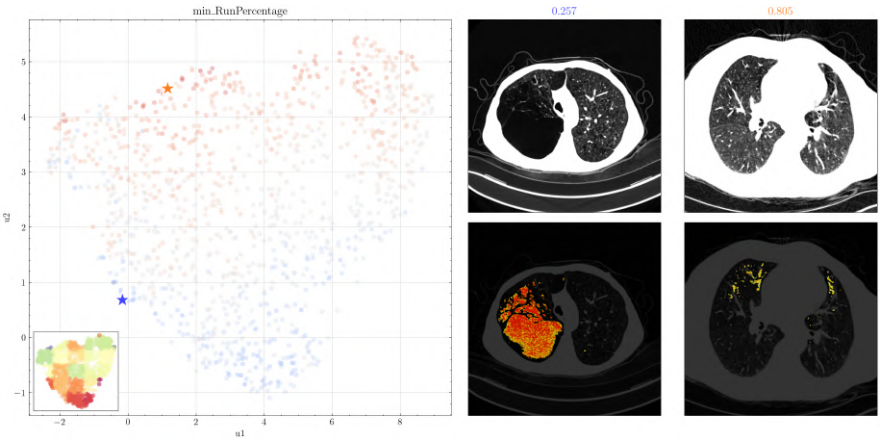

Figure 8.13: Minimum of Run Percentage distribution across the UMAP embedding (reference GOLD distribution in bottom-left corner). Example images with low and high feature values with their voxel-based feature heatmaps.

The minimum of Run Length Non-Uniformity Normalised is the third most influ-

ential feature in U2; it is a texture feature derived from the grey Level Run Length Matrix. It quantifies the variation in run lengths across the image. A high feature value means that the run lengths are uniformly distributed. A low feature value means that some run lengths dominate over others, making the texture less uniform. In the case of the emphysematous lesion, the domination of low attenuation is prevalent as shown in Figure 8.14.

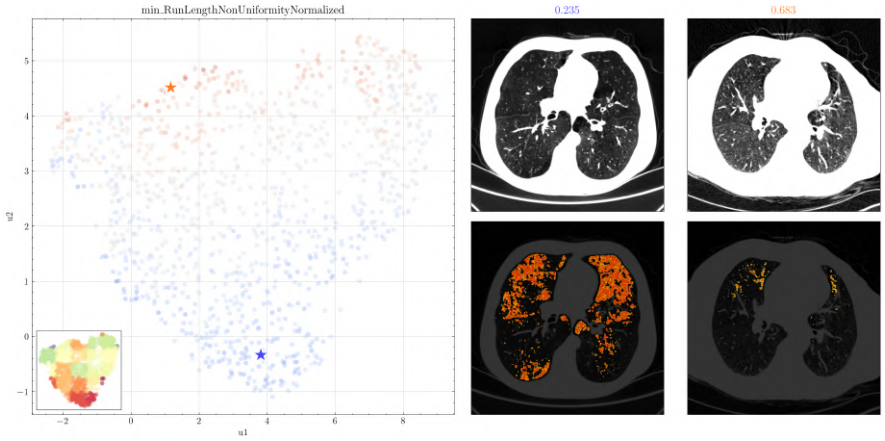

Figure 8.14: Minimum of Run Length Non-Uniformity Normalised distribution across the UMAP embedding (reference GOLD distribution in bottom-left corner). Example images with low and high feature values with their voxel-based feature heatmaps.

Both the maximum of Long Run Emphasis (LRE) and the minimum of Short Run Emphasis (SRE) are important features for U2; they are texture features derived from the Grey Level Run Length Matrix (GLRLM). They describe the distribution of run lengths in an image. Long Run Emphasis high values mean more homogeneous texture and low values mean less homogeneous texture. Similarly, Short Run Emphasis high values mean less homogeneous texture and low values mean more homogeneous texture. The emphysematous regions are homogeneous, so the LRE were aggregated by maximum (indicating homogeneity) and SRE were aggregated by minimum (indicating homogeneity). It might appear that they carry the same information; information is indeed similar, yet the subject of analysis is different. One analyses structure in a larger, global context and the other in a smaller, local context, supplementing each other. The example series slices are presented for LRE in Figure 8.15 and SRE in Figure 8.16.

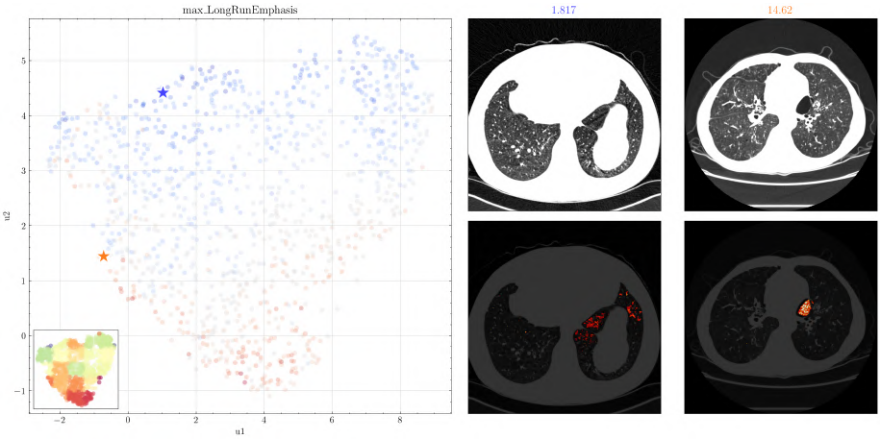

Figure 8.15: Maximum of Long Run Emphasis (LRE) distribution across the UMAP embedding (reference GOLD distribution in bottom-left corner). Example images with low and high feature values with their voxel-based feature heatmaps.

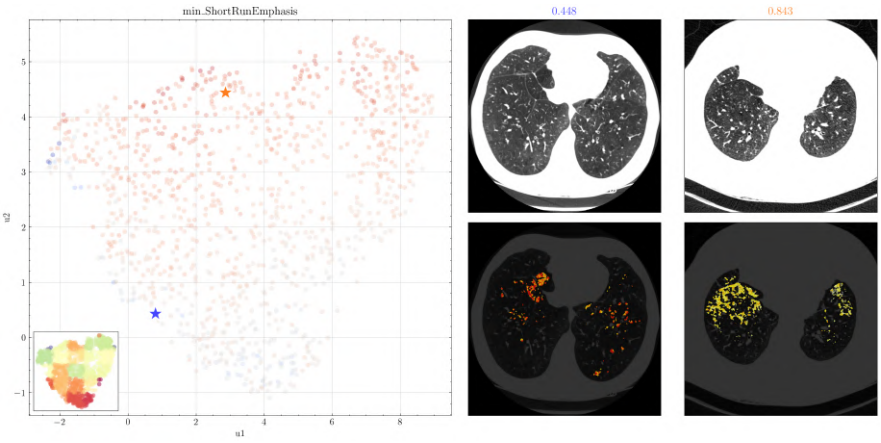

Figure 8.16: Minimum of Short Run Emphasis (SRE) distribution across the UMAP embedding (reference GOLD distribution in bottom-left corner). Example images with low and high feature values with their voxel-based feature heatmaps.

8.5.3 UMAP features significance conclusion

The first UMAP component UMAP 1 (U1), seems to indirectly cover the location and size of the ROIs while also partly covering the extent of low grey level zones (emphysema). Run Entropy differentiates patients based on the randomness of values in the ROI. The bigger the ROI and the less it contains emphysema, the larger the randomness is, covering two important aspects: the presence of emphysema and its extent. The standard deviation of the contour's Small Area Emphasis indicates whether the ROI is located near the lung border, also covering its extent. If it is a small ROI near the lung border but has a small volume, the calculated feature has a high std; if it is near the lung border but has a high volume, it reaches the fissure, resulting in a smaller std. The mean Surface Area directly informs about the extent of changes.

The second UMAP component UMAP 2 (U2), seems to cover the extent and intensity of the low grey level zones (emphysema) in ROIs. Minor Axis Length informs about the extent of ROIs; its std value informs how many different ROIs the segmentation contains. The emphysematous changes, if prevalent over the whole lung volume, are heterogeneous, which is identified by this feature. Run Percentage directly informs about ROIs' homogeneity, where large emphysematous regions are highly homogeneous. The Run Length Non-Uniformity Normalised is also a measure informing about ROIs' homogeneity. The goal of both Long Run Emphasis (LRE) and Short Run Emphasis (SRE), as explained in this context, is also to measure homogeneity in local and global contexts.

Chapter 9

Summary

Works done in the scope of the doctoral dissertation aimed to demonstrate the potential of unsupervised methods in the low-attenuation lesion detection on the chest Computed Tomography (CT) images. The created algorithm was mainly based on the COPDGene database, consisting of 2243 unique patients and their GOLD classifications indicating the severity of respiratory impairment. The dataset consists of images taken with different scanners, parameters, and reconstruction kernels. Of the available series, the focus was on images with a standard reconstruction kernel guaranteeing the least amount of noise, but including images from different scanners and with different layer thicknesses in the analysis.

Accurate delineation of emphysematous lesions is a challenge. They are heterogeneous in shape and distribution. There is no set with enough manually labelled emphysematous areas to use neural networks to segment them. In medical practice, thresholding based on a single cut-off threshold is used. However, as the literature review has shown, no universal threshold guarantees ideal segmentation. Following that, the automatic thresholding method was proposed based on a single CT.

Segmentation of emphysema using a fixed-threshold method has yet another limitation; the bronchial tree has a similar range of Hounsfield units (HU), which makes it appear along with emphysema on the resulting segmentation. To overcome this issue, a new method has been developed to generate the patient's airway mask. This method utilises two velocity maps to iteratively extend airway branches into the lung parenchyma. Additionally, bronchial wall structures help validate the segmentation. A technique for detecting segmentation errors has also been introduced, allowing the

identification and removal of both under-segmented and over-segmented airways. As the lesion segmentation algorithm assumes an adaptive cut-off threshold for the lung image, the proposed bronchial segmentation method effectively reduces the number of false positives by restricting the area with similar HU values to emphysematous lesions.

The proposed method for automatic lesion segmentation was based on Gaussian mixtures. The per-slice approach ensures the sensitivity of the method to small lesions appearing in the lung parenchyma. Two methods were compared, clustering the components of the mixtures and clustering the cut-off thresholds determined from the mixtures. Both methods could separate damaged alveoli from healthy alveoli, but the first method was chosen for further analysis. The method showed a clearer trend of emphysema volume and greater differences in the mean HU values of the segmentation. Thus, presenting a viable substitute for deep learning in the identification of emphysematous lesions on the chest CT images of patients.

To quantify this, a method was introduced that generates a UMAP embedding to capture relationships derived from patients' emphysematous lesion features. Common radiomic features, contour features, and positional features were analysed. Radiomic and contour features showed the ability to extract characteristic subgroups of changes in the UMAP embedding space. In particular, features relating to the size of the changes, their neighbouring grey levels, and changes in grey levels stood out. The created embedding was confronted with the GOLD classification of the images. UMAP embedding creates clearly defined clusters for each of the GOLD subgroups, showing a quantitative and qualitative relationship between GOLD groups and segmented regions.

The premise of the project was to explore the potential of unsupervised classical machine learning and image processing methods for the segmentation and quantification of emphysematous lesions. Both airway and lesion segmentation can be performed in an unsupervised manner by using mechanisms known to medics that characterise the structures. Only when it comes to lung segmentation is the use of deep learning techniques recommended. This guarantees working with an accurate image of the lungs without missing any structure. The methods presented allow easy interpretation of the results and traceability of the decision-making process. The created graphical interpretation of the results in the form of 2D embedding allows differential diagnosis and potential analysis of disease progression.

Bibliography

[1] D. Adeloye et al. "Global, regional, and national prevalence of, and risk factors for, chronic obstructive pulmonary disease (COPD) in 2019: a systematic review and modelling analysis". In: *The Lancet Respiratory Medicine* 10.5 (2022), pp. 447–458. ISSN: 2213-2600. DOI: 10.1016/S2213-2600(21)00511-7.

[2] B. Lundback et al. "Not 15 But 50 of smokers develop COPD?—Report from the Obstructive Lung Disease in Northern Sweden Studies". In: *Respiratory Medicine* 97.2 (Feb. 2003), pp. 115–122. ISSN: 0954-6111. DOI: 10.1053/rmed.2003.1446.

[3] S. S. Salvi and P. J. Barnes. "Chronic obstructive pulmonary disease in non-smokers". In: *The Lancet* 374.9691 (Aug. 2009), pp. 733–743. ISSN: 0140-6736. DOI: 10.1016/S0140-6736(09)61303-9.

[4] I. A. Yang, C. R. Jenkins, and S. S. Salvi. "Chronic obstructive pulmonary disease in never-smokers: risk factors, pathogenesis, and implications for prevention and treatment". In: *The Lancet Respiratory Medicine* 10.5 (May 2022), pp. 497–511. ISSN: 2213-2600. DOI: 10.1016/s2213-2600(21)00506-3.

[5] G. Shaddick et al. "Half the world's population are exposed to increasing air pollution". In: *npj Climate and Atmospheric Science* 3.1 (June 2020). ISSN: 2397-3722. DOI: 10.1038/s41612-020-0124-2.

[6] R. Rombach et al. *High-Resolution Image Synthesis with Latent Diffusion Models*. 2021. arXiv: 2112.10752 [cs.CV].

[7] F. Tomasi et al. "Automatic Music Playlist Generation via Simulation-based Reinforcement Learning". In: *Proceedings of the 29th ACM SIGKDD Conference on Knowledge Discovery and Data Mining*. KDD '23. Long Beach, CA, USA: Association for Computing Machinery, 2023, pp. 4948–4957. ISBN: 9798400701030. DOI: 10.1145/3580305.3599777.

[8] M. De Nadai et al. "Personalized Audiobook Recommendations at Spotify Through Graph Neural Networks". In: *Companion Proceedings of the ACM Web Conference 2024*. WWW '24. Singapore, Singapore: Association for Computing Machinery, 2024, pp. 403–412. ISBN: 9798400701726. DOI: 10.1145/3589335.3648339.

[9] E. Kasneci et al. "ChatGPT for good? On opportunities and challenges of large language models for education". In: *Learning and Individual Differences* 103 (2023). DOI: 10.1016/j.lindif.2023.102274.

[10] G. Rosenbusch and A. de Knecht-van Eekelen. *Wilhelm Conrad Röntgen: The Birth of Radiology*. Springer International Publishing, 2019. ISBN: 9783319976617. DOI: 10.1007/978-3-319-97661-7.

[11] SIEMENS. *Siemens Healthineers SOMATOM Force CT*. Accessed: 2024-08-29. URL: https://www.siemens-healthineers.com/pl/computed-tomography/dual-source-ct/somatom-force.

[12] D. Y. F. Chung et al. "Computed tomography". In: *Emergency Cross-sectional Radiology*. Cambridge University Press, 2012, pp. 1–7.

[13] G. N. Hounsfield. "Computed medical imaging". en. In: *Journal of Computer Assisted Tomography* 4.5 (Oct. 1980), pp. 665–674.

[14] N. Birur et al. "Comparison of gray values of cone-beam computed tomography with hounsfield units of multislice computed tomography: An in vitro study". en. In: *Indian J. Dent. Res.* 28.1 (2017), p. 66.

[15] V. M. Runge and J. T. Heverhagen. "Image Resolution: Pixel and Voxel Size". In: *The Physics of Clinical MR Taught Through Images*. Cham: Springer International Publishing, 2022, pp. 34–35. ISBN: 978-3-030-85413-3. DOI: 10.1007/978-3-030-85413-3_13.

[16] H. D. Nagel. "CT Parameters that Influence the Radiation Dose". In: *Radiation Dose from Adult and Pediatric Multidetector Computed Tomography*. Ed. by D. Tack and P. A. Gevenois. Berlin, Heidelberg: Springer Berlin Heidelberg, 2007, pp. 51–79. ISBN: 978-3-540-68575-3. DOI: 10.1007/978-3-540-68575-3_4.

[17] A. Midya et al. "Influence of CT acquisition and reconstruction parameters on radiomic feature reproducibility". In: *Journal of Medical Imaging* 5.01 (Feb. 2018), p. 1. DOI: 10.1117/1.jmi.5.1.011020.

[18] I. H. Shon et al. "Influence of X-ray computed tomography (CT) exposure and reconstruction parameters on positron emission tomography (PET) quantitation". In: *EJNMMI Physics* 7.1 (Oct. 2020). DOI: 10.1186/s40658-020-00331-w.

[19] S. P. Raman et al. "CT Scan Parameters and Radiation Dose: Practical Advice for Radiologists". In: *Journal of the American College of Radiology* 10.11 (2013), pp. 840–846. ISSN: 1546-1440. DOI: 10.1016/j.jacr.2013.05.032.

[20] C.-C. Yang. "Evaluation of Impact of Factors Affecting CT Radiation Dose for Optimizing Patient Dose Levels". In: *Diagnostics* 10.10 (Oct. 2020), p. 787. ISSN: 2075-4418. DOI: 10.3390/diagnostics10100787.

[21] S. Elojeimy, S. Tipnis, and W. Huda. "Relationship between radiographic techniques (kilovolt and milliampere-second) and CTDIVOL". In: *Radiation Protection Dosimetry* 141.1 (Apr. 2010), pp. 43–49. ISSN: 1742-3406. DOI: 10.1093/rpd/ncq138.

[22] P. Nagpal et al. "Factors Affecting Radiation Dose in Computed Tomography Angiograms for Pulmonary Embolism: A Retrospective Cohort Study". In: *Journal of Clinical Imaging Science* 10 (Nov. 2020), p. 74. ISSN: 2156-7514. DOI: 10.25259/jcis_168_2020.

[23] L. Yu et al. "Radiation dose reduction in computed tomography: techniques and future perspective". In: *Imaging in Medicine* 1.1 (Oct. 2009), pp. 65–84. ISSN: 1755-5205. DOI: 10.2217/iim.09.5.

[24] L. W. Goldman. "Principles of CT: Radiation Dose and Image Quality". In: *Journal of Nuclear Medicine Technology* 35.4 (2007), pp. 213–225. ISSN: 0091-4916. DOI: 10.2967/jnmt.106.037846.

[25] T. Clark. "Computed Tomography: Fundamentals, System Technology, Image Quality, Applications, 2nd Edition". In: *Biomedical Instrumentation and Technology* 41 (July 2007), pp. 278–278. DOI: 10.2345/0899-8205(2007)41[278:CTFSTI]2.0.CO;2.

[26] W. R. Webb, N. L. Müller, and D. P. Naidich. "Emphysema". In: *High-resolution CT of the lung*. Wolters Kluwer Heath, 2015. Chap. 2, pp. 264–273.

[27] J. T. Beck et al. "Artificial Intelligence Tool for Optimizing Eligibility Screening for Clinical Trials in a Large Community Cancer Center". In: *JCO Clinical Cancer Informatics* 4 (2020), pp. 50–59. DOI: 10.1200/CCI.19.00079.

[28] S. M. McKinney et al. "International evaluation of an AI system for breast cancer screening". In: *Nature* 577.7788 (Jan. 2020), pp. 89–94. ISSN: 1476-4687. DOI: 10.1038/s41586-019-1799-6.

[29] M. Gillooly and D. Lamb. "Airspace size in lungs of lifelong non-smokers: effect of age and sex." In: *Thorax* 48.1 (1993), pp. 39–43.

[30] K. Soejima et al. "Longitudinal Follow-up Study of Smoking-induced Lung Density Changes by High-resolution Computed Tomography". In: *American Journal of Respiratory and Critical Care Medicine* 161.4 (Apr. 2000), pp. 1264–1273. DOI: 10.1164/ajrccm.161.4.9905040.

[31] J. Stoller. "Murray and Nadel's Textbook of Respiratory Medicine, 6th Edition". In: *Annals of the American Thoracic Society* 12 (Aug. 2015), pp. 1257–8. DOI: 10.1513/AnnalsATS.201504-251OT.

[32] J. G. Betts. "The Lungs". In: *Anatomy and Physiology*. OpenStax College, Rice University, 2013. Chap. 22.2, pp. 1001–1003.

[33] J. E. Hall and A. C. Guyton. "Respiration". In: *Guyton and Hall Textbook of Medical Physiology*. Saunders, Elsevier, 2011. Chap. 37, p. 472.

[34] B. Suki, D. Stamenović, and R. Hubmayr. "Lung Parenchymal Mechanics". In: (July 2011), pp. 1317–1351. DOI: 10.1002/cphy.c100033.

[35] W. R. Webb, N. L. Müller, and D. P. Naidich. "The Lung Interstitium". In: *High-resolution CT of the lung*. Wolters Kluwer Heath, 2015. Chap. 2, pp. 72, 73.

[36] D. S. Zander and C. F. Farver. *Pulmonary Pathology*. Foundations in Diagnostic Pathology. London, England: Churchill Livingstone, July 2008.

[37] J. B. West. "Normal Physiology: Exercise". In: *Pulmonary Physiology and Pathophysiology: An integrated, case-based approach*. Second. Lippincott Williams amp; Wilkins, 2001, pp. 3–5.

[38] J. B. West. "Normal Physiology: Exercise". In: *Pulmonary Physiology and Pathophysiology: An integrated, case-based approach*. Second. Lippincott Williams and Wilkins, 2001, pp. 6–8.

[39] J. A. Verschakelen and W. De Wever. "Decreased Lung Attenuation". In: *Computed Tomography of the Lung: A Pattern Approach*. Berlin, Heidelberg: Springer Berlin Heidelberg, 2007, pp. 47–68. ISBN: 978-3-540-68260-8. DOI: 10.1007/978-3-540-68260-8_5.

[40] M. Sterclova et al. "Low Attenuation Patterns". In: *HRCT in Interstitial Lung Disease: Instructive Case Studies*. Ed. by E. Kocova. Cham: Springer International Publishing, 2019, pp. 47–85. ISBN: 978-3-030-16315-0. DOI: 10.1007/978-3-030-16315-0_6.

[41] J. L. Chai and E. F. Patz. "CT of the lung: patterns of calcification and other high-attenuation abnormalities." In: *American Journal of Roentgenology* 162.5 (1994). PMID: 8165982, pp. 1063–1066. DOI: 10.2214/ajr.162.5.8165982.

[42] E. Marchiori et al. "Diffuse High-Attenuation Pulmonary Abnormalities: A Pattern-Oriented Diagnostic Approach on High-Resolution CT". In: *American Journal of Roentgenology* 184.1 (2005). PMID: 15615988, pp. 273–282. DOI: 10.2214/ajr.184.1.01840273.

[43] J. A. Verschakelen and W. De Wever. "Decreased Lung Attenuation". In: *Computed Tomography of the Lung: A Pattern Approach*. Berlin, Heidelberg: Springer Berlin Heidelberg, 2007, pp. 47–68. ISBN: 978-3-540-68260-8. DOI: 10.1007/978-3-540-68260-8_5.

[44] W. R. Webb et al. "Normal and diseased isolated lungs: high-resolution CT." In: *Radiology* 166.1 (Jan. 1988), pp. 81–87. ISSN: 1527-1315. DOI: 10.1148/radiology.166.1.3336706.

[45] C. Sanders, P. H. Nath, and W. C. Bailey. "Detection of Emphysema with Computed Tomography: Correlation with Pulmonary Function Tests and Chest Radiography". In: *Investigative Radiology* 23.4 (Apr. 1988), pp. 262–266. ISSN: 0020-9996. DOI: 10.1097/00004424-198804000-00004.

[46] D. Steiger et al. "The importance of low-dose CT screening to identify emphysema in asymptomatic participants with and without a prior diagnosis of COPD". In: *Clinical Imaging* 78 (Oct. 2021), pp. 136–141. ISSN: 0899-7071. DOI: 10.1016/j.clinimag.2021.03.012.

[47] J. Fuhrman et al. "Evaluation of emphysema on thoracic low-dose CTs through attention-based multiple instance deep learning". In: *Scientific Reports* 13.1 (Jan. 2023). ISSN: 2045-2322. DOI: 10.1038/s41598-023-27549-9.

[48] S. N. J. Pipavath et al. "Chronic Obstructive Pulmonary Disease: Radiology-Pathology Correlation". In: *Journal of Thoracic Imaging* 24.3 (Aug. 2009), pp. 171–180. ISSN: 0883-5993. DOI: 10.1097/rti.0b013e3181b32676.

[49] G. F. *Emphysema (diagrams). Case study, Radiopaedia.org.* [Online; accessed May, 2024]. Mar. 2010. DOI: 10.53347/rID-9225.

[50] E. J. Stern et al. "Idiopathic giant bullous emphysema (vanishing lung syndrome): imaging findings in nine patients." In: *American Journal of Roentgenology* 162.2 (Feb. 1994), pp. 279–282. ISSN: 1546-3141. DOI: 10.2214/ajr.162.2.8310909.

[51] D. M. Hansell et al. "Fleischner Society: Glossary of Terms for Thoracic Imaging". In: *Radiology* 246.3 (Mar. 2008), pp. 697–722. ISSN: 1527-1315. DOI: 10.1148/radiol.2462070712.

[52] D. L. *Subpleural bullae. Case study, Radiopaedia.org.* [Online; accessed May, 2024]. Dec. 2009. DOI: 10.53347/rID-7959.

[53] D. D. *Bronchial atresia. Case study, Radiopaedia.org.* [Online; accessed May, 2024]. Jan. 2010. DOI: 10.53347/rID-8279.

[54] J. Hoidal. "Genetics of COPD: present and future". In: *European Respiratory Journal* 18.5 (2001), pp. 741–743. URL: http://erj.ersjournals.com/content/erj/18/5/741.

[55] T. R. BAI and D. A. KNIGHT. "Structural changes in the airways in asthma: observations and consequences". In: *Clinical Science* 108.6 (May 2005), pp. 463–477. ISSN: 1470-8736. DOI: 10.1042/cs20040342.

[56] P. J. Barnes. "Mediators of Chronic Obstructive Pulmonary Disease". In: *Pharmacological Reviews* 56.4 (Dec. 2004), pp. 515–548. ISSN: 1521-0081. DOI: 10.1124/pr.56.4.2.

[57] P. J. Barnes, K. F. Chung, and C. P. Page. "Inflammatory mediators of asthma: an update". en. In: *Pharmacol Rev* 50.4 (Dec. 1998), pp. 515–596.

[58] J. Majo, H. Ghezzo, and M. Cosio. "Lymphocyte population and apoptosis in the lungs of smokers and their relation to emphysema". In: *European Respiratory Journal* 17.5 (May 2001), pp. 946–953. ISSN: 1399-3003. DOI: 10.1183/09031936.01.17509460.

[59] L. Taraseviciene-Stewart et al. "Is Alveolar Destruction and Emphysema in Chronic Obstructive Pulmonary Disease an Immune Disease?" In: *Proceedings of the American Thoracic Society* 3.8 (Nov. 2006), pp. 687–690. ISSN: 1546-3222. DOI: 10.1513/pats.200605-105sf.

[60] R. M. Tuder. "State of the Art. Cellular and Molecular Mechanisms of Alveolar Destruction in Emphysema: An Evolutionary Perspective". In: *Proceedings of the American Thoracic Society* 3.6 (Aug. 2006), pp. 503–510. ISSN: 1546-3222. DOI: 10.1513/pats.200603-054ms.

[61] M. G. Cosio, M. Saetta, and A. Agusti. "Immunologic Aspects of Chronic Obstructive Pulmonary Disease". In: *New England Journal of Medicine* 360.23 (June 2009), pp. 2445–2454. ISSN: 1533-4406. DOI: 10.1056/nejmra0804752.

[62] P. J. Barnes. "Immunology of asthma and chronic obstructive pulmonary disease". In: *Nature Reviews Immunology* 8.3 (Feb. 2008), pp. 183–192. ISSN: 1474-1741. DOI: 10.1038/nri2254.

[63] J. F. Donohue. "Therapeutic Responses in Asthma and COPD: Bronchodilators". In: *Chest* 126.2, Supplement (2004), 125S–137S. ISSN: 0012-3692. DOI: 10.1378/chest.126.2_suppl_1.125S.

[64] H. A. Kerstjens et al. "A Comparison of Bronchodilator Therapy with or without Inhaled Corticosteroid Therapy for Obstructive Airways Disease". In: *New England Journal of Medicine* 327.20 (1992), pp. 1413–1419. DOI: 10.1056/NEJM199211123272003.

[65] A. Agustí et al. "Global Initiative for Chronic Obstructive Lung Disease 2023 Report: GOLD Executive Summary". In: *American Journal of Respiratory and Critical Care Medicine* 207.7 (Apr. 2023), pp. 819–837. ISSN: 1535-4970. DOI: 10.1164/rccm.202301-0106pp.

[66] P. W. Jones et al. "Development and first validation of the COPD Assessment Test". In: *European Respiratory Journal* 34.3 (Aug. 2009), pp. 648–654. ISSN: 1399-3003. DOI: 10.1183/09031936.00102509.

[67] J. C. Bestall et al. "Usefulness of the Medical Research Council (MRC) dyspnoea scale as a measure of disability in patients with chronic obstructive pulmonary disease". In: *Thorax* 54.7 (July 1999), pp. 581–586. ISSN: 0040-6376. DOI: 10.1136/thx.54.7.581.

[68] M. S. Dunnill. "Quantitative Methods in the Study of Pulmonary Pathology". In: *Thorax* 17.4 (1962), pp. 320–328. ISSN: 0040-6376. DOI: 10.1136/thx.17.4.320.

[69] W. M. Thurlbeck et al. "A comparison of three methods of measuring emphysema". In: *Human Pathology* 1.2 (June 1970), pp. 215–226. ISSN: 0046-8177. DOI: 10.1016/s0046-8177(70)80035-1.

[70] R. C. Ryder, W. M. Thurlbeck, and J. Gough. "A Study of Interobserver Variation in the Assessment of the Amount of Pulmonary Emphysema in Paper-Mounted Whole Lung Sections". In: *American Review of Respiratory Disease* 99.3 (1969). PMID: 5765627, pp. 354–364. DOI: 10.1164/arrd.1969.99.3.354.

[71] P. Turner and W. F. Whimster. "Volume of emphysema." In: *Thorax* 36.12 (1981), pp. 932–937. ISSN: 0040-6376. DOI: 10.1136/thx.36.12.932.

[72] A. Madani, C. Keyzer, and P. Gevenois. "Quantitative computed tomography assessment of lung structure and function in pulmonary emphysema". In: *European Respiratory Journal* 18.4 (2001), pp. 720–730. ISSN: 0903-1936. DOI: 10.1183/09031936.01.00255701.

[73] M. Saetta et al. "Destructive Index: A Measurement of Lung Parenchymal Destruction in Smokers". In: *American Review of Respiratory Disease* 131.5 (1985). PMID: 4003921, pp. 764–769. DOI: 10.1164/arrd.1985.131.5.764.

[74] M. Mishima et al. "Complexity of terminal airspace geometry assessed by lung computed tomography in normal subjects and patients with chronic obstructive pulmonary disease". In: *Proceedings of the National Academy of Sciences* 96.16 (1999), pp. 8829–8834. DOI: 10.1073/pnas.96.16.8829.

[75] N. Tanabe et al. "Fractal analysis of low attenuation clusters on computed tomography in chronic obstructive pulmonary disease". In: *BMC Pulmonary Medicine* 18.1 (Aug. 2018). ISSN: 1471-2466. DOI: 10.1186/s12890-018-0714-5.

[76] M. Hayhurst et al. "Diagnosis of Pulmonary Emphysema by Computerised Tomography". In: *The Lancet* 324.8398 (Aug. 1984), pp. 320–322. ISSN: 0140-6736. DOI: 10.1016/s0140-6736(84)92689-8.

[77] N. L. Müller et al. ""Density Mask"". In: *Chest* 94.4 (Oct. 1988), pp. 782–787. ISSN: 0012-3692. DOI: 10.1378/chest.94.4.782.

[78] P. A. Gevenois et al. "Comparison of computed density and macroscopic morphometry in pulmonary emphysema." In: *American Journal of Respiratory and Critical Care Medicine* 152.2 (Aug. 1995), pp. 653–657. ISSN: 1535-4970. DOI: 10.1164/ajrccm.152.2.7633722.

[79] A. Madani et al. "Pulmonary Emphysema: Objective Quantification at Multi–Detector Row CT—Comparison with Macroscopic and Microscopic Morphometry". In: *Radiology* 238.3 (2006). PMID: 16424242, pp. 1036–1043. DOI: 10.1148/radiol.2382042196.

[80] A. A. Bankier et al. "Pulmonary Emphysema: Subjective Visual Grading versus Objective Quantification with Macroscopic Morphometry and Thin-Section CT Densitometry". In: *Radiology* 211.3 (June 1999), pp. 851–858. ISSN: 1527-1315. DOI: 10.1148/radiology.211.3.r99jn05851.

[81] K. Kishi et al. "The correlation of emphysema or airway obstruction with the risk of lung cancer: a matched case-controlled study". In: *European Respiratory Journal* 19.6 (2002), pp. 1093–1098. ISSN: 0903-1936. DOI: 10.1183/09031936.02.00264202.

[82] F. Maldonado et al. "Are Airflow Obstruction and Radiographic Evidence of Emphysema Risk Factors for Lung Cancer?: A Nested Case-Control Study Using Quantitative Emphysema Analysis". In: *Chest* 138.6 (2010), pp. 1295–1302. ISSN: 0012-3692. DOI: 10.1378/chest.09-2567.

[83] E. J. Stern and M. S. Frank. "CT of the lung in patients with pulmonary emphysema: diagnosis, quantification, and correlation with pathologic and physiologic findings." In: *American Journal of Roentgenology* 162.4 (Apr. 1994), pp. 791–798. ISSN: 1546-3141. DOI: 10.2214/ajr.162.4.8140992.

[84] A. Dirksen et al. "Progress of emphysema in severe alpha1-Antitrypsin Deficiency as Assessed by Annual CT". In: *Acta Radiologica* 38.5 (Sept. 1997), pp. 826–832. ISSN: 1600-0455. DOI: 10.1080/02841859709172418.

[85] A. Dirksen et al. "A Randomized Clinical Trial of alpha1-Antitrypsin Augmentation Therapy". In: *American Journal of Respiratory and Critical Care Medicine* 160.5 (Nov. 1999), pp. 1468–1472. ISSN: 1535-4970. DOI: 10.1164/ajrccm.160.5.9901055.

[86] E. A. Regan et al. "Genetic Epidemiology of COPD (COPDGene) Study Design". In: *COPD: Journal of Chronic Obstructive Pulmonary Disease* 7.1 (Mar. 2010), pp. 32–43. ISSN: 1541-2563. DOI: 10.3109/15412550903499522.

[87] W. Rzyman et al. "Results of an open-access lung cancer screening program with low-dose computed tomography: the Gdańsk experience". In: *Polish Archives*

of Internal Medicine 125.4 (Mar. 2015), pp. 232–239. ISSN: 1897-9483. DOI: 10.20452/pamw.2778.

[88] M. Ostrowski et al. "Ten years of experience in lung cancer screening in Gdańsk, Poland: a comparative study of the evaluation and surgical treatment of 14,200 participants of 2 lung cancer screening programmes". In: *Interactive CardioVascular and Thoracic Surgery* 29.2 (Mar. 2019), pp. 266–274. ISSN: 1569-9293. DOI: 10.1093/icvts/ivz079.

[89] D. R. Baldwin et al. "UK Lung Screen (UKLS) nodule management protocol: modelling of a single screen randomised controlled trial of low-dose CT screening for lung cancer". In: *Thorax* 66.4 (2011), pp. 308–313. ISSN: 0040-6376. DOI: 10.1136/thx.2010.152066.

[90] S. Hu, E. Hoffman, and J. Reinhardt. "Automatic lung segmentation for accurate quantitation of volumetric X-ray CT images". In: *IEEE transactions on medical imaging* 20 (July 2001), pp. 490–8. DOI: 10.1109/42.929615.

[91] A. Mansoor et al. "Segmentation and Image Analysis of Abnormal Lungs at CT: Current Approaches, Challenges, and Future Trends". In: *Radiographics: a review publication of the Radiological Society of North America, Inc* 35 (July 2015), pp. 1056–76. DOI: 10.1148/rg.2015140232.

[92] D. Carmo et al. "A Systematic Review of Automated Segmentation Methods and Public Datasets for the Lung and its Lobes and Findings on Computed Tomography Images". In: *Yearbook of Medical Informatics* 31.01 (Aug. 2022), pp. 277–295. DOI: 10.1055/s-0042-1742517.

[93] A. Mansoor et al. "Segmentation and image analysis of abnormal lungs at CT: Current approaches, challenges, and future trends". In: *Radiographics* 35.4 (2015), pp. 1056–1076. DOI: 10.1148/rg.2015140232.

[94] M. Brown et al. "Method for segmenting chest CT image data using an anatomical model: preliminary results". In: *IEEE Transactions on Medical Imaging* 16.6 (1997), pp. 828–839. DOI: 10.1109/42.650879.

[95] S. Hu, E. Hoffman, and J. Reinhardt. "Automatic lung segmentation for accurate quantitation of volumetric X-ray CT images". In: *IEEE Transactions on Medical Imaging* 20.6 (2001), pp. 490–498. DOI: 10.1109/42.929615.

[96] L.-Y. Tseng and L.-C. Huang. "An adaptive thresholding method for automatic lung segmentation in CT images". In: *AFRICON 2009*. 2009, pp. 1–5. DOI: 10.1109/AFRCON.2009.5308100.

[97] R. Adams and L. Bischof. "Seeded region growing". In: *IEEE Transactions on Pattern Analysis and Machine Intelligence* 16.6 (1994), pp. 641–647. DOI: 10.1109/34.295913.

[98] A. Mangan and R. Whitaker. "Partitioning 3D surface meshes using watershed segmentation". In: *IEEE Transactions on Visualization and Computer Graphics* 5.4 (1999), pp. 308–321. DOI: 10.1109/2945.817348.

[99] Y. Boykov and M.-P. Jolly. "Interactive Organ Segmentation Using Graph Cuts". In: *Medical Image Computing and Computer-Assisted Intervention – MICCAI 2000*. Ed. by S. L. Delp, A. M. DiGoia, and B. Jaramaz. Berlin, Heidelberg: Springer Berlin Heidelberg, 2000, pp. 276–286. ISBN: 978-3-540-40899-4.

[100] T. F. Chan and L. A. Vese. "Active contours without edges". In: *IEEE Transactions on Image Processing* 10.2 (2001), pp. 266–277. DOI: 10.1109/83.902291.

[101] P. A. Yushkevich et al. "User-guided 3D active contour segmentation of anatomical structures: Significantly improved efficiency and reliability". In: *NeuroImage* 31.3 (2006), pp. 1116–1128. DOI: 10.1016/j.neuroimage.2006.01.015.

[102] C. Xu and J. Prince. "Snakes, shapes, and gradient vector flow". In: *IEEE Transactions on Image Processing* 7.3 (1998), pp. 359–369. DOI: 10.1109/83.661186.

[103] L. A. Vese and T. F. Chan. In: *International Journal of Computer Vision* 50.3 (2002), pp. 271–293. DOI: 10.1023/a:1020874308076.

[104] T. W. Way et al. "Computer-aided diagnosis of pulmonary nodules on CT scans: Segmentation and classification using 3D active contours". In: *Medical Physics* 33.7 (2006), pp. 2323–2337. DOI: 10.1118/1.2207129.

[105] J. Song et al. "Lung lesion extraction using a toboggan based growing automatic segmentation approach". In: *IEEE Transactions on Medical Imaging* 35.1 (2016), pp. 337–353. DOI: 10.1109/TMI.2015.2474119.

[106] P. P. Rebouças Filho et al. "Novel and powerful 3D adaptive crisp active contour method applied in the segmentation of CT lung images". In: *Medical Image Analysis* 35 (2017), pp. 503–516. DOI: 10.1016/j.media.2016.09.002.

[107] Y. Guo et al. "Automated iterative neutrosophic lung segmentation for image analysis in thoracic computed tomography". In: *Medical Physics* 40.8 (July 2013), p. 081912. DOI: 10.1118/1.4812679.

[108] A. Mansoor et al. "A Generic Approach to Pathological Lung Segmentation". In: *IEEE Transactions on Medical Imaging* 33.12 (Dec. 2014), pp. 2293–2310. DOI: 10.1109/tmi.2014.2337057.

[109] E. E. Özsavaş et al. "Automatic Segmentation of Anatomical Structures from CT Scans of Thorax for RTP". In: *Computational and Mathematical Methods in Medicine* 2014 (2014), pp. 1–14. DOI: 10.1155/2014/472890.

[110] P. Korfiatis et al. "Optimizing lung volume segmentation by texture classification". In: *Proceedings of the 10th IEEE International Conference on Information Technology and Applications in Biomedicine*. 2010, pp. 1–4. DOI: 10.1109/ITAB.2010.5687763.

[111] P. Korfiatis et al. "Texture classification-based segmentation of lung affected by interstitial pneumonia in high-resolution CT". In: *Medical Physics* 35.12 (Nov. 2008), pp. 5290–5302. DOI: 10.1118/1.3003066.

[112] Y. Tao et al. "Multi-level Ground Glass Nodule Detection and Segmentation in CT Lung Images". In: *Medical Image Computing and Computer-Assisted Intervention – MICCAI 2009*. Springer Berlin Heidelberg, 2009, pp. 715–723. DOI: 10.1007/978-3-642-04271-3_87.

[113] A. Mansoor et al. "A Generic Approach to Pathological Lung Segmentation". In: *IEEE Transactions on Medical Imaging* 33.12 (Dec. 2014), pp. 2293–2310. DOI: 10.1109/tmi.2014.2337057.

[114] I. Sluimer, M. Prokop, and B. van Ginneken. "Toward automated segmentation of the pathological lung in CT". In: *IEEE Transactions on Medical Imaging* 24.8 (Aug. 2005), pp. 1025–1038. DOI: 10.1109/tmi.2005.851757.

[115] O. Ronneberger, P.Fischer, and T. Brox. "U-Net: Convolutional Networks for Biomedical Image Segmentation". In: *Medical Image Computing and Computer-Assisted Intervention (MICCAI)*. Vol. 9351. LNCS. (available on arXiv:1505.04597 [cs.CV]). Springer, 2015, pp. 234–241. URL: http://lmb.informatik.uni-freiburg.de/Publications/2015/RFB15a.

[116] Z. Kunpeng and S. Xin. "Automatic lung field segmentation based on the U-net deep neural network". In: *2019 14th IEEE International Conference on Electronic Measurement and Instruments (ICEMI)*. 2019, pp. 1670–1676. DOI: 10.1109/ICEMI46757.2019.9101832.

[117] Y. Said et al. "Medical Images Segmentation for Lung Cancer Diagnosis Based on Deep Learning Architectures". In: *Diagnostics* 13.3 (Feb. 2023), p. 546. DOI: 10.3390/diagnostics13030546.

[118] S. Ghosh et al. "Using Convolutions and Image Processing Techniques to Segment Lungs from CT Data". In: *Emerging Technology in Modelling and Graphics*. Ed. by J. K. Mandal and D. Bhattacharya. Singapore: Springer Singapore, 2020, pp. 129–136. ISBN: 978-981-13-7403-6.

[119] D. Müller, I. Soto-Rey, and F. Kramer. "Robust chest CT image segmentation of COVID-19 lung infection based on limited data". In: *Informatics in Medicine Unlocked* 25 (2021), p. 100681. DOI: 10.1016/j.imu.2021.100681.

[120] H. Shaziya and K. Shyamala. "Pulmonary CT Images Segmentation using CNN and UNet Models of Deep Learning". In: *2020 IEEE Pune Section International Conference (PuneCon)*. 2020, pp. 195–201. DOI: 10.1109/PuneCon50868.2020.9362463.

[121] S. A. Agnes, J. Anitha, and J. D. Peter. "Automatic lung segmentation in low-dose chest CT scans using convolutional deep and wide network (CDWN)". In: *Neural Computing and Applications* 32.20 (Nov. 2018), pp. 15845–15855. DOI: 10.1007/s00521-018-3877-3.

[122] A.-A.-Z. Imran et al. "Automatic Segmentation of Pulmonary Lobes Using a Progressive Dense V-Network". In: *Deep Learning in Medical Image Analysis and Multimodal Learning for Clinical Decision Support*. Cham: Springer International Publishing, 2018, pp. 282–290. ISBN: 978-3-030-00889-5.

[123] F. T. Ferreira et al. "End-to-End Supervised Lung Lobe Segmentation". In: *2018 International Joint Conference on Neural Networks (IJCNN)*. 2018, pp. 1–8. DOI: 10.1109/IJCNN.2018.8489677.

[124] M. Negahdar, D. Beymer, and T. Syeda-Mahmood. "Automated volumetric lung segmentation of thoracic CT images using fully convolutional neural network". In: Feb. 2018, p. 54. DOI: 10.1117/12.2293723.

[125] X. Feng et al. "Deep convolutional neural network for segmentation of thoracic organs-at-risk using cropped 3D images". In: *Medical Physics* 46.5 (Mar. 2019), pp. 2169–2180. DOI: 10.1002/mp.13466.

[126] R. Nakano et al. "Automated segmentation framework of lung gross tumor volumes on 3D planning CT images using dense V-Net deep learning". In: *International Forum on Medical Imaging in Asia 2019*. Ed. by H. Fujita, F. Lin, and J. H. Kim. SPIE, Mar. 2019. DOI: 10.1117/12.2521509.

[127] C. Liu and M. Pang. "Extracting Lungs from CT Images via Deep Convolutional Neural Network Based Segmentation and Two-Pass Contour Refinement". In: *Journal of Digital Imaging* 33.6 (Oct. 2020), pp. 1465–1478. DOI: 10.1007/s10278-020-00388-0.

[128] M. A. Cifci. "SegChaNet: A Novel Model for Lung Cancer Segmentation in CT Scans". In: *Applied Bionics and Biomechanics* 2022 (May 2022). Ed. by Y. Gu, pp. 1–16. DOI: 10.1155/2022/1139587.

[129] Ü. Budak et al. "Efficient COVID-19 Segmentation from CT Slices Exploiting Semantic Segmentation with Integrated Attention Mechanism". In: *Journal of Digital Imaging* 34.2 (Mar. 2021), pp. 263–272. DOI: 10.1007/s10278-021-00434-5.

[130] Z. Zhang et al. "DENSE-INception U-net for medical image segmentation". In: *Computer Methods and Programs in Biomedicine* 192 (Aug. 2020), p. 105395. DOI: 10.1016/j.cmpb.2020.105395.

[131] R. K. Gupta et al. "COVID-19 Lesion Segmentation and Classification of Lung CTs Using GMM-Based Hidden Markov Random Field and ResNet 18". In: *International Journal of Fuzzy System Applications* 11.2 (May 2022), pp. 1–21. DOI: 10.4018/ijfsa.296587.

[132] L. Geng et al. "Lung segmentation method with dilated convolution based on VGG-16 network". In: *Computer Assisted Surgery* 24 (Aug. 2019), pp. 27–33. DOI: 10.1080/24699322.2019.1649071.

[133] R. Ali, R. C. Hardie, and H. K. Ragb. "Ensemble Lung Segmentation System Using Deep Neural Networks". In: *2020 IEEE Applied Imagery Pattern Recognition Workshop (AIPR)*. 2020, pp. 1–5. DOI: 10.1109/AIPR50011.2020.9425311.

[134] F. Isensee et al. "nnU-Net: a self-configuring method for deep learning-based biomedical image segmentation". In: *Nature Methods* 18.2 (Dec. 2020), pp. 203–211. DOI: 10.1038/s41592-020-01008-z.

[135] J. Hofmanninger et al. "Automatic lung segmentation in routine imaging is primarily a data diversity problem, not a methodology problem". In: *European Radiology Experimental* 4.1 (Aug. 2020). DOI: 10.1186/s41747-020-00173-2.

[136] A. Dosovitskiy et al. *An Image is Worth 16x16 Words: Transformers for Image Recognition at Scale*. 2021. arXiv: 2010.11929. URL: https://arxiv.org/abs/2010.11929.

[137] J. C. Hogg. "Pathophysiology of airflow limitation in chronic obstructive pulmonary disease". In: *The Lancet* 364.9435 (2004), pp. 709–721. ISSN: 0140-6736. DOI: 10.1016/S0140-6736(04)16900-6.

[138] D. E. Niewoehner, J. Kleinerman, and D. B. Rice. "Pathologic changes in the peripheral airways of young cigarette smokers". In: *New England Journal of Medicine* 291.15 (1974), pp. 755–758.

[139] M. Cosio et al. "The relations between structural changes in small airways and pulmonary-function tests". In: *New England Journal of Medicine* 298.23 (1978), pp. 1277–1281.

[140] N. Berend et al. "Small airways disease: reproducibility of measurements and correlation with lung function". In: *Chest* 79.3 (1981), pp. 263–268.

[141] N. Berend, C. Skoog, and W. M. Thurlbeck. "Single-breath nitrogen test in excised human lungs". In: *Journal of Applied Physiology* 51.6 (1981), pp. 1568–1573.

[142] J. L. Wright et al. "Morphology of peripheral airways in current smokers and ex-smokers". In: *American Review of Respiratory Disease* 127.4 (1983), pp. 474–477.

[143] K. A. Hale et al. "Lung disease in long-term cigarette smokers with and without chronic air-flow obstruction". In: *American Review of Respiratory Disease* 130.5 (1984), pp. 716–721.

[144] M. G. Cosio et al. "Morphologic and morphometric effects of prolonged cigarette smoking on the small airways". In: *American Review of Respiratory Disease* 122.2 (1980), pp. 265–271.

[145] J. Leopold and J. Gough. "The centrilobular form of hypertrophic emphysema and its relation to chronic bronchitis". In: *Thorax* 12.3 (1957), p. 219.

[146] A. Anderson and A. G. Foraker. "Centrilobular emphysema and panlobular emphysema: two different diseases". In: *Thorax* 28.5 (1973), pp. 547–550.

[147] M. G. Cosio et al. "Morphologic and morphometric effects of prolonged cigarette smoking on the small airways". In: *American Review of Respiratory Disease* 122.2 (1980), pp. 265–271.

[148] Y. Sato et al. "Three-dimensional multi-scale line filter for segmentation and visualization of curvilinear structures in medical images". In: *Medical Image Analysis* 2.2 (1998), pp. 143–168. ISSN: 1361-8415. DOI: https://doi.org/10.1016/S1361-8415(98)80009-1.

[149] A. F. Frangi et al. "Multiscale vessel enhancement filtering". In: *Medical Image Computing and Computer-Assisted Intervention — MICCAI'98*. Ed. by W. M. Wells, A. Colchester, and S. Delp. Berlin, Heidelberg: Springer Berlin Heidelberg, 1998, pp. 130–137. ISBN: 978-3-540-49563-5.

[150] E. Meijering et al. "Neurite tracing in fluorescence microscopy images using ridge filtering and graph searching: principles and validation". In: *2004 2nd IEEE International Symposium on Biomedical Imaging: Nano to Macro (IEEE Cat No. 04EX821)*. 2004, 1219–1222 Vol. 2. DOI: 10.1109/ISBI.2004.1398764.

[151] T. Jerman et al. "Enhancement of Vascular Structures in 3D and 2D Angiographic Images". In: *IEEE Transactions on Medical Imaging* 35.9 (Sept. 2016), pp. 2107–2118. ISSN: 1558-254X. DOI: 10.1109/tmi.2016.2550102.

[152] R. Zhang et al. "An Improved Fuzzy Connectedness Method for Automatic Three-Dimensional Liver Vessel Segmentation in CT Images". In: *Journal of Healthcare Engineering* 2018 (Oct. 2018), pp. 1–18. ISSN: 2040-2309. DOI: 10.1155/2018/2376317.

[153] R. A. Ochs et al. "Automated classification of lung bronchovascular anatomy in CT using AdaBoost". In: *Medical Image Analysis* 11.3 (2007), pp. 315–324. DOI: 10.1016/j.media.2007.03.004.

[154] M. W. K. Law and A. C. S. Chung. "Three Dimensional Curvilinear Structure Detection Using Optimally Oriented Flux". In: *Computer Vision – ECCV 2008*. Ed. by D. Forsyth, P. Torr, and A. Zisserman. Berlin, Heidelberg: Springer Berlin Heidelberg, 2008, pp. 368–382. ISBN: 978-3-540-88693-8.

[155] O. Merveille et al. "Curvilinear Structure Analysis by Ranking the Orientation Responses of Path Operators". In: *IEEE Transactions on Pattern Analysis and Machine Intelligence* 40.2 (2018), pp. 304–317. DOI: 10.1109/TPAMI.2017.2672972.

[156] A. P. Kiraly et al. "Three-Dimensional Human Airway Segmentation Methods for Clinical Virtual Bronchoscopy". In: *Academic Radiology* 9.10 (2002), pp. 1153–1168. ISSN: 1076-6332. DOI: https://doi.org/10.1016/S1076-6332(03)80517-2.

[157] T. Kitasaka et al. "A Method for Segmenting Bronchial Trees from 3D Chest X-ray CT Images". In: *Medical Image Computing and Computer-Assisted Intervention - MICCAI 2003*. Ed. by R. E. Ellis and T. M. Peters. Berlin, Heidelberg: Springer Berlin Heidelberg, 2003, pp. 603–610. ISBN: 978-3-540-39903-2.

[158] W. Park, E. Hoffman, and M. Sonka. "Segmentation of intrathoracic airway trees: a fuzzy logic approach". In: *IEEE Transactions on Medical Imaging* 17.4 (1998), pp. 489–497. ISSN: 0278-0062. DOI: 10.1109/42.730394.

[159] D. Bartz et al. "Hybrid segmentation and exploration of the human lungs". In: *IEEE Visualization, 2003. VIS 2003.* 2003, pp. 177–184. DOI: 10.1109/VISUAL.2003.1250370.

[160] P. Lo et al. "Vessel-guided airway tree segmentation: A voxel classification approach". In: *Medical Image Analysis* 14.4 (2010), pp. 527–538. DOI: 10.1016/j.media.2010.03.004.

[161] L. M. Lorigo et al. "Codimension-two geodesic active contours for the segmentation of tubular structures". In: *Proceedings of the IEEE Computer Society Conference on Computer Vision and Pattern Recognition* 1 (2000), pp. 444–451. DOI: 10.1109/CVPR.2000.855853.

[162] T. Schlathölter et al. "Simultaneous segmentation and tree reconstruction of the airways for virtual bronchoscopy". In: *Proceedings of SPIE - The International Society for Optical Engineering* 4684 I (2002), pp. 103–113. DOI: 10.1117/12.467061.

[163] T. Deschamps and L. D. Cohen. "Fast extraction of minimal paths in 3D images and applications to virtual endoscopy". In: *Medical Image Analysis* 5.4 (Dec. 2001), pp. 281–299. ISSN: 1361-8415. DOI: 10.1016/s1361-8415(01)00046-9.

[164] S. Aylward and E. Bullitt. "Initialization, noise, singularities, and scale in height ridge traversal for tubular object centerline extraction". In: *IEEE Transactions on Medical Imaging* 21.2 (2002), pp. 61–75. ISSN: 0278-0062. DOI: 10.1109/42.993126.

[165] S. A. Nadeem et al. "A novel iterative method for airway tree segmentation from CT imaging using multiscale leakage detection". In: *Lecture Notes in Computer Science (including subseries Lecture Notes in Artificial Intelligence and Lecture Notes in Bioinformatics)* 10118 LNCS (2017), pp. 46–60. DOI: 10.1007/978-3-319-54526-4_4.

[166] R. Rudyanto et al. "Detecting airway remodeling in COPD and emphysema using low-dose CT imaging". In: vol. 8315. 2012. DOI: 10.1117/12.910901.

[167] P. Lo et al. "Extraction of Airways From CT (EXACT'09)". In: *IEEE Transactions on Medical Imaging* 31.11 (2012), pp. 2093–2107. DOI: 10.1109/TMI.2012.2209674.

[168] J.-P. Charbonnier et al. "Improving airway segmentation in computed tomography using leak detection with convolutional networks". In: *Medical Image Analysis* 36 (2017), pp. 52–60. DOI: 10.1016/j.media.2016.11.001.

[169] J. Yun et al. "Improvement of fully automated airway segmentation on volumetric computed tomographic images using a 2.5 dimensional convolutional neural net". In: *Medical Image Analysis* 51 (2019), pp. 13–20. DOI: 10.1016/j.media.2018.10.006.

[170] A. Garcia-Uceda et al. "Automatic airway segmentation from computed tomography using robust and efficient 3-D convolutional neural networks". In: *Scientific Reports* 11.1 (Aug. 2021). ISSN: 2045-2322. DOI: 10.1038/s41598-021-95364-1.

[171] A. G.-U. Juarez, H. Tiddens, and M. de Bruijne. "Automatic airway segmentation in chest CT using convolutional neural networks". In: *Lecture Notes in Computer Science (including subseries Lecture Notes in Artificial Intelligence and Lecture Notes in Bioinformatics)* 11040 LNCS (2018), pp. 238–250. DOI: 10.1007/978-3-030-00946-5_24.

[172] Y. Qin et al. "AirwayNet: A Voxel-Connectivity Aware Approach for Accurate Airway Segmentation Using Convolutional Neural Networks". In: *Lecture Notes in Computer Science (including subseries Lecture Notes in Artificial Intelligence*

and Lecture Notes in Bioinformatics) 11769 LNCS (2019), pp. 212–220. DOI: 10.1007/978-3-030-32226-7_24.

[173] Y. Qin et al. "Learning Tubule-Sensitive CNNs for Pulmonary Airway and Artery-Vein Segmentation in CT". In: *IEEE Transactions on Medical Imaging* 40.6 (2021), pp. 1603–1617. DOI: 10.1109/TMI.2021.3062280.

[174] A. Garcia-Uceda Juarez, H. A. W. M. Tiddens, and M. de Bruijne. "Automatic Airway Segmentation in Chest CT Using Convolutional Neural Networks". In: *Image Analysis for Moving Organ, Breast, and Thoracic Images*. Ed. by D. Stoyanov et al. Cham: Springer International Publishing, 2018, pp. 238–250. ISBN: 978-3-030-00946-5.

[175] A. Garcia-Uceda Juarez et al. "A Joint 3D UNet-Graph Neural Network-Based Method for Airway Segmentation from Chest CTs". In: *Lecture Notes in Computer Science (including subseries Lecture Notes in Artificial Intelligence and Lecture Notes in Bioinformatics)* 11861 LNCS (2019), pp. 583–591. DOI: 10.1007/978-3-030-32692-0_67.

[176] D. Jin et al. "3D convolutional neural networks with graph refinement for airway segmentation using incomplete data labels". In: *Lecture Notes in Computer Science (including subseries Lecture Notes in Artificial Intelligence and Lecture Notes in Bioinformatics)* 10541 LNCS (2017), pp. 141–149. DOI: 10.1007/978-3-319-67389-9_17.

[177] Q. Meng et al. "Tracking and Segmentation of the Airways in Chest CT Using a Fully Convolutional Network". In: *Medical Image Computing and Computer-Assisted Intervention - MICCAI 2017*. Ed. by M. Descoteaux et al. Cham: Springer International Publishing, 2017, pp. 198–207. ISBN: 978-3-319-66185-8.

[178] Y. Qin et al. "AirwayNet: A Voxel-Connectivity Aware Approach for Accurate Airway Segmentation Using Convolutional Neural Networks". In: *Medical Image Computing and Computer Assisted Intervention – MICCAI 2019*. Ed. by D. Shen et al. Cham: Springer International Publishing, 2019, pp. 212–220. ISBN: 978-3-030-32226-7.

[179] T. Zhao et al. "Bronchus Segmentation and Classification by Neural Networks and Linear Programming". In: *Medical Image Computing and Computer Assisted Intervention – MICCAI 2019*. Ed. by D. Shen et al. Cham: Springer International Publishing, 2019, pp. 230–239. ISBN: 978-3-030-32226-7.

[180] Y. Qin et al. "Learning Bronchiole-Sensitive Airway Segmentation CNNs by Feature Recalibration and Attention Distillation". In: *Medical Image Computing and Computer Assisted Intervention – MICCAI 2020*. Ed. by A. L. Martel et al. Cham: Springer International Publishing, 2020, pp. 221–231. ISBN: 978-3-030-59710-8.

[181] G. Vegas Sánchez-Ferrero et al. "Harmonization of chest CT scans for different doses and reconstruction methods". In: *Medical Physics* 46 (June 2019). DOI: 10.1002/mp.13578.

[182] T. Lindeberg. "Scale-space for N-D discrete signals". In: *Scale-Space Theory in Computer Vision*. Boston, MA: Springer US, 1994, pp. 101–122. ISBN: 978-1-4757-6465-9. DOI: 10.1007/978-1-4757-6465-9_4.

[183] M. Hubert and E. Vandervieren. "An adjusted boxplot for skewed distributions". In: *Computational Statistics and Data Analysis* 52.12 (2008), pp. 5186–5201. ISSN: 0167-9473. DOI: 10.1016/j.csda.2007.11.008.

[184] R. Uppaluri et al. "Quantification of Pulmonary Emphysema from Lung Computed Tomography Images". In: *American Journal of Respiratory and Critical Care Medicine* 156.1 (July 1997), pp. 248–254. DOI: 10.1164/ajrccm.156.1.9606093.

[185] H. O. Coxson et al. "A Quantification of the Lung Surface Area in Emphysema Using Computed Tomography". In: *American Journal of Respiratory and Critical Care Medicine* 159.3 (Mar. 1999), pp. 851–856. ISSN: 1535-4970. DOI: 10.1164/ajrccm.159.3.9805067.

[186] R. UPPALURI et al. "Quantification of Pulmonary Emphysema from Lung Computed Tomography Images". In: *American Journal of Respiratory and Critical Care Medicine* 156.1 (July 1997), pp. 248–254. ISSN: 1535-4970. DOI: 10.1164/ajrccm.156.1.9606093.

[187] R. Uppaluri et al. "Adaptive Multiple Feature Method (AMFM) for the early detection of parenchymal pathology in a smoking population". In: vol. 3337. 1998, pp. 8–13. DOI: 10.1117/12.312563.

[188] G. Vegas-Sánchez-Ferrero and R. San José Estépar. "A CT scan harmonization technique to detect emphysema and small airway diseases". In: *Lecture Notes in Computer Science (including subseries Lecture Notes in Artificial Intelligence*

and Lecture Notes in Bioinformatics) 11040 LNCS (2018), pp. 180–190. DOI: 10.1007/978-3-030-00946-5_19.

[189] Y. Hame et al. "Adaptive quantification and longitudinal analysis of pulmonary emphysema with a hidden markov measure field model". In: *IEEE Transactions on Medical Imaging* 33.7 (2014), pp. 1527–1540. DOI: 10.1109/TMI.2014.2317520.

[190] S. D. Almeida et al. "cOOpD: Reformulating COPD Classification on Chest CT Scans as Anomaly Detection Using Contrastive Representations". In: *Lecture Notes in Computer Science (including subseries Lecture Notes in Artificial Intelligence and Lecture Notes in Bioinformatics)* 14224 LNCS (2023), pp. 33–43. DOI: 10.1007/978-3-031-43904-9_4.

[191] M. T. Cazzolato et al. "dp-BREATH: Heat maps and probabilistic classification assisting the analysis of abnormal lung regions". In: *Computer Methods and Programs in Biomedicine* 173 (2019), pp. 27–34. ISSN: 0169-2607. DOI: 10.1016/j.cmpb.2019.01.014.

[192] L. Chen et al. "A Graph Convolutional Multiple Instance Learning on a Hypersphere Manifold Approach for Diagnosing Chronic Obstructive Pulmonary Disease in CT Images". In: *IEEE Journal of Biomedical and Health Informatics* 26.12 (2022), pp. 6058–6069. DOI: 10.1109/JBHI.2022.3209410.

[193] Z. Li et al. "Early detection of COPD based on graph convolutional network and small and weakly labeled data". In: *Medical and Biological Engineering and Computing* 60.8 (2022), pp. 2321–2333. DOI: 10.1007/s11517-022-02589-x.

[194] Y. Suzuki et al. "Segmentation of Diffuse Lung Abnormality Patterns on Computed Tomography Images using Partially Supervised Learning". In: *Advanced Biomedical Engineering* 11 (2022), pp. 25–36. DOI: 10.14326/abe.11.25.

[195] L. Peng et al. "Semi-supervised learning for semantic segmentation of emphysema with partial annotations". In: *IEEE Journal of Biomedical and Health Informatics* 24.8 (2020), pp. 2327–2336. DOI: 10.1109/JBHI.2019.2963195.

[196] J. C. Ross et al. "A Bayesian Nonparametric Model for Disease Subtyping: Application to Emphysema Phenotypes". In: *IEEE Transactions on Medical Imaging* 36.1 (2017), pp. 343–354. DOI: 10.1109/TMI.2016.2608782.

[197] P. Savadjiev et al. "Improved Detection of Chronic Obstructive Pulmonary Disease at Chest CT Using the Mean Curvature of Isophotes". In: *Radiology: Artificial Intelligence* 4.1 (2022). DOI: 10.1148/ryai.210105.

[198] S. K. H. Bukhari and L. Fahad. "Lung Disease Detection using Deep Learning". In: 2022, pp. 154–159. DOI: 10.1109/ICET56601.2022.10004651.

[199] X. Deng et al. "COPD stage detection: leveraging the auto-metric graph neural network with inspiratory and expiratory chest CT images". In: *Medical and Biological Engineering and Computing* 62.6 (2024), pp. 1733–1749. DOI: 10.1007/s11517-024-03016-z.

[200] F. Binczyk et al. "MiMSeg - an algorithm for automated detection of tumor tissue on NMR apparent diffusion coefficient maps." In: *Information Sciences* 384 (2017), pp. 235–248. ISSN: 0020-0255. DOI: 10.1016/j.ins.2016.07.052.

[201] W. Penny, J. Mattout, and N. Trujillo-Barreto. "CHAPTER 35 - Bayesian model selection and averaging". In: *Statistical Parametric Mapping*. Ed. by K. FRISTON et al. London: Academic Press, 2007, pp. 454–467. ISBN: 978-0-12-372560-8. DOI: 10.1016/B978-012372560-8/50035-8.

[202] J. Cohen. "CHAPTER 3 - The Significance of a Product Moment rs". In: *Statistical Power Analysis for the Behavioral Sciences*. Ed. by J. Cohen. Academic Press, 1977, pp. 75–107. ISBN: 978-0-12-179060-8. DOI: 10.1016/B978-0-12-179060-8.50008-6.

[203] R. UPPALURI et al. "Quantification of Pulmonary Emphysema from Lung Computed Tomography Images". In: *American Journal of Respiratory and Critical Care Medicine* 156.1 (July 1997), pp. 248–254. ISSN: 1535-4970. DOI: 10.1164/ajrccm.156.1.9606093.

[204] L. Sorensen, S. B. Shaker, and M. De Bruijne. "Quantitative analysis of pulmonary emphysema using local binary patterns". In: *IEEE transactions on medical imaging* 29.2 (2010), pp. 559–569.

[205] L. Peng et al. "Joint weber-based rotation invariant uniform local ternary pattern for classification of pulmonary emphysema in CT images". In: *2017 IEEE International Conference on Image Processing (ICIP)*. IEEE. 2017, pp. 2050–2054.

[206] R. Nava et al. "Extended Gabor approach applied to classification of emphysematous patterns in computed tomography". In: *Medical and Biological Engineering and Computing* 52 (2014), pp. 393–403.

[207] T. Azim and M. Niranjan. "Texture classification with Fisher kernel extracted from the continuous models of RBM". In: *2014 International Conference on Computer Vision Theory and Applications (VISAPP)*. Vol. 2. IEEE. 2014, pp. 684–690.

[208] P. Lambin et al. "Radiomics: extracting more information from medical images using advanced feature analysis". In: *European journal of cancer* 48.4 (2012), pp. 441–446.

[209] P. Lambin et al. "Radiomics: the bridge between medical imaging and personalized medicine". In: *Nature reviews Clinical oncology* 14.12 (2017), pp. 749–762.

[210] V. Cheplygina et al. "Transfer learning for multicenter classification of chronic obstructive pulmonary disease". In: *IEEE journal of biomedical and health informatics* 22.5 (2017), pp. 1486–1496.

[211] Z. Li et al. "A novel CT-based radiomics features analysis for identification and severity staging of COPD". In: *Academic Radiology* 29.5 (2022), pp. 663–673.

[212] Y. Yang et al. "Lung radiomics features for characterizing and classifying COPD stage based on feature combination strategy and multi-layer perceptron classifier". In: *Mathematical Biosciences and Engineering* 19.8 (2022), pp. 7826–7855.

[213] Y. Yang et al. "Lung radiomics features selection for COPD stage classification based on auto-metric graph neural network". In: *Diagnostics* 12.10 (2022), p. 2274.

[214] P. R. Amudala Puchakayala et al. "Radiomics for improved detection of chronic obstructive pulmonary disease in low-dose and standard-dose chest CT scans". In: *Radiology* 307.5 (2023), e222998.

[215] G. Gonzalez et al. "Disease staging and prognosis in smokers using deep learning in chest computed tomography". In: *American journal of respiratory and critical care medicine* 197.2 (2018), pp. 193–203.

[216] S. Singla et al. "Improving clinical disease subtyping and future events prediction through a chest CT-based deep learning approach". In: *Medical physics* 48.3 (2021), pp. 1168–1181.

[217] C. Xu et al. "DCT-MIL: Deep CNN transferred multiple instance learning for COPD identification using CT images". In: *Physics in Medicine & Biology* 65.14 (2020), p. 145011.

[218] R. Du et al. "Identification of COPD from multi-view snapshots of 3D lung airway tree via deep CNN". In: *IEEE Access* 8 (2020), pp. 38907–38919.

[219] L. Y. Tang et al. "Towards large-scale case-finding: training and validation of residual networks for detection of chronic obstructive pulmonary disease using low-dose CT". In: *The Lancet Digital Health* 2.5 (2020), e259–e267.

[220] T. T. Ho et al. "A 3D-CNN model with CT-based parametric response mapping for classifying COPD subjects". In: *Scientific Reports* 11.1 (2021), p. 34.

[221] L. Chen et al. "A graph convolutional multiple instance learning on a hypersphere manifold approach for diagnosing chronic obstructive pulmonary disease in CT images". In: *IEEE Journal of Biomedical and Health Informatics* 26.12 (2022), pp. 6058–6069.

[222] L. Zhang et al. "COPD identification and grading based on deep learning of lung parenchyma and bronchial wall in chest CT images". In: *The British Journal of Radiology* 95.1133 (2022), p. 20210637.

[223] Y. Wu et al. "Deep CNN for COPD identification by Multi-View snapshot integration of 3D airway tree and lung field". In: *Biomedical Signal Processing and Control* 79 (2023), p. 104162.

[224] J. Sun et al. "Detection and staging of chronic obstructive pulmonary disease using a computed tomography–based weakly supervised deep learning approach". In: *European radiology* 32.8 (2022), pp. 5319–5329.

[225] Z. Li et al. "Early detection of COPD based on graph convolutional network and small and weakly labeled data". In: *Medical and Biological Engineering and Computing* 60.8 (2022), pp. 2321–2333.

[226] M. Xue et al. "CT-based COPD identification using multiple instance learning with two-stage attention". In: *Computer Methods and Programs in Biomedicine* 230 (2023), p. 107356.

[227] K. Yu et al. "DrasCLR: A self-supervised framework of learning disease-related and anatomy-specific representation for 3D lung CT images". In: *Medical Image Analysis* 92 (2024), p. 103062. ISSN: 1361-8415. DOI: 10.1016/j.media.2023.103062.

[228] J. Vestbo et al. "Evaluation of COPD longitudinally to identify predictive surrogate end-points (ECLIPSE)". In: *European Respiratory Journal* 31.4 (2008), pp. 869–873.

[229] M. DeCamp and J. C. Tilburt. "Why we cannot trust artificial intelligence in medicine". In: *The Lancet Digital Health* 1.8 (Dec. 2019), e390. ISSN: 2589-7500. DOI: 10.1016/S2589-7500(19)30197-9.

[230] J. J. Hatherley. "Limits of trust in medical AI". In: *Journal of Medical Ethics* 46.7 (2020), pp. 478–481. ISSN: 0306-6800. DOI: 10.1136/medethics-2019-105935.

[231] L. McInnes et al. "UMAP: Uniform Manifold Approximation and Projection". In: *Journal of Open Source Software* 3.29 (2018), p. 861. DOI: 10.21105/joss.00861.

[232] B. Luo, R. C. Wilson, and E. R. Hancock. "Spectral embedding of graphs". In: *Pattern Recognition* 36.10 (2003), pp. 2213–2230. ISSN: 0031-3203. DOI: 10.1016/S0031-3203(03)00084-0.

[233] D.-A. Clevert, T. Unterthiner, and S. Hochreiter. *Fast and Accurate Deep Network Learning by Exponential Linear Units (ELUs)*. 2016. arXiv: 1511.07289 [cs.LG].